Synthesis, characterisation and engineering of thin films of ZSM-5 on alumina, quartz and sand supports

By

Velaphi Zakhele Msimang

B.Tech (Chem. Eng.) - Peninsula Technikon

M.E. (Civil/Env. Eng.) - Texas A&M University

Submitted to the University of Cape Town
in fulfillment of the requirements
for the degree of
Doctor of Philosophy

Department of Chemical Engineering
University of Cape Town
Rondebosch
Cape Town, June 5, 2005

Acknowledgements

The many people to whom I owe a word of thanks include the following (in no order of importance), and to all of them and those inadvertently omitted, I say may the pool from which you draw your strength grow ever so deeper.

- Swedish colleagues who made my stay in Luleå pleasant: Dr Jonas Hedlund and his family, Dr Fredrik Jareman, Dr Olov Öhrman and his family, Jonas Lindmark, Dr. Valeri Naydenov;
- Dr Klaus Möller, without whose profound engineering wisdom and guidance I would have fallen flat on my face. Thanks to you Klaus, the hikes up Table Mountain were some of the high points of my stay in Cape Town. Many more thanks to Sharon as well. Oh and the cat!;
- the faceless members of the LaTeX cyberfamily who took time out to answer my newbie questions;
- members of the Catalysis division at UCT, for making it pleasant to be at the office by balancing hard work with humor;

The people around whom my life revolves deserve special mention, because it is from them that I have gotten the strength, the inspiration and the will to keep going. On this side of the line, these include my parents, Matswene no Bab'uMsimang, siblings, uBhuti no Ntsika, and the nephew and niece (Hlomi and Asante) that will carry the torch forward. The 'Sakkies' family is right alongside in this long list. On the other side there are many as well, including u Jojoza, Mteni, Silwane, uMaMboweni, uMaLegoale, Mhlahlela.

The spirit of this family has guided me through many dark patches, and it is to them that this work is devoted.

Synopsis

Zeolite films supported on inert material are a novel type of catalyst that could provide interesting activity and selectivity properties. Such materials will see application in catalytic distillation as reactive packings and in novel low pressure drop catalytic reactors.

This thesis studies the physical and reactive properties of thin ZSM-5 films supported on alumina, quartz and sand packings. The objective of this work is to evaluate the intrinsic catalytic properties of these materials by estimating the reaction-diffusion model parameters from the results of the tri-isopropylbenzene (TIPB) cracking and para-xylene (pX) isomerization probe reactions. These intrinsic model parameters are then correlated with respect to the physical analysis of the zeolite films. It is postulated that the zeolite films on all supports would be smooth and homogeneous, the model parameters would be independent of film thickness while the selectivity and activity would depend strongly on film thickness.

Zeolite films were prepared on 3 supports (3mm quartz and alumina beads, and 0.2mm sand particles) using the seed film method. The samples are characterised using SEM, N_2 adsorption, XPS, EDX, and ICP-AES. SEM analysis indicated that four film thicknesses of 150, 350, 800, 2300 nm are prepared on each support.

Results indicate that only the Quartz supported zeolite films could be characterised as smooth and homogeneous. The sand supported zeolite was subject to agglomeration during preparation. The alumina support contained surface pores and mobile cations which caused non-uniform film growth and deactivated the active sites during catalyst pretreatment, respectively.

The TIPB reaction, which estimated only the external activity[1] of the catalyst, showed that, for smooth inert films (quartz, sand) and within experimental error, the rate constants remained constant with increasing film thickness. In the case of alumina supports, the activity increased with increasing film thickness, conforming to a diffusion driven migration of Na^+ cations which is confirmed by EDX and reaction analysis.

The pX isomerization estimates the overall activity and selectivity. Smooth, homogeneous films with plate like geometry were assumed in all cases in order to develop a simple one-dimensional reaction-diffusion model. The model provided an excellent description of the experimental data.

Analysis shows that for smooth, homogeneous zeolite films (quartz, sand) the activity is independent of film thickness. The pX activity of the alumina film (*i.e.*, the zeolite film supported on alumina beads), increased with increasing film thickness which corresponded to deactivation caused by migration of Na^+ ions. Although, diffusion limitations were present, the observed ortho-xylene selectivity enhancement and activity reduction with increasing film thickness did not conform to that predicted by the reaction-diffusion model. As a result, the diffusivity increased with increasing film thickness i.e. it was not possible to predict the variation of activity and selectivity with film thickness using a single diffusion coefficient. This was attributed to the

[1]Throughout this thesis, 'external activity' implies the activity of the non shape-selective acid sites resident on the outside of the zeolite matrix.

non-homogeneity of the zeolite film possibly as a result of variations in the growth orientation and, in the case of alumina supports, cation migration.

Chemical Vapor deposition (CVD) of tetraethoxysilane (TEOS) onto the external surface of a sand supported zeolite served only to deactivate the catalyst without significant selectivity enhancements. This has been attributed to a bulk blocking effect, in which active sites (pore volume) are rendered inacessible by CVD.

It is concluded that zeolite supported films approximated as smooth, homogeneous supports by physical characterization may not necessarily be homogeneous for catalytic applications even when care is taken to ensure that the support is smooth and inert. Furthermore, the selectivity and activity variation with film thickness are considerably smaller than expected.

Contents

List of Figures

List of Tables

Nomenclature

A	chromatogram peak area	[-]
A_z	theoretical external surface area of zeolite sample	$[L^2]$
c_i	molar concentration of species i	$[\frac{mol}{L^3}]$
$c_{i,b}$	bulk concentration of species i	$[\frac{mol}{L^3}]$
$c_{i,s}$	surface concentration of species i	$[\frac{mol}{L^3}]$
D	gas phase diffusivity	$[\frac{L^2}{T}]$
d	diameter	$[L]$
D_i	effective diffusivity of species i	$[\frac{L^2}{T}]$
d_p	particle diameter	$[L]$
D_{AB}	diffusivity of species A in fluid B	$[\frac{L^2}{T}]$
D_{eff}	effective diffusivity	$[\frac{L^2}{T}]$
F_i	molar flow rate of species i	$[\frac{mol}{T}]$
$[i]$	concentration of species i	$\frac{mol}{L^3}$
J	molar flux	$[\frac{mol}{L^2T}]$
k_i	reaction rate constant of species i	$[T^{-1}]$
L	bed length	$[L]$
M_i	molecular mass of species i	$[\frac{M}{mol}]$
n	number of entities	[-]
n	reaction order	[-]
$n_{i,fed}$	moles of species i fed to reactor	[mol]
$\dot{n}$	molar flowrate	$[\frac{mol}{T}]$
P	pressure	$[\frac{M}{T^2L^2}]$

P^o	standard pressure	$[\frac{M}{T^2L^2}]$
P_{vap}	vapor pressure	$[\frac{L^3}{T}]$
Pe_p	particle Peclet number	[-]
R	radius of catalyst particle	$[L]$
R	universal gas constant	$\frac{J}{molK}$
$r_{i,max}$	maximum reaction rate of species i	$[\frac{mol}{L^3T}]$
r_i	reaction rate of species i	$[\frac{mol}{L^3T}]$
$\mathrm{r_{crystal}}$	crystal size	$[L]$
Re	reynolds number	[-]
Re_p	particle Reynolds number	[-]
Sc	Schmidt number	[-]
Sh	Sherwood number	[-]
STP	standard temperature and pressure	
T	temperature	$[^oC$ or $K]$
T^o	standard temperature	$[^oC$ or $K]$
T_f	film thickness	$[L]$
T_R	reaction temperature	$[^oC$ or $K]$
u	linear velocity	$\frac{L}{T}$
$V_{z(eolite)}$	volume of zeolite sample	$[L^3]$
$\dot{v}_{cg}$	carrier gas volumetric flowrate	$[\frac{L^3}{T}]$
$\sum_v$	Fuller et al. [1966] volume parameter	[-]
W_i	molar flux of species i	$[\frac{moles}{L^3 \cdot T}]$
X_i	conversion of species i	[[-] or %]
$X_{i,int}$	integral conversion of species i	[[-] or %]
x	conversion	[[-] or %]
$x_{i,max}$	maximum conversion of species i	[[-] or %]
z	position in the plug flow reactor of length L	[–]

Greek letters

α	fraction of accessible external acid sites to the total amount of acid sites on the unmodified external zeolite surface	[-]
η_i	effectiveness factor of species i	[-]
μ	viscosity	$[\frac{M}{LT}]$
ϕ_i	Thiele modulus	[-]
ρ	density	$[\frac{M}{L^3}]$
τ	residence time	$[T]$
τ_m	modified residence time	$[\frac{L}{T}]$
ζ_i	dimensionless position of species i	[-]

Chapter 1

Introduction

When a chemical reaction takes place in the pores of a zeolite, the observed results are the culmination of a series of processes, the slowest of which masks the role of the others. The researcher investigating the intrinsic properties of the catalyst therefore needs to be able to deconvolute the contributions of each of these phenomena to the observed results. This chapter provides a glimpse into these processes, the techniques to study them, and the related physical properties of zeolite films. Because the ultimate objective is to provide a better understanding of the catalytic properties of these films, the focus is accordingly limited.

1.1 Background

A catalyst is a substance that changes the rate of a reaction without itself being consumed. It does this by reducing the amount of activation energy that has to be put into enabling a chemical reaction (see figure 1.1), thus making production processes economical. Most chemical reactions in industry are catalytic, and a majority of these use a solid catalyst [Gates, 1992; Rabo and Schoonover, 2001; Bozell, 2002].

If the catalyst and reactants are in the same phase, the catalytic reaction is classified as *homogeneous*. Otherwise, it is *heterogeneous*. In line with the focus of this work, the discussion will henceforth be limited to heterogeneous catalysis, with the catalyst being in the solid phase.

Locations (called *active* or *acid sites*) where the actual chemical reactions occur are distributed throughout the catalyst surface area, and it is desired to limit the reaction to formation of the valuable product.

In microporous catalysts, the active/metal sites sitting in the spatially restrictive micro pores go further than cutting energy costs. They enhance selectivity by denying access to molecules with much larger kinetic diameters than the size of the pore entrances (*reactant shape selectivity*). When a reaction can follow different routes, the internal pores suppress the mechanism that

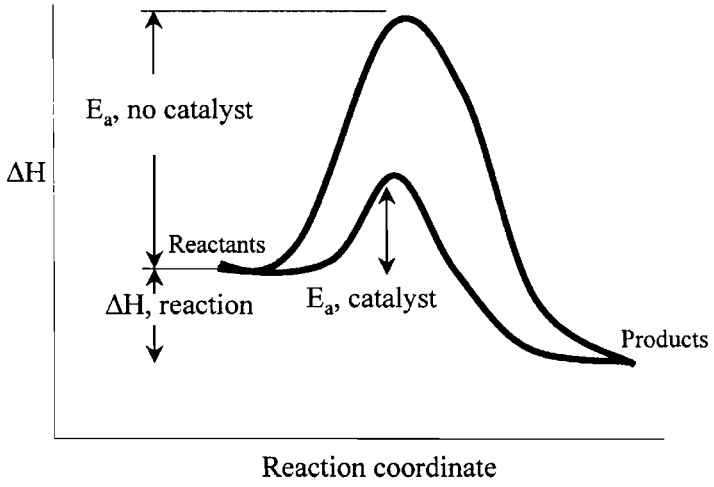

Figure 1.1: A catalyst lowers the activation barrier (E_a) that impedes a chemical reaction.

involves large intermediates (*transition state selectivity*). After a reaction has occurred in the pore, only the products with optimal configurations will leave the pore system (*product shape selectivity*), or the rate of diffusion of the bulkier ones will be retarded (*diffusion-controlled shape selectivity*). Over and above the fact that the catalyst itself is environmentally friendly compared to liquid acids or metal catalysts, its shape selective properties help reduce the amount of waste generated, thereby minimizing the environmental impact of chemical processes. The production of valuable product is also increased [Derouane, 1998; Tsai et al., 1999; Anastas et al., 2000; Ziolek, 2004].

1.2 The catalytic cycle

Figure 1.2 is a schematic representation of the processes that take place during heterogeneous catalysis using porous catalysts.

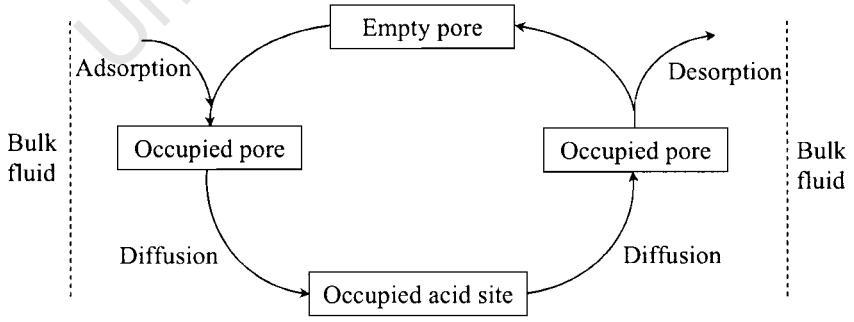

Figure 1.2: The cycle of some of the processes occurring inside porous catalysts. After Schuring [2002].

Reactants migrate from the bulk fluid phase to the stationary layer marking the solid-fluid interface of the system. Across this layer they diffuse and are adsorbed on the solid phase. From here they diffuse through the pore/channel until they reach the active site, where a reaction takes place and products form. This sequence is then reversed until the products end up in the bulk fluid, where the experimentalist collects the data. Since the slowest phenomenon (also referred

to as the *rate-controlling step*) determines the observed results - in cases where the chemical reaction is not the rate-controlling step - it camouflages the intrinsic properties of the catalyst [Hougen and Watson, 1943; Weisz and Swegler, 1955; Satterfield, 1969; Weisz and Prater, 1954; Weisz, 1973; Wei, 1982; Bauer et al., 1991; Post, 1991; Li et al., 1992]. The role of adsorption in the cycle is relatively well-known [Palekar and Rajadhyaksha, 1986; Kärger and Ruthven, 1992].

As this work will demonstrate, the diffusion process can be key to an accurate evaluation of the catalyst properties.

Put simplistically, when the size of guest molecules is close to that of the intracrystalline pore space - as is the case with many heterogeneous reactions in microporous (*i.e.*, $d < 2nm$) environments - the reactant and/or product molecule will either creep or bounce off the walls of the channels until it reaches the active site and/or bulk phase, respectively. Time scales of these modes of migration differ by many orders of magnitude. Thus the importance of an intimate understanding of the behavior of molecules in microporous media.

The work of Thiele [1939] was seminal to an understanding of the relationship between intraparticle diffusion and heterogeneous catalysis. A brief history of the subject is laid out by Wheeler [1951]. Especially because of its impact on the goals of this work, it is explored in further detail in §1.3 and §1.10.1.

1.3 Diffusion

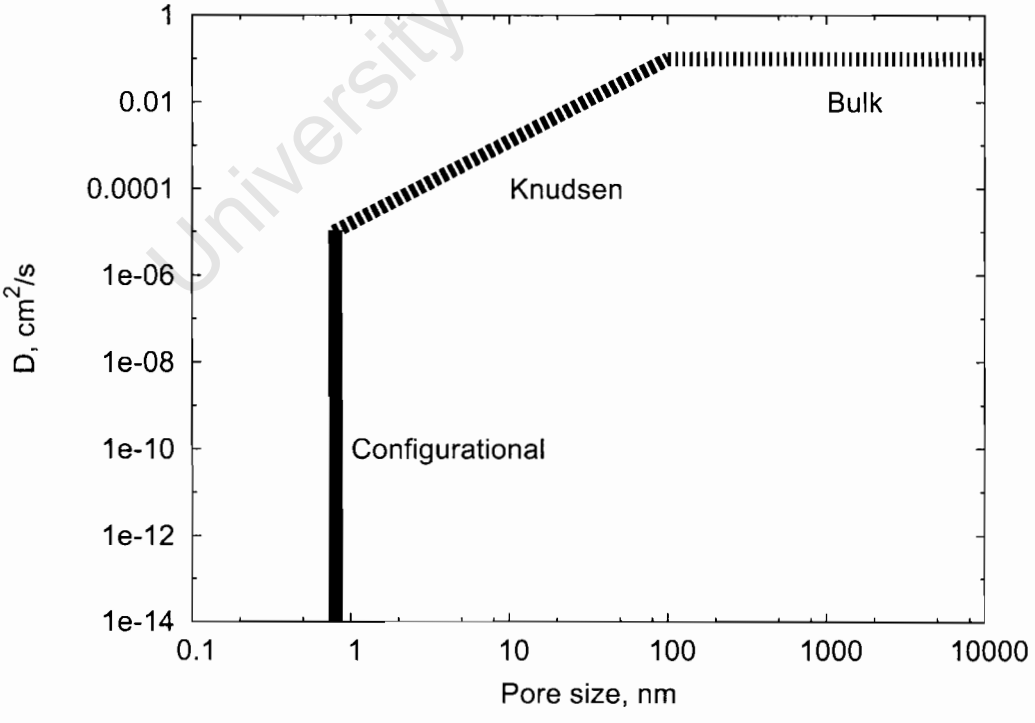

Figure 1.3: Effect of pore size on the diffusion regime.

Figure 1.3 is a schematic showing the possible diffusion regimes in pores of varying sizes.

Porous materials may have a bi- or multimodal pore size distribution (see figure 1.4) as a result of the micropores within a particle (*intraparticle*) and macropores between neighboring particles (*interparticle*).

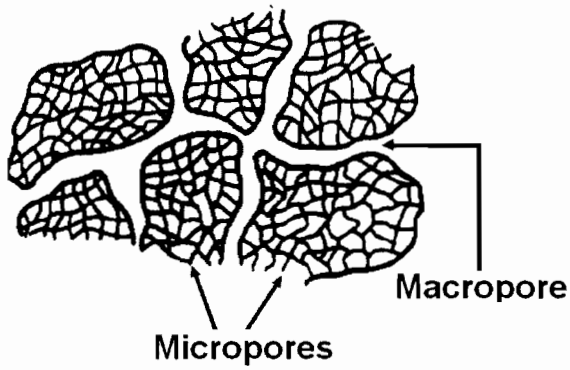

Figure 1.4: Schematic representation of bidisperse pore structure. After Petropoulos et al. [1991].

As can be inferred from figures 1.3 and 1.4, the nature of the pore size distribution has implications on the relative rates of diffusion in the macro- or microporous regions [Heering et al., 1982; Li et al., 1992; Palekar and Rajadhyaksha, 1986; Doelle et al., 1981]. The diffusion resistance in these regions is also impacted by the ratio of the sizes of the microparticles to those of the agglomerates. Models for the study of materials with such *bidisperse* pore size distributions have been developed [Doğu, 1998].

Basically, when there is a concentration gradient (∇c) in an environment where the probability of collisions between molecules and walls is very low, the thermally-driven random motion and subsequent collisions of these molecules drive them to the region of low concentration. Their flux ($\mathbf{J}$) to this region can be approximated using Fick's first law of diffusion (equation 1.1):

$$\mathbf{J} = -\mathbf{D} \cdot \nabla \mathbf{c} \tag{1.1}$$

where D is the diffusion coefficient. When molecules collide with pore walls more often than they do with one another, their flux depends on temperature and the dimensions of the pores. This is the *Knudsen* regime of diffusion.

Weisz [1980] showed that in such microporous environments as those that obtain in zeolites, diffusivities can be many orders of magnitude lower than in the Knudsen region. He labeled this diffusion *configurational*, and in this mode the interaction of the diffusing molecules among themselves and with the walls of microporous host are the factors that affect their transport.

Efforts to develop the pool of knowledge on these phenomena continue on two main fronts, with molecular dynamic simulation being one and the development of experimental techniques to measure diffusivities the other [Kärger and Ruthven, 1992; Keil, 1996; Nijhuis et al., 1999a,b; Paschek and Krishna, 2001]. However, these studies are often done using single components diffusing at

low temperatures. Under these conditions, the measured diffusivities may be much higher than in a multicomponent environment, where slower diffusing species may retard diffusion of the fast ones [Klemm and Emig, 1997; Masuda et al., 2000]. The challenge remains, therefore, to gather data under catalytic reaction conditions, where multicomponent diffusion at high temperature is involved [Haag et al., 1982; Baiker et al., 1982; Post, 1991; Haag, 1994; Keipert and Baerns, 1998; Koriabkina et al., 2002; Čejka and Wichterlová, 2002; Schwan and Möller, 2003].

Interest in zeolite ZSM-5 is because - over and above its zeolitic properties - its dimensions are similar to those of many industrially important organic molecules. Under reaction conditions, this proximity in dimensions between the ZSM-5 channels and the guest species imply a keen interaction between the two and among the guest species molecules themselves. Transport of these molecules is therefore retarded considerably more than it would be outside the pores of this zeolite. Typical diffusivities of paraxylene in silicalite and ZSM-5 are shown in table 1.1. Under catalytic conditions (high temperature), they may differ by orders of magnitude[1] from the values obtained at low temperature in single component systems[Garcia and Weisz, 1993].

1.4 Zeolites

Belonging in microporous materials used in industry [Budd et al., 2004], zeolites are regular three-dimensional networks of silicon and oxygen in which a certain proportion of the silicon is replaced by aluminum. Many occur naturally, but some are synthesized in the laboratory. With each silicon atom sitting at the center, the zeolite network is a continuous matrix of SiO_4 and AlO_4^- tetrahedra (otherwise referred to as *primary building units*), with the oxygen atoms linking the neighboring units. Together with the number of tetrahedra, the pore openings of the cage-like structures resulting from these links determine the dimensions by which the structure is defined (see figure 1.5 for illustration).

The negative charge induced by the AlO_4^- group can be neutralized either by protons, NH_4^+ or metal cations.

The poisoning effect of alkali cations on zeolites has been observed, with Baba et al. [1996] finding that in acid-catalyzed hexane cracking and cyclopropane isomerization, the catalytic activity of H-ZSM-5 is degraded severely by the presence of small proportions of sodium and potassium ions (figure 1.6).

When protons are the counterions, the resultant hydroxyl groups act as Brønsted acid sites (figure 1.7). The less well characterized Lewis acid sites result from the counterbalancing of the negative charge of the framework by extra-framework cations [Sokol et al., 2000; Catana et al., 2001]. The general topic of the nature of acidity in zeolites and other solid catalysts is reviewed by Benesi and Winquist [1978]. Generally, a zeolite can be represented by the formula: $M_{x/v}[(AlO_2)_x(SiO_2)_z]nH_2O$, where M is a counterion of valence v, n is the number of water

[1] Other factors, including the Si/Al ratio and film morphology, could account for the differences in the estimated diffusivities [Kärger and Ruthven, 1992].

Table 1.1: pX diffusivities in Silicalite/ZSM-5. Adapted from Kärger and Ruthven [1992].

Sorbate	Sorbent	$r_{crystal}$ μm	D(at 298K) m^2/s	E_a kJ/mol
pX	H-ZSM-5	1.8	6×10^{-15}	
	H-ZSM-5	0.3	3×10^{-15}	-
	H-ZSM-5	0.5	$\approx 10^{-20}$	66.5
	H-ZSM-5 [a]	0.8	$\approx 10^{-15}$	55
	H-ZSM-5 [b]	-	$\approx 10^{-11}$	-
	H-ZSM-5 [c]	0.5	6×10^{-16}	-
	H-ZSM-5 [d]	0.4	$\approx 1 \times 10^{-14}$	-
	Silicalite	1	$\approx 10^{-15}$	15
	Silicalite	27.5	4×10^{-14}	30
mX	H-ZSM-5	14	2×10^{-14}	-
	Silicalite	1	4×10^{-16}	-
	H-ZSM-5 [e]	0.5	7×10^{-19}	29
	H-ZSM-5 [f]	0.15	9.6×10^{-20}	-
oX	H-ZSM-5	1.5	$\approx 10^{-19}$	-
	H-ZSM-5	0.5	$\approx 10^{-16}$	-
	H-ZSM-5 [g]	-	$\approx 10^{-14}$	-
	H-ZSM-5 [h]	0.025	5×10^{-19}	37
	H-ZSM-5 [i]	0.35	1.8×10^{-18}	37
	H-ZSM-5 [j]	0.5	6.5×10^{-18} m^2/s	30
	H-ZSM-5 [k]	0.15	2.2×10^{-18}	-
	Silicalite	1	2×10^{-16}	-
	Silicalite	27.5	2×10^{-15}	34
	H-ZSM-5 [l]	13.5	$5 \pm 3 \times 10^{-17}$	-

[a] Data from Masuda et al. [1998] measured at 498K.
[b] Data from Olson et al. [1981] measured at 588K.
[c] Data from Mirth et al. [1993] measured at 373K.
[d] Data from Chon et al. [1991] measured at 373K.
[e] Data from Mirth et al. [1993] measured at 373K. At 473K, D = 5×10^{-18} m^2/s.
[f] Data from Chon et al. [1991] measured at 373K.
[g] Data from Olson et al. [1981] measured at 588K.
[h] Data from Olson and Haag [1984] measured at 393K.
[i] Data from Olson and Haag [1984] measured at 393K.
[j] Data from Mirth et al. [1993] measured at 373K. At 473K, D = 5×10^{-17} m^2/s.
[k] Data from Chon et al. [1991] measured at 373K.
[l] Data from Klemm and Emig [1997] measured at 483K in a single-component system. $D = 3.5 \pm 1.5 \times 10^{-16}$ m^2/s for a multicomponent system at 483K.

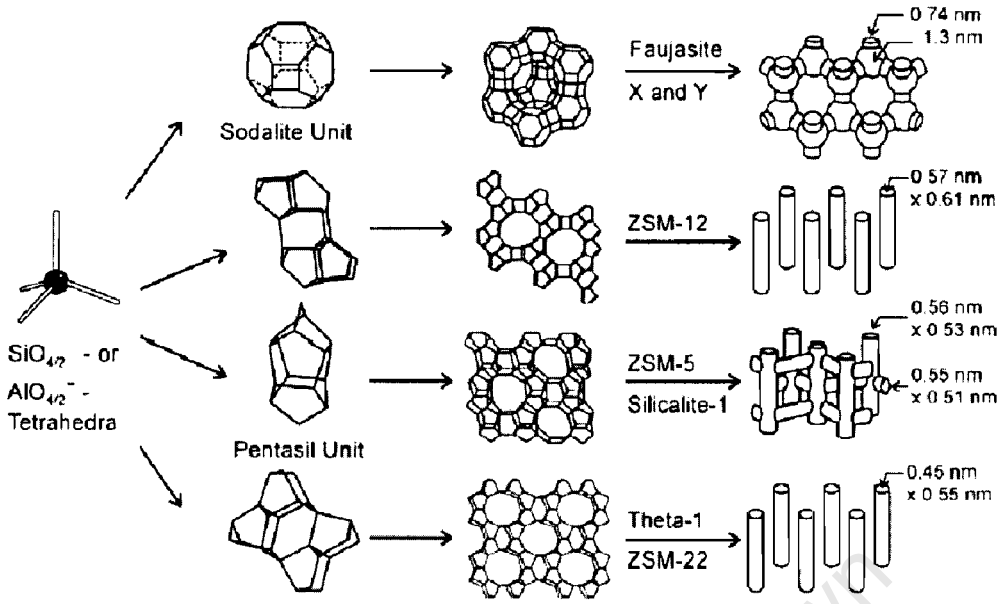

Figure 1.5: Structures of four zeolites. After Weitkamp [2000].

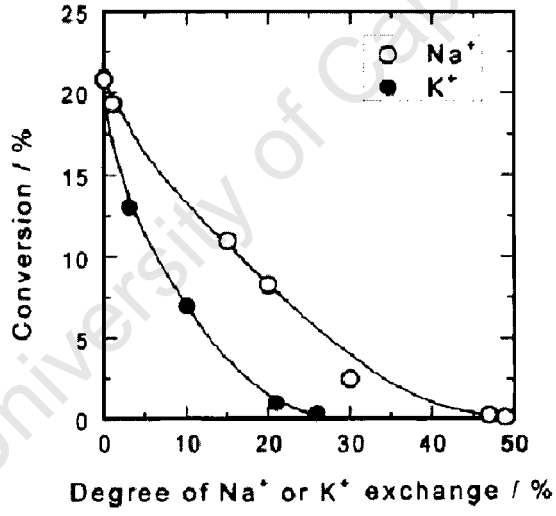

Figure 1.6: Hexane conversion vs Na^+ and K^+ in H-ZSM-5. Reaction conditions: $T = 623K$, $p_{hexane} = 8kPa$, Contact time (W/F) = 1.3 g h mol^{-1}. After Baba et al. [1996].

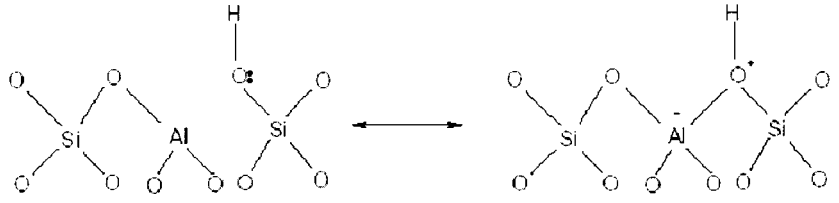

Figure 1.7: The structure of Brønsted sites in zeolites. After Haag and Chen [1987].

molecules, and z/x the silicon/aluminum ratio.

Among the many properties that make these materials desirable are:

- *Stability.* Many zeolites can withstand acidic environments and ionizing radiation. They are also thermally stable to temperatures over 500^oC.
- *Adsorption.* Zeolites have large void fractions with regular uniformly-sized pores that allow or deny access to the channel system based on the size or shape of the guest molecule.
- *Ion Exchange.* The mobility of the counterions that neutralize the matrix makes the zeolite useful in exchanging ions with the surrounding fluid.
- *Miscellaneous.* Zeolites are not toxic and can be regenerated, thus enabling safe and repeated use.

Because of these properties and others, zeolites are being used in a very wide spectrum of technologies, including fine chemical synthesis, petroleum refining, wastewater treatment [Breck, 1974; Barrer, 1978; Venuto, 1994; Bowman, 2003; Cundy and Cox, 2003], groundwater remediation and many other applications reviewed elsewhere [Davis, 1991; Derouane, 1998; Tsai et al., 1999; Weisz, 2000; Stone, 2003].

1.5 Zeolite ZSM-5

Zeolite ZSM-5 was first synthesized in the laboratory by Mobil workers [Argauer and Landolt, 1972]. Belonging to the MFI-family of 10-membered rings (10 oxygen atoms are connected via silicon atoms to form a ring), this zeolite differs from its silicalite sibling by its aluminum content. The former has a silica/alumina ratio between $5 - 200$, whereas the latter contains very little (if any) aluminum [Szostak, 1992]. Figure 1.8 shows a crystallographic structure of MFI with the dimensions of the intersecting a (sinusoidal) and b (straight) channels.

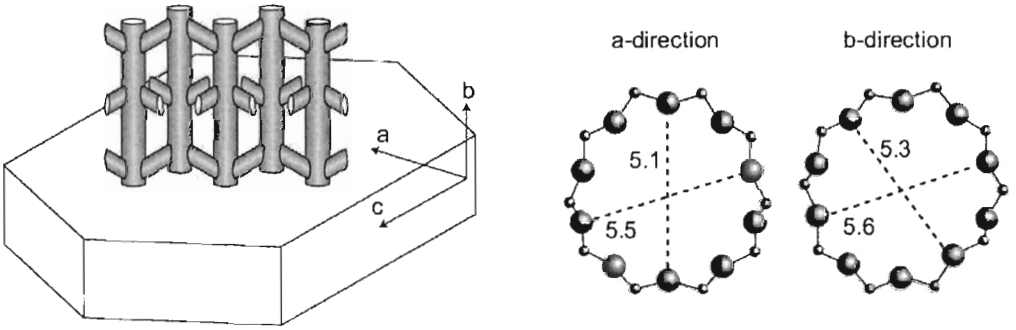

Figure 1.8: MFI channel system with crystallographic axes (shown) and pore dimensions (in Å). After Jareman [2004].

Over and above its zeolitic properties, it is the molecular dimensions of the pores of ZSM-5 that make it ubiquitous in a large range of technologies. For instance, in the production of paraxylene

(pX), large ZSM-5 crystals are highly selective for the para- isomer over its meta- and ortho-equivalents, whose dimensions vary by less than $0.1nm$ (figure 1.9)[Ratnasamy et al., 1986; Tsai et al., 1999; Davis, 2003].

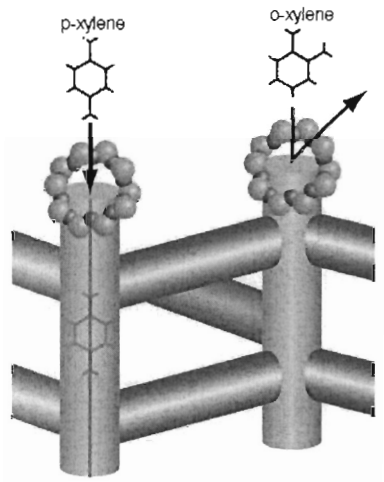

Figure 1.9: Schematic showing the selectivity of ZSM-5 channels to molecules of the same molecular formula but different configurations. After Davis [2003].

1.6 Post synthesis modification of zeolites

Numerous efforts have been pursued to enhance the shape-selective properties of zeolites for application in different technologies. These include steaming and acid washing, cation exchange, the use of large crystals, and the in-situ adsorption of large bases on the external surface. Many researchers review these and other efforts [Szostak, 1991; Chen et al., 1994; Choplin, 1994; Vansant, 1997; Aboul-Gheit et al., 2001; Chen et al., 2002]. Of interest to this work is Chemical Vapor Deposition (CVD) on ZSM-5.

Investigated and reviewed extensively [Chu et al., 1989; Hibino et al., 1991, 1993; Chun et al., 1994; Tynjälä and Pakkanen, 1997; Röger et al., 1998; Impens et al., 1999; Weber et al., 2000; Röger et al., 2001], CVD is a technique whereby access to the non shape selective external surface acid sites can be denied and the ZSM-5 pore mouth narrowed or blocked in order to advantage diffusion of the species with the optimal configuration. Figure 1.10 illustrates how in theory, by using a silicon alkoxide, the deposited silica could reduce the width of the pore mouth. Röger et al. [2001] have since refuted the pore narrowing theory in favor of pore blocking.

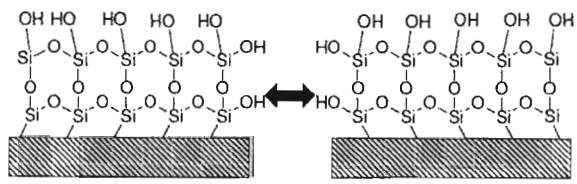

Figure 1.10: Pore narrowing effect of silica deposition. After Hibino et al. [1993].

1.7 Zeolite film synthesis

A continuous layer of zeolite resting on a non-porous support constitutes a zeolite film (figure 1.11). When the support is porous, a membrane results. Zeolite films and membranes belong to a bigger group of catalysts known as *structured catalysts*, and that the first book on these catalysts was published six years ago [Cybulski and Moulijn, 1998] is testimony to the novelty of their design. Attributes that make zeolite films and membranes interesting to researchers and

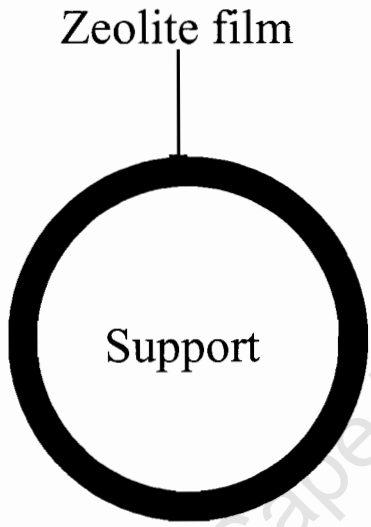

Figure 1.11: Schematic cross-section of a zeolite film on a spherical support.

industry include:

- Elimination of the macropores characteristic of pellets.
- Films and membranes enable the simultaneous reaction and separation of molecules.
- They are able to withstand harsh environments.
- When packed in a reactor, their configuration allows for a low pressure drop.

These and others make zeolite films and membranes a subject of great interest in a wide range of applications including chemical sensors, air purifiers, autocatalytic converters, and microelectronic devices. The challenge remains, though, to make these materials cheaper [van Bekkum et al., 1994; den Exter et al., 1996; Bein, 1996; Vroon et al., 1998; Saracco et al., 1999; van der Puil et al., 1999; Chiang and Chaob, 2001; Dixon, 2003; Doyle et al., 2003].

Bein [1996] discusses three techniques for the synthesis of supported zeolite films. Figure 1.12 is a schematic of these. With method I, pre-synthesized crystals are deposited on the substrate. Method II involves the use of a precursor solution that - under hydrothermal conditions - forms seed crystals on the support, which sometimes supplies the nutrients required for growth. Method III also uses a precursor solution under hydrothermal conditions, but with preformed seed crystals. These and other methods of supported film and membrane synthesis, including slurry dip

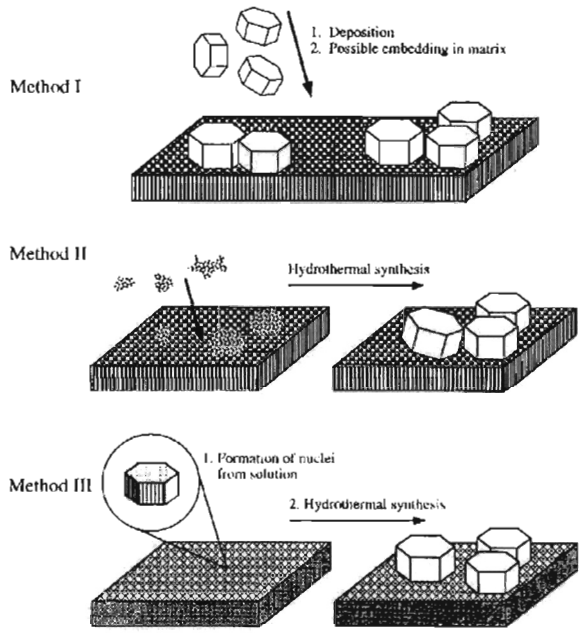

Figure 1.12: Techniques for the synthesis of zeolite films. After Bein [1996].

coating, selective etching, and vapor phase transformation, have been reported and reviewed [Davis and Lobo, 1992; Nakazawa et al., 1998; Hedlund, 1998; Tavolaro and Drioli, 1999; Wong et al., 2001a,b].

1.8 Seed-film technique

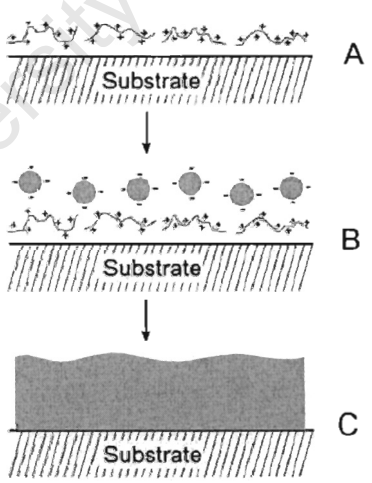

Figure 1.13: Schematic representation of the seed-film method. (**A**) Preparation of substrate; (**B**) adsorption of seed crystals; (**C**) film growth. After Sterte et al. [2001].

The seed-film technique [Hedlund et al., 1997; Sterte et al., 2001] is essentially a three-step method to prepare continuous zeolite films (figure 1.13). Firstly, the substrate or support on which the film will be synthesized is prepared for adsorption of seed crystals. This is done by treating it with a cationic polymer. Negatively charged silicalite seeds are then electrostatically adsorbed onto the support. Lastly, the seeded support is submerged into a synthesis solution

that - under hydrothermal conditions - supplies nutrients required for the growth of the discrete seed crystals into a dense and continuous zeolite film (figure 1.14).

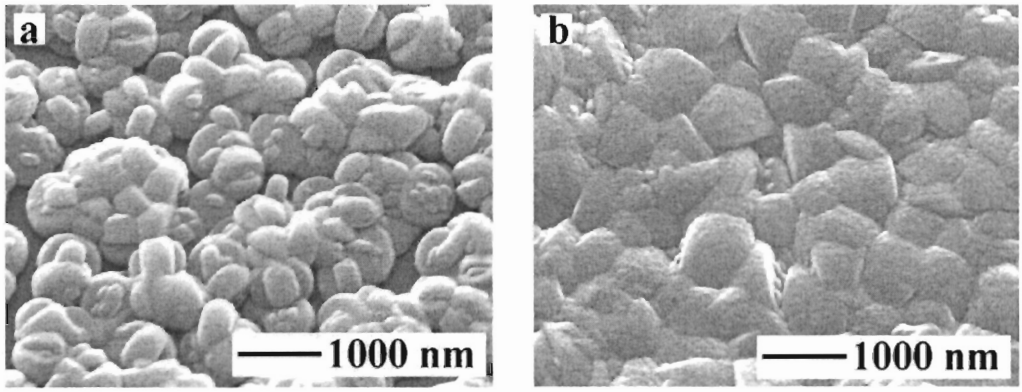

Figure 1.14: SEM images showing zeolite film growth on a support: (**a**) non-continuous film after 24 hours in synthesis mixture; (**b**) a dense continuous film after 96 hours of hydrothermal synthesis. After Hedlund et al. [1999a].

1.9 Parameters affecting zeolite film properties

Numerous factors such as:

- the use of templating agents during film synthesis;
- the size of the seed crystals;
- the nature, composition and properties of the support ;

affect the properties of zeolite films and membranes synthesized using the seed-film method [Davis and Lobo, 1992; Jansen et al., 1998; Hedlund, 1998; Tavolaro and Drioli, 1999]. However, this section will focus on those pertinent to the goal of this work.

ZSM-5 films and membranes prepared using the seed-film method are dogged by cracks (figure 1.15(a)), which are caused by the high temperature removal of the templating agent used during film synthesis [Nishiyama et al., 1995; Bein, 1996; Mintova et al., 1997; Yan et al., 1997; Mintova et al., 1998; Vroon et al., 1998; Wegner et al., 1999; Hedlund et al., 1999b; Dong et al., 2000; Lai et al., 2003].

However, other discontinuities such as grain boundaries can also have undesirable effects on the resultant molecular sieve. For instance, Vroon et al. [1998], Nair et al. [2001] and Au and Yeung [2001] show that grain boundaries can allow nonzeolitic diffusion. As shown in figure 1.15, the number of grain boundaries per unit area decreases with increasing membrane/film thickness [Au and Yeung, 2001; Jareman, 2004].

In their investigation of the parameters affecting the properties of films prepared using the seed-film method, Hedlund et al. [1999a] and Li et al. [2001] found the following:

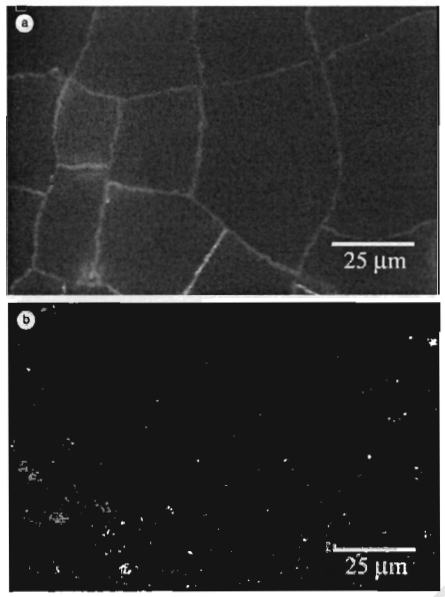

Figure 1.15: Confocal microscope images of dye-infiltrated MFI membranes prepared using the same synthesis recipe:(a) $15\mu m$ membrane showing cracks but no grain boundaries and (b) $1\mu m$ membrane showing grain boundaries. The dye cannot enter the micropores. Both membranes were supported on α-alumina. After Nair et al. [2001].

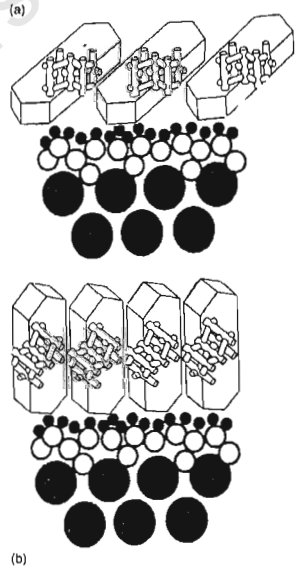

Figure 1.16: A schematic showing changing film orientation.**(a)** Straight channels perpendicular to the support; **(b)** sinusoidal channels perpendicular to the support. After Caro et al. [2000].

- The film's orientation changes with *film thickness* and *size* of the seed crystals. In very thin films (<200 nm), the crystals are preferentially oriented with the a-axis (sinusoidal channels) or the b-axis (straight channels) perpendicular to the substrate surface. As the film thickens (≈ 1000 nm), a larger fraction of the crystalline material (grown twins) becomes oriented with the a-axis perpendicular to the substrate surface. However, in very thick films (>2000 nm), most of the crystalline material has adapted an orientation with both the a- and b-axis pointing away from (but not perpendicular to) the support surface.
- When large seeds are used, the amount of adsorbed seeds has a larger influence on the preferred orientation. This is as a result of growth competition between neighboring crystals and, because of the thickness-orientation relationship stated above, the fact that after the same crystallization time, thicker films are formed from larger crystals.

Figure 1.16 is an illustration of two possible ZSM-5 film orientations on supports.

In MFI-type zeolites, a change in the crystal orientation has implications on the effective diffusivity because the latter depends on the tortuosity of the diffusion path. The pore dimensions, which are not the same for the straight and sinusoidal channels (figure 1.8), also affect the diffusivity of reactant or product species. Using gravimetric and frequency-response techniques, Song and Rees [2000] found that in silicalite-1, the diffusion coefficients of para-xylene in the straight channels are about one order of magnitude higher than in the sinusoidal ones.

Returning to figure 1.14, it can be seen that as the film grows, it gets smoother. Hedlund et al. [1999a] warned against the intuition that, based on their smoothness, thick films could be assumed to be free of defects. Nonetheless, in the absence of other thickness-dependent defects, the external surface area of the thick film can be expected to decrease with increasing film thickness.

1.10 Probe reactions

In numerous scientific studies it has been shown that carefully chosen probe reactions can be excellent diagnostic tools in the characterization of solid catalyst properties [Dewing, 1984; Martens et al., 1988; Garcia and Weisz, 1990, 1993; Amelse, 1993; Das et al., 1994; Weitkamp and Ernst, 1994; Klemm and Emig, 1997; Röger et al., 2001; Manstein, 2001], and in many instances, they may well be the only recourse in the study of the microporosity typical of many molecular sieves [Sun et al., 2003].

While this indirect technique of studying catalytic properties of materials can be complicated (as demonstrated by Wei [1982] in applying mathematical studies of complex reaction systems [Wei and Prater, 1962; Wei, 1962a,b]), the benefits are direct when these reactions are of commercial interest, as is the case with paraxylene isomerization and toluene disproportionation in zeolite ZSM-5.

The use of probe reactions in heterogeneous organic catalysis over zeolites has come a long way in advancing the understanding of the physicochemical phenomena characteristic of the catalytic reactions that occur in the zeolite matrix. The contributions of researchers of note towards this end have been reviewed [Venuto, 1994].

1.10.1 Paraxylene isomerization

The similarity of the dimensions of the xylene isomers to each other and to those of the internal pore spaces of ZSM-5 make xylene isomerization a superb probe reaction for the study of shape-selective properties of this zeolite. 20 years after he had presented a theoretical model on diffusion effects in complex reaction systems of first order reactions [Wei, 1962a,b], Wei [1982] applied it in the development of a mathematical theory of enhanced para-xylene (pX) selectivity in ZSM-5. To do this, he constructed a simple linear first order reaction model and showed how diffusion effects change the apparent reaction scheme from a linear (or series) to a triangular (or series-parallel) scheme (figure 1.17). Experimentally, this apparent change in reaction scheme manifests itself in a molar $mX : oX$ ratio that decreases with increasing diffusion resistance.

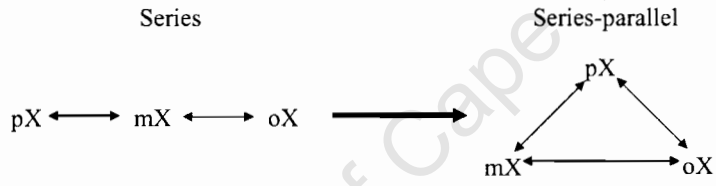

Figure 1.17: Diffusion effects on pX isomerization from linear to triangular scheme.

In his appraisal of meta-xylene isomerization as a probe reaction in the characterization of various zeolites, Dewing [1984] presented equation 1.2, whereby the intrinsic relative rate constant of the reaction can be extracted from the observed.

$$\left(\frac{k_{mX\rightarrow oX}}{k_{mX\rightarrow pX}}\right)_{observed} = \sqrt{\frac{D_{oX}}{D_{pX}}\left(\frac{k_{mX\rightarrow oX}}{k_{mX\rightarrow pX}}\right)_{intrinsic}} \tag{1.2}$$

Weitkamp and Ernst [1994] presented a comprehensive survey of the meta-xylene isomerization reaction in shape-selective catalysis.

In large intracrystalline cavities (e.g. zeolite Y), the acid-catalyzed pX isomerization is accompanied by disproportionation (figure 1.18), resulting in lower xylene yields and significant amounts of trimethylbenzene (TMB) [Lanewala and Bolton, 1969; Collins et al., 1983; Olson and Haag, 1984; Guisnet et al., 2000].

However, the restrictive space in ZSM-5 pores cannot accommodate the diphenylmethane-type intermediate. Hence the intermolecular model cannot hold [Llopis et al., 2004]. Olson and Haag [1984] showed that the intramolecular mechanism (figure 1.19) prevails in ZSM-5, and attributed it to *transition state selectivity*, which prohibits formation of large intermediates.

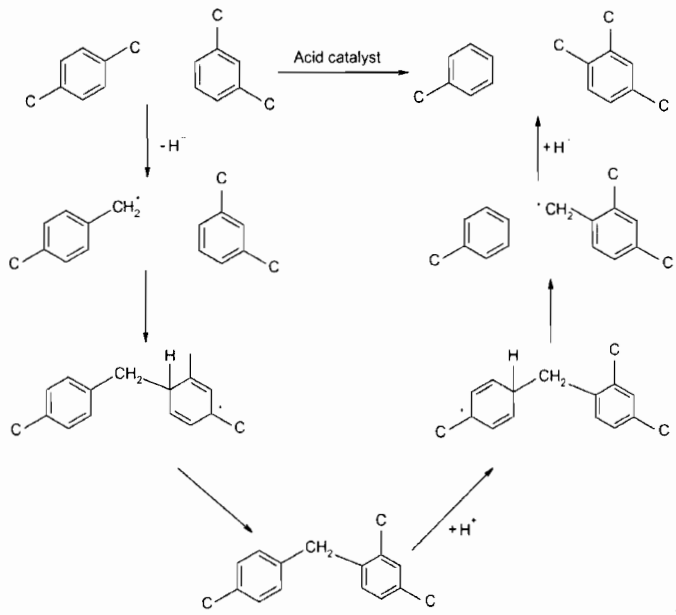

Figure 1.18: (*Intermolecular*) Disproportionation mechanism. [Olson and Haag, 1984].

Commercially, paraxylene is typically produced by converting a ethylbenzene (EB) - xylene mixture. Table 1.2 shows typical compositions and process conditions of two xylene processes, the Mobil Vapor Phase Isomerization (MVPI) and the Mobil High Temperature Isomerization (MHTI).

The feed for these processes usually comes from pyrolysis gasoline from steam reforming, toluene disproportionation (TDP), catalytic naphta reformate, and coke-oven light oil.

Table 1.2: Product analysis from a commercial xylene isomerization process. After Chen et al. [1996].

	MVPI[a]	MHTI[b]
Feed(wt%)		
Xylenes and EB	100	100
Hydrogen	0.1	0.2
Total	100.1	100.2
Products(wt%)		
Fuel gas	0.8	4.7
Benzene	7.7	11.2
Toluene	1.2	1.8
p-Xylene	77.9	80.1
C9 aromatics	12.5	2.4
Total	100.1	100.2

[a]Process conditions [Cannella, 1997]: WHSV=2-50 hr^{-1}; T=315-370°C; H_2/HC molar ratio= 6 : 1; P = 1480 kPa

[b]Process conditions [Cannella, 1997]: WHSV=10-12 hr^{-1}; T=427-460°C; H_2/HC molar ratio=1.5-2.1; P=1480-1825 kPa

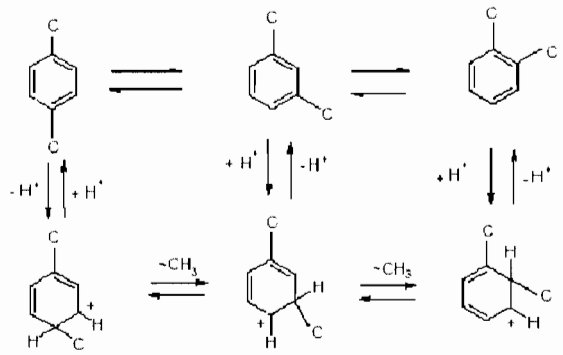

Figure 1.19: (*Intramolecular*) isomerization mechanism. [Olson and Haag, 1984].

1.10.2 External surface activity - 1,3,5-Triisopropylbenzene cracking

The large kinetic diameter (8.5Å,[Hibino et al., 1993]) of the 1,3,5-triisopropylbenzene (TIPB) molecule precludes it from reaching the internal catalytic sites of ZSM-5 (d = 5.5Å). Within limits[2], its chemical conversion is therefore indicative of the extent of external surface acid sites[3] on the catalyst.

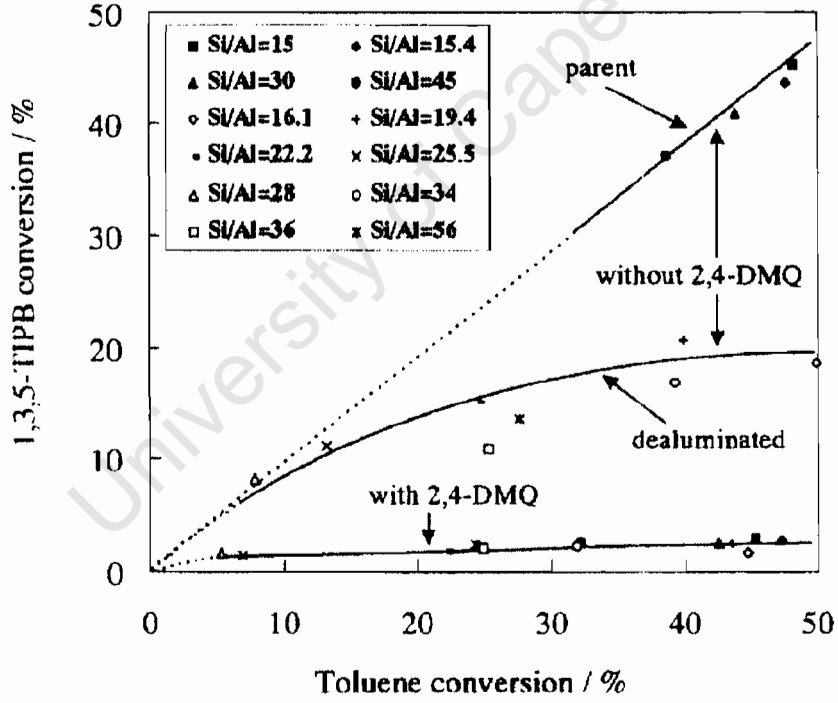

Figure 1.20: Conversions of 1,3,5-TIPB and TDP on MCM-22. After Wu et al. [1998].

Wu et al. [1998] successfully used TIPB cracking[4] in their study of the catalytic properties of MCM-22 in toluene disproportionation (TDP) (figure 1.20). Namba et al. [1986a] also used TIPB

[2]At long residence times, 1,3,5-TIPB tends to coke (on zeolites), thereby reducing conversions [Al-Khattaf and de Lasa, 2002; Mahgoub and Al-Khattaf, 2004].

[3]Farcasiu and Degnan [1988] demonstrate the impact of external surface acid sites on the effectiveness of zeolites and propose a modified effectiveness factor that accounts for it.

[4]T = 573K, p_{TIPB} = 8.8kPa, Q_{He} = 30 ml min^{-1}, W/F = 1.25 g h mol^{-1}.

cracking[5] to show that dealumination of NaZSM-5 by $SiCl_4$ was limited to the external surface of the ZSM-5 crystallites.

Namba et al. [1986b], Hibino et al. [1991, 1993], Čejka et al. [1996], Röger et al. [2001] and [Manstein, 2001] successfully used TIPB cracking in their investigation of the effects of external surface modification of ZSM-5 via chemical vapor deposition (CVD) with alkoxysilanes on its shape selective properties.

In zeolite films, the prevalence of defects (e.g., cracks and grain boundaries) larger than the zeolite's channel dimensions may mean more active sites are accessible to the TIPB molecules than would be anticipated.

1.11 Objectives of this thesis

- Characterize the physical and catalytic properties of supported Zeolite ZSM-5 films prepared using the seed-film technique.
- Investigate the effect of support type and film thickness on the intrinsic catalytic properties.
- Investigate the effect of chemical vapor deposition of tetraethoxysilane on the catalytic properties of ZSM-5 films supported on sand.

[5] T = 548K, p_{TIPB} = 10kPa, Helium carrier gas, W/F = 4.1 g h mol^{-1}.

Chapter 2

Experimental

ZSM-5 films were grown on quartz, alumina and sand supports using the stepwise seed-film method outlined in §1.8. Subsequent to physical characterization, probe reactions were conducted to investigate the intrinsic properties of these films, and the effects of support type and film thickness. One of the films was then coated with silica (via CVD) and its intrinsic catalytic properties monitored. This chapter describes these experiments.

2.1 Film synthesis and physical characterization

Supports on which the films were synthesized are sand (Merck), alumina (Vereinigte Füllkörper-Fabriken), and quartz (Merck). Their properties are summarized in table 2.1.

The seed-film technique [Hedlund, 1998] was employed in growing the films. In a stepwise fashion, ZSM-5 films ($Si/Al = 50$) were synthesized on all three support types to the following approximate thicknesses (in nm and with an error of 10%): 150, 350, 800, and 2300 after 1, 2, 6, and 18 hydrothermal synthesis steps, respectively.

Tetra-propyl-ammonium-hydroxide (TPAOH, AppliChem, GmbH, Germany) and tetra-ethoxy-silane (TEOS, Sigma-Aldrich) were used as template and silica source, respectively. Using a synthesis solution with the molar composition 9TPAOH: $25SiO_2$: $360H_2O$: 100EtOH, a colloidal

Table 2.1: Physical properties of supports.

Support	External surface area(BET) $(m^2/g)\times10^3$	External surface area[a] $(m^2/g)\times10^3$	Density g/cm^3	Composition	Pore vol. cm^3/g	Diam. (mm)
Quartz	3.6	0.77	2650	>99%SiO_2	N/A	2.5-4
Sand	170	110	2650	>99%SiO_2	N/A	0.1-0.3
Alumina	90	0.77	2650	>99%Al_2O_3[b]	2.4×10^{-4}	3

[a]Theoretical, assuming non-porous spherical particles.
[b]According to the vendor, 0.4-0.5wt% of the alumina is $Na_2O + K_2O$.

solution of 60 nm silicalite-1 seed crystals was prepared over a 2 week period under hydrothermal synthesis (60℃). Following repeated centrifugation to purify it, the sol was re-dispersed in distilled water. The final sol had 0.9 wt% solids and a pH of 10.0. The supports were placed in a quartz glass container with a conical bottom outlet. They were then rinsed thoroughly with a dilute ammonia solution (0.1 M) and acetone. To render them positively charged, the supports were treated with a cationic polymer solution (0.4 wt% Redifloc 4150, Eka Chemicals) prepared as prescribed by Lassinantti et al. [2000]. They were then rinsed six times with a 0.1 M ammonia solution[1] in order to remove excess polymer. Then the seed sol was added to the container and seeds electrostatically adsorbed onto the supports. To remove excess seed crystals, the ammonia solution was again used six times to rinse the seeded supports.

Next, a film was grown by hydrothermal synthesis on the seeded surface of the support. A synthesis solution with a molar composition of 3 TPAOH: 25 SiO_2: 0.25 Al_2O_3: 1 Na_2O: 1600 H_2O: 100 EtOH was prepared using a mixture of aluminum isopropoxide (Sigma-Aldrich), TPAOH, H_2O and NaOH solution (Riedel-de Haën). TEOS was added to the mixture in a polypropylene bottle. The resultant synthesis solution was poured in the quartz glass container until the supports were fully covered. It was then submerged in a heated oil bath at 75℃ under reflux for 48 hours per hydrothermal synthesis step. After each step, the sample was removed from the oil bath and allowed to cool, after which the supports were rinsed six times with the dilute ammonia solution and a fresh synthesis solution added for the next synthesis step. After the last synthesis step, the samples were rinsed in the ammonia solution for 4 days prior to their removal from the synthesis beaker. The samples were then calcined at 400℃ using a heating rate of 0.2℃. Cooling was controlled to 0.3℃/min. Ion exchange then ensued in a 10% NH_4NO_3 solution at 100℃ for 1 hour. The samples were then calcined again as just described.

Images of the films were obtained using a Phillips XL 30 SEM (20 kV) with a LaB6 emission source to measure film thickness and compare the roughness of the samples. Preparation involved mounting the samples in resin (LR White, London Resin Company Ltd.) and, in the case of samples used to obtain profiles (*i.e*, side view) of the films, polishing. To remove the resin, the samples were calcined prior to analysis. They were sputter-coated with gold.

A Micromeritics ASAP 2010 was used to collect nitrogen adsorption data at 77 K, with a sample size of ≈10 grams and pressure range of $0.05 < P/P_o < 0.2$. The zeolite loading (*i.e.*, amount of zeolite per amount of sample), was determined using nitrogen adsorption data. Using this data and the specific surface area of a ZSM-5 powder[2] (415 $\frac{m^2}{g\ zeolite}$), the zeolite loadings ($\frac{g\ zeolite}{g\ catalyst}$) were computed.

Inductively coupled plasma atomic emission spectroscopy (ICP-AES) was used to measure the sodium and silicon content in bulk crystals. X-ray photoelectron spectroscopy (XPS) was performed to analyze the Si/Na ratio at the surface (to a depth of ≈6 nm) of the particles. A KRATOS Axis ultra electron spectrometer (225 W) using a monochromated Al Kα source was used to record the spectra.

[1] each time they were rinsed, a fresh solution was used.

[2] The powder was synthesized with a recipe similar to that used to grow the films [Öhrman et al., 2001].

In order to investigate the efficiency of the ion-exchange procedure, energy dispersive X-ray (EDX) and XPS analyses were conducted on the quartz and alumina samples, respectively.

2.2 Reaction characterization

The intrinsic catalytic properties of the films were investigated at atmospheric pressure in a fixed bed reactor using pX isomerization for overall reactivity and TIPB cracking for external surface activity. A flowsheet of the apparatus, which was also used for silanisation, is shown in figure 2.1. Air was used for calcination, and Argon (Ar) as carrier gas for the test and silanisation reactions. A pressure build-up was prevented by adjusting the needle valve (N).

A 250 mm long tubular reactor (figure B.1, Appendix B) with an internal diameter of 17 mm was used for the catalytic experiments. A 1/8 inch tube in the centre of the reactor served as a thermo-well and contained a thermo-couple, which was used for temperature measurements during the tests. The reactor was loaded with sample, and glass beads without zeolite (d= 2 mm) were used to fill the rest of the reactor up- and downstream of the sample. To separate the packing from the sample, stainless steel gauzewire with glass wool were placed between them. The reactor was heated from room temperature to 450℃ at a rate of 1.8℃/min under flowing synthetic air. The sample was calcined in the reactor for at least 3 hours prior to and in-between tests. The feed was argon saturated at 60℃ with p-xylene (>99%, Saarchem) or 1,3,5-tri-isopropyl benzene (TIPB, >97%, Aldrich) (figure B.2, Appendix B). The p-xylene contained 0.1% m-xylene and 0.035% o-xylene. The saturated gas was fed to the reactor operating at 450℃. The product from the reactor was analysed by an on-line HP 5890 Gas Chromatograph (GC) equipped with a polar column (BP-xylenes, SGE). Table 2.2 shows the GC temperature program. Hydrogen was used as carrier gas.

2.2.1 Reaction Conditions

Both test reactions were conducted at 450℃, and the hydrocarbon concentration in the reactor was 1.13 mol p-xylene/m^3 and $1.55 \cdot 10^{-2}$ mol TIPB/m^3, corresponding to partial pressures of 6.82 kPa p-xylene and 93 Pa TIPB. The partial pressure of p-xylene was determined using the Antoine equation, while the partial pressure of TIPB was measured indirectly, by comparing the GC peak areas for TIPB and p-xylene, assuming proportionality between area and number of

Table 2.2: Gas Chromatograph temperature program.

	Temperature Program		
	Units	pX	TiPB
Initial oven temperature	℃	40	150
Initial time	min	12	inf
Temperature ramp	℃/min	5	N/A
Final temperature	℃	90	150
Final time	min	0	N/A

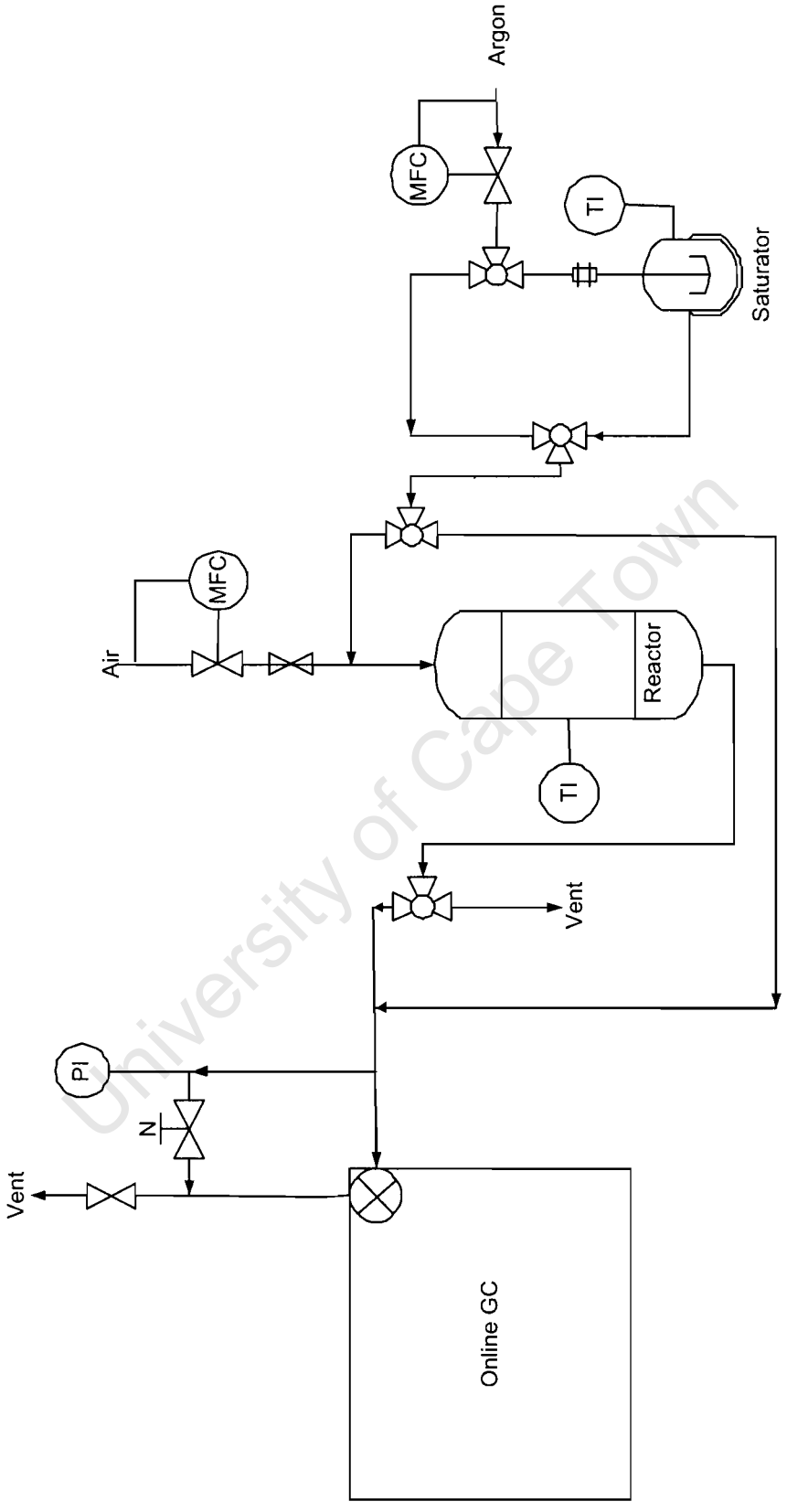

Figure 2.1: Flowsheet of reaction apparatus

carbon atoms. Further reaction conditions[3] are given in tables 2.3, 2.4, and 2.5.

Table 2.3: Reaction conditions for experiments on ZSM-5 films supported on sand.

Thickness nm	Run ID	Reactant	$m_{catalyst}$ g	$m_{zeolite}$ g	bed height cm	WHSV 1/hr	$\dot{v}_{cg}$ ml/min
150	1	pX	7.0	0.051	2.28	5.5-27	16-80
150	2	pX	7.1	0.051	2.28	5.5-28	16-80
150	3	TiPB	7.0	0.051	2.28	0.41-0.55	40-80
150	4	TiPB	7.0	0.051	2.28	0.41-0.68	40-80
350	5	pX	7.2	0.079	2.35	4.5-18	10-80
350	6	pX	3.0	0.033	0.978	9.1-45	10-80
350	7	TiPB	7.2	0.079	2.35	0.27-0.45	40-80
350	8	TiPB	3.0	0.033	0.978	0.54-0.91	40-80
800	9	pX	8.0	0.23	2.61	0.69-6.9	25-80
800	10	pX	3.0	0.087	0.978	2.1-17	10-80
800	11	TiPB	8.0	0.23	2.61	0.069-0.17	25-80
800	12	TiPB	3.0	0.087	0.978	0.34-1.4	24-80
2300	13	pX	3.0	0.23	0.978	0.79-6.6	20-80
2300	14	pX	1.0	0.076	0.326	2.6-19	20-80
2300	15	TiPB	3.0	0.23	0.98	0.053-0.13	25-80
2300	16	TiPB	1.0	0.076	0.326	0.13-0.53	10-30

Table 2.4: Reaction conditions for experiments on ZSM-5 films supported on alumina.

Thickness nm	Run ID	Reactant	$m_{catalyst}$ g	$m_{zeolite}$ g	bed height cm	WHSV 1/hr	$\dot{v}_{cg}$ ml/min
150	17	pX	36	0.090	10	2.0-16	10-80
150	18	TiPB	36	0.090	10	0.12-0.40	10-80
350	19	pX	36	0.25	10	0.73-5.8	10-80
350	20	TiPB	36	0.25	10	0.044-0.15	10-80
800	21	pX	36	0.49	10	0.37-2.9	10-80
800	22	TiPB	36	0.49	10	0.022-0.074	10-80
2300	23	pX	36	0.72	10	0.25-2.0	10-80
2300	24	TiPB	36	0.72	10	0.015	80
2300	23	pX	6	0.12	1.6	1.5-12	10-80
2300	24	TiPB	6	0.12	1.6	0.015-0.050	10-80

Table 2.5: Reaction conditions for experiments on ZSM-5 films supported on quartz.

Thickness nm	Run ID	Reactant	$m_{catalyst}$ g	$m_{zeolite}$ g	bed height cm	WHSV 1/hr	$\dot{v}_{cg}$ ml/min
350	25	pX	29	0.017	8	10-83	4-80
350	26	TiPB	29	0.017	8	10-83	4-80
800	27	pX	30	0.049	8	1.9-31	10-80
800	28	TiPB	30	0.049	8	0.25-0.75	10-80
2300	29	pX	22	0.13	6	1.4-12	15-80
2300	30	TiPB	22	0.13	6	0.085-0.34	15-80

[3]WHSV's were calculated based on zeolite mass, and flowrates($\dot{v}_{cg}$) measured assuming standard temperature and pressure(STP). Because of the high dilution factor, the flow rate of the feed is assumed negligible. Hence the use of the subscript *cg* for 'carrier gas'.

2.3 CVD

On the 350nm sand film, inertization of the external surface acid sites was done at 100℃ using tetraethoxysilane (TEOS) in vapor form ($p_{TEOS} = 1.96kPa$) and argon as the carrier gas at a flowrate of 80 ml/min. With pX and TIPB reactions done prior to each silica deposition step, and calcination after each reaction, the process was repeated over 15 deposition cycles, and figure 2.2 shows the sequence of reactions constituting a typical silica deposition cycle.

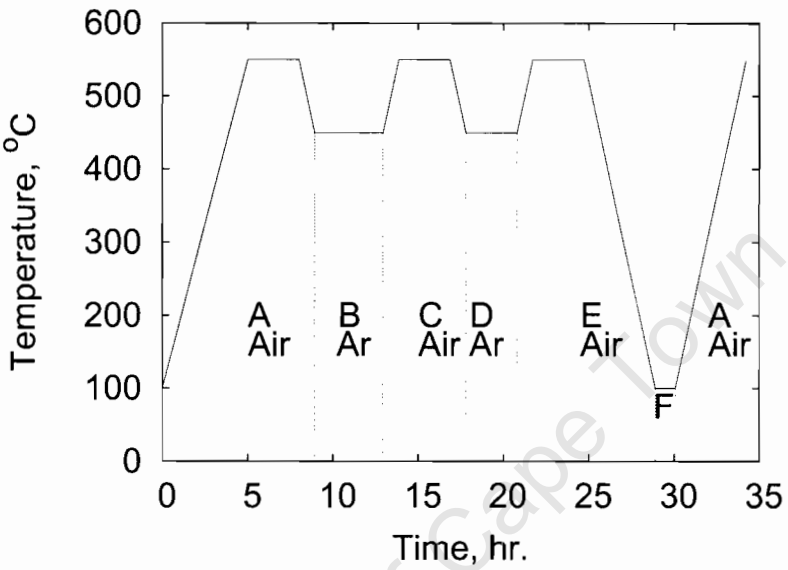

Figure 2.2: Sketch of one complete inertisation and test reaction cycle. A,C,E = calcination. B,D = probe reactions. F = CVD (under Argon). Air is for calcination and Ar(gon) the carrier gas.

2.4 Evaluation of Catalytic Reaction Data

2.4.1 Molar flow rates

Referenced at standard temperature T^o and pressure P^o, the volumetric flowrate of the carrier gas determined the molar flow rates. For the carrier gas and the feed, the molar flowrates are, respectively:

$$\dot{n}_{cg} = \left(\frac{P^o \dot{v}_{cg}}{RT^o}\right)_{STP} \tag{2.1}$$

and,

$$\dot{n}_{feed} = \frac{\dot{n}_{cg} p_{vap-feed}}{p_t otal - p_{vap}} \tag{2.2}$$

where $\dot{n}_{cg}$ is the carrier gas molar flow rate, $p_{vap-feed}$ the feed vapor pressure at the saturator temperature , $p_t otal$ the total pressure in the saturator, and $\dot{n}_{feed}$ the molar flow rate of the feed.

2.4.2 Concentrations

The ideal gas law governed the concentrations of the feed:

$$c_{feed} = \left(\frac{\dot{n}_{feed}}{\dot{v}_{cg}}\right)_{T_R} \tag{2.3}$$

where T_R is the reaction temperature.

2.4.3 Conversion, X_i

For each reactant, the conversion was defined as:

$$X_{feed} = \left(\frac{\dot{n}_{feed,in} - \dot{n}_{feed,out}}{\dot{n}_{feed,in}}\right) \times 100\% \tag{2.4}$$

2.4.4 Selectivity, S_i

The selectivity, S_i, for any product i of the xylene isomerization was defined as

$$S_i = \frac{\dot{n}_i}{\sum_{products} \dot{n}_i} \tag{2.5}$$

where $\dot{n}_i$ is the molar flow rate of product species i. Instead of molar flow rates, molar concentrations can also be used. Because ZSM-5 does not produce many side reactions (discussed in §1.10.1) at the conversions relevant to this work, the product xylene isomers are the only species considered in computing S_i. This definition excludes the feed species, *i.e.*, pX. As an example, for the xylene isomerization reaction (with negligible side reactions), it is:

$$S_{mX} = \frac{c_{mX}}{c_{mX} + c_{oX}} \tag{2.6}$$

2.4.5 Yield, Y_i

The yield of product i is the ratio of its concentration c_i to that of all reactants and products. For instance, in the isomerization of pX, the mX yield (on a benzene-free basis, [Manstein et al., 2002]) is:

$$y_{mX} = \frac{c_{mX}}{c_{mX} + c_{oX} + c_{pX}} \tag{2.7}$$

2.4.6 Residence time, τ

The residence time for the xylene isomerization reactions was defined as:

$$\tau = \frac{V_z}{\dot{v}_{cg}} \tag{2.8}$$

where V_z is the volume of catalyst. In the case of TiPB cracking a modified residence time based on apparent external surface area A_z was used, such that:

$$\tau_m = \frac{A_z}{\dot{v}_{cg}} \tag{2.9}$$

If it is assumed that the film can be approximated by a slab of uniform thickness (T_f), the apparent external surface area can be calculated using equation 2.10:

$$A_z = \frac{V_z}{T_f} \tag{2.10}$$

2.4.7 Effectiveness factor, η_i

Because of the difficulty to extract an explicit equation for the effectiveness factor, it was evaluated numerically, such that:

$$\eta_i = \int_0^V \frac{r_i}{(r_i)_{surface}} dV \tag{2.11}$$

2.4.8 Thiele modulus, ϕ_{pX}

Aris [1975] defines a Thiele modulus for reversible first order reactions. At low conversions this provides a first approximation to the Thiele modulus of pX isomerization.

$$\phi_{pX} = T_f \left(\frac{k_{pX}}{D_{pX}} + \frac{k_{pX}}{Ke_1 D_{mX}} \right)^{0.5} \tag{2.12}$$

Also for this case, $\eta_{pX} = \frac{tanh(\phi_{pX})}{\phi_{pX}}$ is a first approximation to the pX effectiveness factor.

2.4.9 Carbon balance, CB%

To check the carbon balance and the integrity of the reaction system, a comparison was made between the carbon entering the reactor (bypass) and the carbon leaving the reactor (online). As all the components were essentially xylene isomers, the response factors cancel out and are thus unnecessary.

$$CB\% = \frac{\sum A_{peak,bypass} - \sum A_{peak,online}}{\sum A_{peak,bypass}} \cdot 100\% \tag{2.13}$$

2.4.10 CVD of TEOS on sample S350

Cyclically, TEOS was deposited (via CVD) for 1 hour on 5 *grams* of sample S350 (*i.e.*, 55 mg zeolite) at 100°C and atmospheric pressure. The flowrate was set at 80 ml/min ($WHSV = 14.7$ $\frac{g_{feed}}{g_{zeolite} \cdot hr}$ and $p_{TEOS} = 0.01964$ bar). Figures 2.3 and 2.4 show the calculation of integral TEOS conversions.

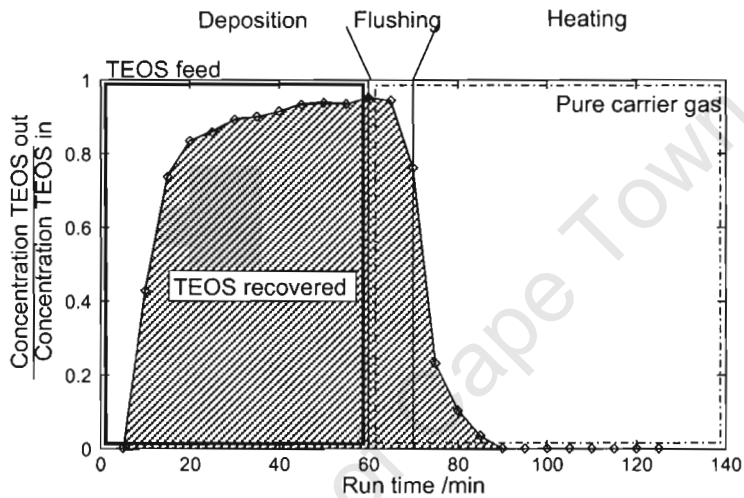

Figure 2.3: Breakthrough curves during CVD of TEOS. After Manstein [2001].

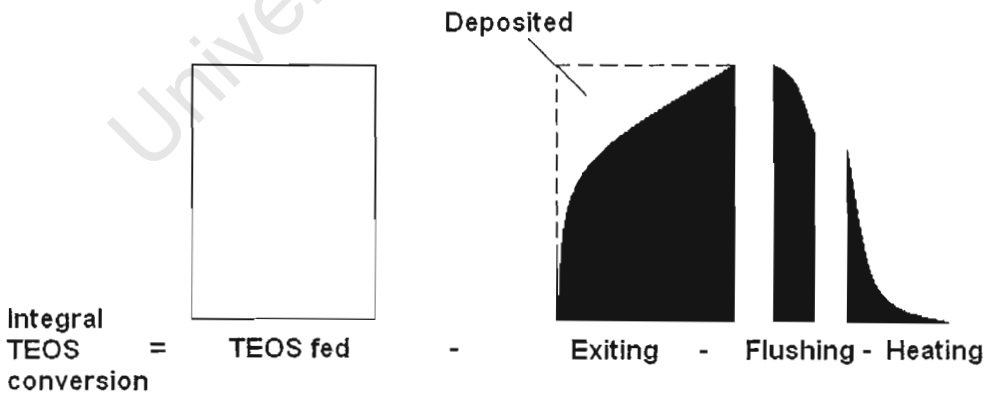

Figure 2.4: Sketch illustrating calculation of integral conversion of TEOS.

To get the integral conversion $X_{TEOS,int}$, the amount of TEOS fed is compared to the total amount of TEOS eluted, such that:

$$X_{TEOS,int} = \left(1 - \frac{n_{TEOSrecovered}}{n_{TEOS,fed}}\right) \times 100\% \tag{2.14}$$

where $n_{TEOS,fed} = \dot{n}_{TEOS,bypass} \times 60min.$

2.4.11 Silica loading

The deposition density of silica Si/nm^2 can be determined [Niwa et al., 1984]:

$$Si/nm^2 = \frac{moles\ TEOS\ deposited}{A_z} \tag{2.15}$$

Assuming the diameter of TEOS is 0.96 nm [Yue et al., 1997], the number of TEOS molecules per monolayer can then be estimated:

$$n_{TEOS,monolayer} = \frac{A_z}{\frac{\pi d_{TEOS}^2}{4}} \tag{2.16}$$

Chapter 3

Reactor model development

In order to draw accurate conclusions from the experimental data, the quantitative characterization has to be underpinned by a good conceptual understanding of the system being investigated. Furthermore, the adoption of correct assumptions about the system simplifies its analysis without compromising accuracy. This section develops the engineering tools used to mimic the experimental data and extract the parameters that describe the properties of the catalysts. The reactions modeled are both para-Xylene isomerization and TIPB cracking.

3.1 Introduction

Assuming a plug flow regime, figure 3.1 is a simplified representation of the global reaction system. The differential volume is further simplified to show that mass transfer occurs not only along the length of the reactor but also from the zeolite particles to the gas surrounding them and vice-versa. At the particulate scale, the system can be represented by the schematic shown in figure 3.2, which shows a cross-sectional model of a ZSM-5 film on a spherical support, and the differential element used to model mass transfer through the zeolite film.

In the development of the reactor model, plate geometry for the zeolite film is assumed. Table 3.1 shows that the film thickness contributes less than 1.2% to the overall radius of the catalyst particle and thus the assumption of flat plate geometry is justified.

Table 3.1: Film thickness to radius ratio for the thickest films

	Alumina	Quartz	Sand
$\frac{T_f}{R}[10^{-2}]$	0.077	0.071	1.2

A simple representation of the mass transfer regimes characterizing the system is shown in figure 3.3, and the cycle of events across the different regions was discussed in §1.2.

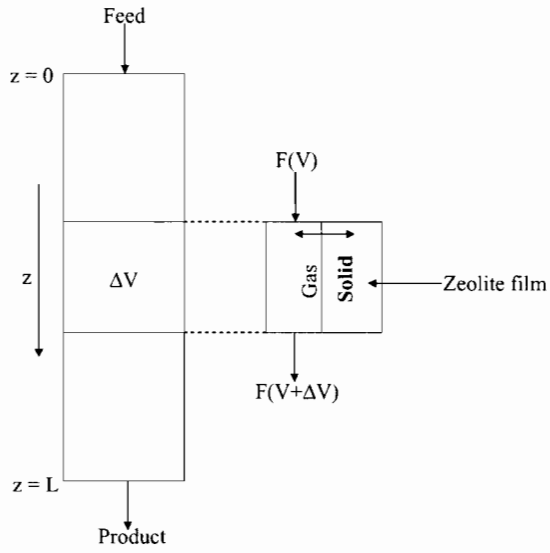

Figure 3.1: Schematic showing a plug flow reactor and a differential plug illustrating mass transfer down the plug and between the zeolite film and the surrounding gas.

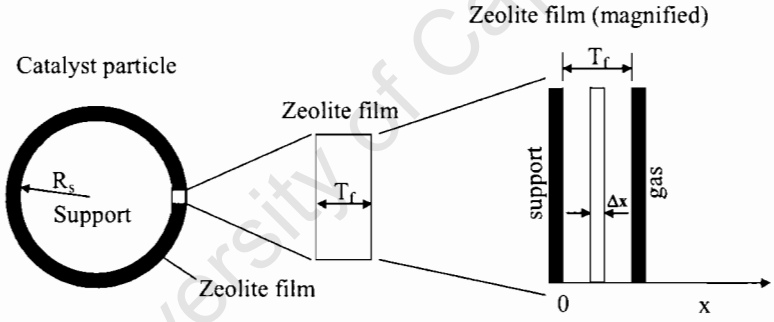

Figure 3.2: Schematic of a catalyst particle and a magnified section of the ZSM-5 film showing a differential element of thickness Δx.

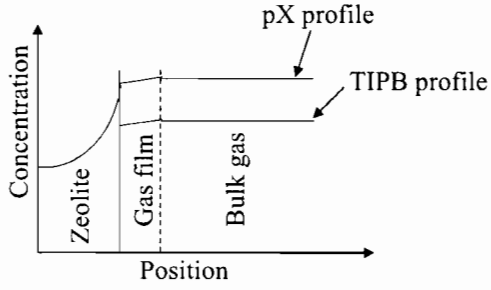

Figure 3.3: Model of transfer of reactants and products between the bulk gas and the zeolite film of thickness Δ x.

3.2 TIPB

Reviewed in §1.10.2, TIPB cracking is a reaction limited[1] to the external surface area of the zeolite matrix. Since the TIPB molecule can only react on an active site, the measured conversion is indicative of the extent of active sites located on the external surface of the zeolite.

3.2.1 Reaction model

On zeolite ZSM-5, the limitation of the TIPB cracking reaction to the external surface active sites implies a definition of the residence time that considers the external surface area of the zeolite instead of its volume. Assuming a constant density system, no external film resistance (see Appendix A.2), a homogeneous distribution of acid sites, and that the reaction follows first order irreversible reaction kinetics, at high temperature (450℃) and low TIPB concentrations ($P_{vap} = 93Pa$), the linear adsorption constant can be lumped with the reaction rate constant (k_{TIPB}) to give equation 3.1 (τ_m is defined in equation 2.9).

$$\frac{dc_{TIPB}}{d\tau_m} = k_{TIPB} \cdot c_{TIPB} \tag{3.1}$$

3.2.2 Estimation of the area-based rate constant, k_{TIPB}

Integration of equation 3.1 and defining $X = 1 - \frac{c_{TIPB}}{c_{TIPB,o}}$ yields equation 3.2:

$$e^{-k_{TIPB}\tau_m} = 1 - X \tag{3.2}$$

Upon linearizing equation 3.2, k_{TIPB} is estimated by determining the slope of the τ_m vs $-ln(1-X)$ curve.

3.3 Para-Xylene isomerization

The assumptions made in modelling this system were:

- the flow regime is that of a plug flow system (Appendix A.2);
- the film is thin enough to allow the use of flat plate geometry;
- Fickian diffusion holds, and diffusion coefficients are independent of position and concentration;
- adsorption kinetics follow linear isotherms;
- acid sites are distributed homogeneously through the film;

[1] The TIPB molecule is too large to access the intracrystalline space of the zeolite film.

- film thickness is uniform and allows a one-dimensional representation; and,
- that the system reaches and maintains steady state.

3.3.1 Reaction kinetics

$$\begin{aligned} pX &\overset{k_{pX}}{\rightleftarrows} mX \\ mX &\overset{k_{mX}}{\rightleftarrows} oX \end{aligned} \tag{3.3}$$

Equation 3.3 represents the first order reversible isomerization of pX. Since the reaction was carried out at high temperature and low xylene vapor pressure, there is a linear relation between the pX concentration in the bulk gas and zeolite adsorbed phase [Chen et al., 1996]. The first order rate expression is therefore employed by lumping together the adsorption equilibrium constants with the rate constants.

Assuming ideal gas behavior, the equilibrium constants K_{e1} and K_{e2} for this reaction are determined from thermodynamic calculations to be 2.25 and 0.475, respectively. Equation 3.4 represents the rate equations for this reaction.

$$\begin{aligned} r_{pX} &= -k_{pX}\left(c_{pX} - \frac{c_{mX}}{K_{e1}}\right) \\ r_{mX} &= k_{pX}\left(c_{pX} - \frac{c_{mX}}{K_{e1}}\right) - k_{mX}\left(c_{mX} - \frac{c_{oX}}{Ke_2}\right) \\ r_{oX} &= k_{mX}\left(c_{mX} - \frac{c_{oX}}{K_{e2}}\right) \end{aligned} \tag{3.4}$$

It now remains to model diffusion effects on the catalytic properties of the zeolite film.

3.3.2 Model equations

Reactor mass balance

A reactor mass balance yields:

$$\frac{dF_i}{dV_{zeolite}} = r_{i,ave} \tag{3.5}$$

Assuming a constant density system at constant pressure and no change in the number of moles implies $F_i = Qc_i$, which, after manipulation and substitution into equation 3.5 yields equation 3.6:

$$\frac{dc_{zi}}{d\tau} = r_{i,ave} \tag{3.6}$$

where

$$\tau = \frac{V_{zeolite}}{Q} \tag{3.7}$$

$r_{i,ave}$ can be obtained from a mass balance across the zeolite film. c_{zi} and $c_i(z,\tau)$ are only equal at the boundary.

Zeolite film mass balance

Considering the molar flux $W_i = -D_i \frac{\partial c_i(\tau,x)}{\partial x}$ ($\frac{mol}{L^3.T}$), equation 3.8 represents a material balance of species i diffusing through an area A_z across the differential element (figure 3.2) at any residence time (*i.e.*, position) τ in the bed and thus the concentrations are both a function of x and τ.

$$W_i \cdot A_z|_x - W_i \cdot A_z|_{x+\Delta x} + r_i \cdot A_z \cdot \Delta x = 0 \tag{3.8}$$

where r_i ($\frac{mol}{L^3.T}$) is a volume-based reaction rate. Division by $A_z \Delta x$, substitution of W_i and defining dimensionless variables $y_i = \frac{c_i}{c_o}$ and $\zeta = \frac{x}{T_f}$ yields the dimensionless 2nd order partial differential equation 3.9 for the zeolite film at any position z in the reactor as Δx tends to 0.

$$\frac{\partial^2 y_i(\tau,\zeta)}{\partial \zeta^2} + \frac{T_f^2}{D_i c_o} r_i(\tau,\zeta) = 0 \tag{3.9}$$

c_o is the total xylene feed concentration. y_i is thus a gas phase mole fraction on the external surface. The solution of this equation requires 2 boundary conditions.

At the support surface ($\zeta = 0$), there is no diffusion into the support, therefore the first boundary condition is given by equation 3.10.

$$\left.\frac{\partial y_i}{\partial \zeta}\right|_{\tau,0} = 0 \tag{3.10}$$

At the gas film interface ($\zeta = 1$), assuming gas film resistance is negligible (see appendix A.2), the concentration in the bulk gas and at the surface must be equal, thus equation 3.11. c_{zi} and $c_i(z,\tau)$ are only equal at the boundary.

$$y_i(\tau,1)c_o = c_{zi}(\tau) \tag{3.11}$$

The average reaction rate across the zeolite film ($r_{i,ave}$) at any τ can now be evaluated (equation 3.12).

$$r_{i,ave} = \frac{\int_0^V r_i dV}{\int_0^V dV} = \int_0^{T_f} r_i A_z dx = \frac{\int_0^1 r_i d\zeta A_z T_f}{A_z T_f} \tag{3.12}$$

To obtain the second boundary condition requires the manipulation of the reactor and zeolite film mass balances.

Combining the reactor and zeolite film mass balance

Equation 3.12 can be evaluated by using equation 3.9 to yield equation 3.13

$$r_{i,ave} = \frac{D_i c_o}{T_f^2} \cdot \left.\frac{\partial y_i}{\partial \zeta}\right|_{\tau,1} \tag{3.13}$$

The effectiveness factor (η_i) is thus given by equation 3.14.

$$\eta_i = \frac{\int_0^V r_i dV}{r_{is} A_z T_f} = \frac{D_i c_o}{T_f^2 r_{is}} \left.\frac{\partial y_i}{\partial \zeta}\right|_{\tau,1} \tag{3.14}$$

Substitution of equation 3.7 and using equation 3.11 yields the second boundary equation (equation 3.15).

$$\frac{\partial y_i(\tau,1)}{\partial \tau} = \frac{D_i}{T_f^2} \left.\frac{\partial y_i}{\partial \zeta}\right|_{\tau,1} \tag{3.15}$$

The equations 3.9, 3.10, and 3.15 represent the final model equations.

3.3.3 Solution of model equations

An orthogonal collocation technique [Villadsen and Michelsen, 1978] is employed to discretize equation 3.9 into a set of algebraic equations (equation 3.16),

$$\sum_{j=1}^{N+1} B_{ij} y_{kj} + \frac{r_k(\tau,\zeta_i)}{c_o} \frac{T_f^2}{D_k} = 0 \qquad k = 1,2,3 \qquad i = 1...N \tag{3.16}$$

where ζ_i are the coordinate nodes defined by the collocation procedure, B_{ij} is the collocation coefficient matrix representing the 2nd derivative, N the number of internal collocation points, and $k = 1,2,3$ represents the pX, mX, and oX species, respectively.

Using a symmetry transform, the support boundary condition (equation 3.10) is automatically satisfied. The 2nd boundary condition (equation 3.15) is also discretized to yield an ordinary differential equation (equation 3.17),

$$\frac{dy_{ki}}{d\tau} = \frac{D_k}{T_f^2} \cdot \sum_{j=1}^{N+1} A_{N+1,j} y_{kj} \tag{3.17}$$

where A_{ij} is the collocation coefficient matrix representing the 1st derivative.

Equations 3.16 and 3.17 are repeated for each species $k = 1...3$. They represent a set of differential-algebraic equations (DAE) which are solved using the implicit integrator DDASAC [Stewart and Caracotsios, 1996]. Sufficient accuracy of the step gradients was obtained with $N = 30$ [Rice and Do, 1995; Schwan and Möller, 2003].

3.3.4 Estimation of model parameters from experimental data

To enable the extraction of the model parameters, further assumptions had to be made. Following the findings by Mirth et al. [1993] and Wei [1982], it was assumed that $D_{pX} : D_{oX} : D_{mX} = 1 : 100 : 1000$ and $k_{pX} = 2k_{mX}$. The result was a 2-parameter model, with k_{pX} being the one and $\frac{D_{pX}}{T_f^2}$ the other. A Levenberg-Marquardt routine [Burton et al., 1980] was then employed to evaluate these parameters, with the least squares criterion defined by equation 3.18.

$$Error = \sum_{j}^{N_{species}} \sum_{i=1}^{N_{exp}} \left[y_{exp(i,j)} - y_{model(i,j)} \right]^2 \tag{3.18}$$

3.3.5 Typical response curves as a function of film thickness

The effects of diffusion resistance or film thickness on the catalytic properties of the films were simulated by taking $k_{pX} = 6.7$ and varying the diffusion time constant by six orders of magnitude and plotting the corresponding response curves. Figure 3.4 shows decreasing the diffusion time constant (larger diffusion limitations) decreases the conversion and makes the catalyst less active, as expected. More interestingly, figure 3.5 shows that the mX yields decrease and oX yields increase with decreasing diffusion time constant or increasing diffusion resistance. Under strong

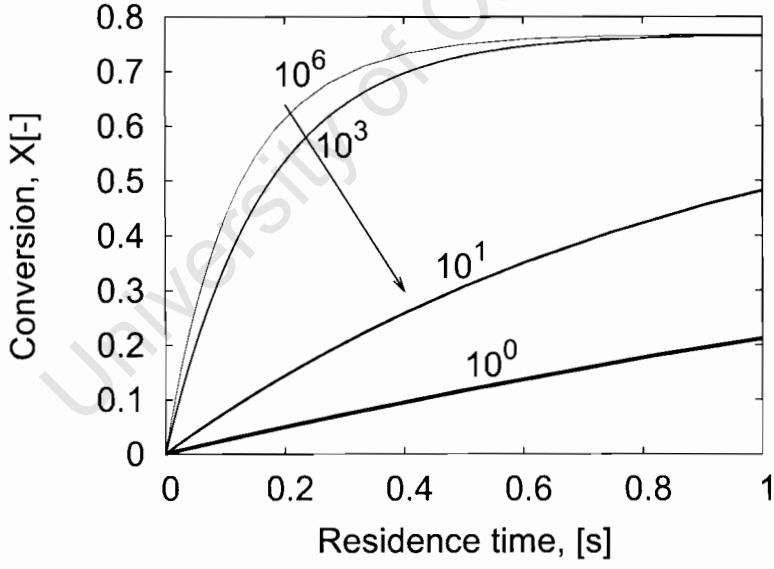

Figure 3.4: Typical pX conversion variation with residence time. Thickness of lines represents severity of diffusion resistance or film thickness, which increases in the direction of the arrow. Above/below each curve is the diffusion time constant (D/T_f^2, [s^{-1}]). $k_{pX} = 6.7 s^{-1}$.

diffusion limitations (bold lines) both mX and oX appear as primary products with oX being preferentially produced. This signifies an apparent change of mechanism from the series reaction $pX \leftrightarrow mX \leftrightarrow oX$ to a parallel reaction $pX \leftrightarrow mX$, $pX \leftrightarrow oX$. This discrepancy is a result of the diffusion resistance imposed by the zeolite on mX and oX.

Furthermore, the response for $D/T_f^2 = 10^3$ shows a small decrease in the conversion but a

large shift in the yield curves, indicating that the yield data is considerably more sensitive to diffusion limitations than the conversion plots for the typical model parameters used for xylene isomerization. The conversion, or catalyst activity continues to decrease with increasing diffusion limitations. This is in contrast to the yield response which varies between two boundaries. Typically, for all $D/T_f^2 > 10^4$ the yield of mX and oX remains unchanged, and represents the intrinsic selectivity of the catalyst. On the other hand, at $D/T_f^2 < 10^2$ the yield of mX reaches a minimum while that of oX reaches a maximum.

Further decreasing D/T_f^2 will not change the observed yield (or selectivity) at constant X, although the conversion (or activity) of the catalyst continues to decrease. This is very important information for parameter estimation. It indicates that for this particular value of k_{pX}, diffusion limitations strongly impact on the yield of mX and oX for diffusion time constants in the range $10^2 < D/T_f^2 < 10^4$, or about 2 orders of magnitude, in which diffusivity estimation would be most sensitive. Outside the bounds of these limitations it becomes increasingly difficult to estimate accurate diffusion coefficients. Outside the range $10^2 < D/T_f^2 < 10^4$ it is no longer possible to estimate diffusion coefficients from the experimental data.

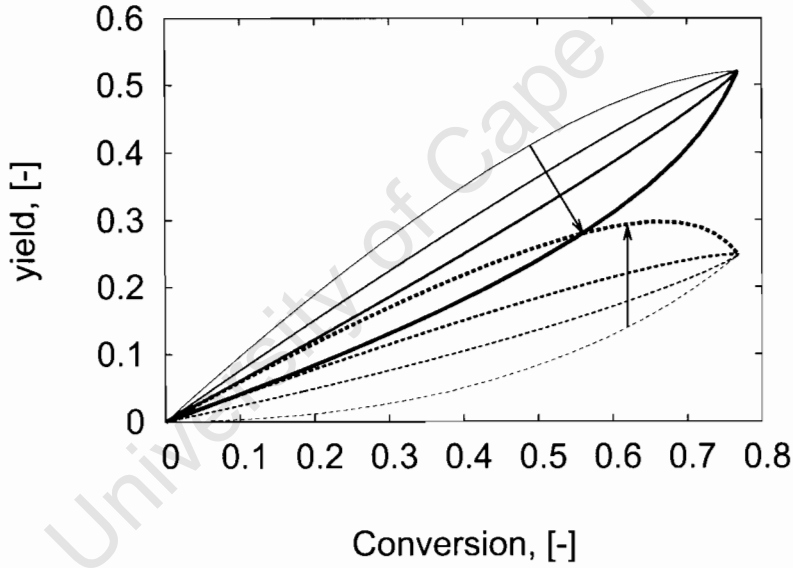

Figure 3.5: Typical mX and oX yield variation with pX conversion. The broken lines represent oX yields, and the solid ones mX yields. Thickness of lines represents severity of diffusion resistance or film thickness. Arrows show movement of the yields as diffusion resistance (or film thickness) increases. In increasing order of the thickness of the lines, the diffusion time constants (D/T_f^2, [s^{-1}]) are 10^4, 3×10^3, 1×10^3, and 10^2. $k_{pX} = 6.7 s^{-1}$.

Figure 3.6 shows that the yield of mX is highest at low conversion when there are no diffusion limitations. Interestingly, under very strong diffusion limitations (small D/T_f^2) it is possible for the mX:oX ratio to exceed that predicted by equilibrium over a wide range of conversions, of course at the expense of very low reactivities. These results may be explained by the following physical reasoning. As resistance to diffusion increases, the slow diffusing mX isomer accumulates in the ZSM-5 pore matrix, thus driving further isomerization into the faster diffusing oX. Thus the decreasing mX:oX ratio with increasing diffusion resistance. These simulations show that to

maximize the effect of diffusion on the yield, operating at low conversions would be ideal. At high conversions, the curves converge towards the chemical equilibrium line, thereby masking the effects of diffusion resistance.

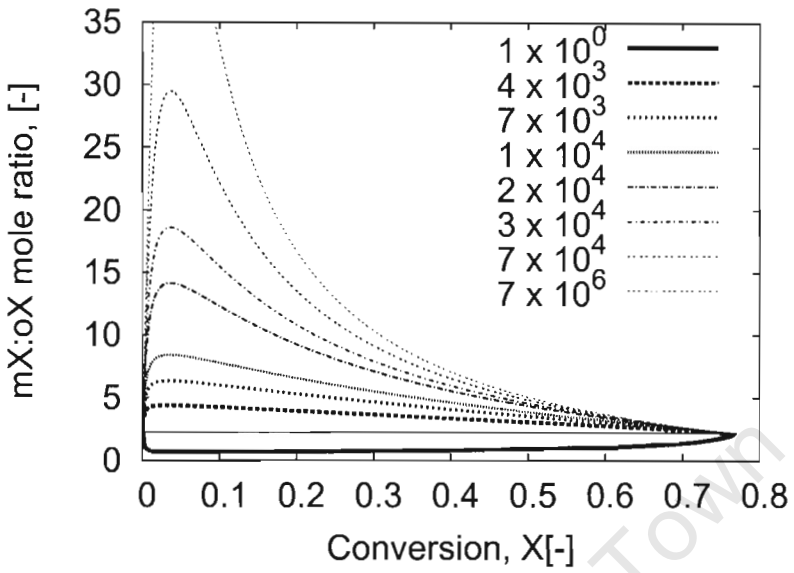

Figure 3.6: Typical mX:oX dependencies on pX conversion. Legend shows diffusion time constants (D/T_f^2, [s^{-1}]). $k_{pX} = 6.7s^{-1}$. The thin solid line represents equilibrium.

Figure 3.7 shows that the effectiveness factor for oX (equation 3.14) is much greater than 1, and increases with increasing diffusion resistance. The effectiveness factor approaches unity at negligible diffusion limitations and near equilibrium as expected. These observations can be explained with the following arguments.

At low conversions, the reaction rate is highest, thus mX is formed at a high rate. Since it cannot escape with as much ease as the other isomers, its concentration rises within the film, being highest at the support film interface. By the LeChatelier principle, it must therefore convert to oX. Because on the outside surface the mX concentration is very low, the rate of formation of oX is also very low, thus

$$\eta_{oX} = \frac{r_{oX}(average)}{r_{oX}(on\ the\ surface)} >> 1 \tag{3.19}$$

η_{oX} should be highest at low pX conversion, where the rate of formation of mX is the greatest, as observed. At higher conversions, some mX will escape to the surface and the reaction of oX on the surface will slow down. Hence η_{oX} decreases with increasing pX conversion.

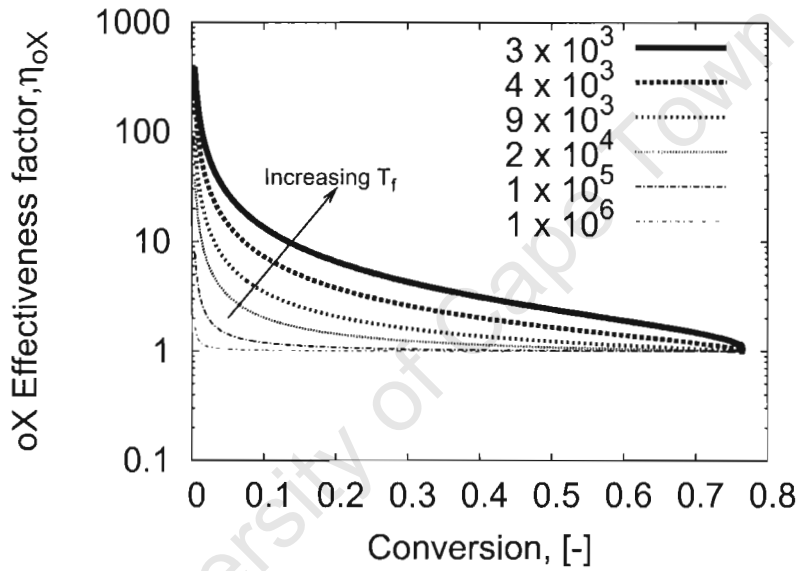

Figure 3.7: Typical oX effectiveness factor as a function of pX conversion. Thickness of lines represents severity of diffusion resistance or film thickness. Arrow shows movement of η_{oX} as diffusion resistance (or film thickness) increases. Legend shows diffusion time constants (D/T_f^2, [s^{-1}]). $k_{pX} = 6.7 s^{-1}$.

Chapter 4

Results

For tabular data, a code is used to identify the film, such that Q150 denotes the 150 nm quartz-supported film, A800 the 800 nm alumina-supported film, and so on. In other words, the first letter denotes the support (Q = quartz, A = alumina, and S = sand), and the accompanying 3-digit number the film thickness in nm. Unless otherwise stated, 'catalyst' refers to the support and the zeolite film coating it.

4.1 Film synthesis and physical characterization

4.1.1 Zeolite loading

Total BET surface areas for each film are shown in table 4.1.

Table 4.1: BET surface areas measured after film synthesis.

	BET surface area data[a] m^2/g		
Step[b] #	Quartz	Sand	Alumina
0	0.0036	0.174	0.125
1	0.125	3.04	1.04
2	0.249	4.57	2.86
6	0.664	12.0	5.64
18	2.45	31.4	8.30

[a]BET surface area ($\frac{m^2}{g\ catalyst}$) of ZSM-5 synthesised using the same synthesis mixture and procedure is 415 m^2/g.

[b]Number of hydrothermal synthesis to achieve film.

It has been shown by Hedlund [1998] that the zeolite loading on the support may be estimated from the difference between the BET surface area of the unsupported and supported zeolite. The BET surface area of the support is negligible (see table 4.1) and thus does not contribute to the total BET surface area. The change in surface area with hydrothermal synthesis shown in table 4.1 is therefore due to increase in mass of zeolite loaded onto the support. In this calculation it is assumed that the morphology of the zeolite in both cases is the same because the same synthesis

procedure has been used. This procedure has been verified by Hedlund [1998] to provide excellent estimates of zeolite loading. This method has been used to estimate the loading on the different supports as shown in figures 4.1 and 4.2.

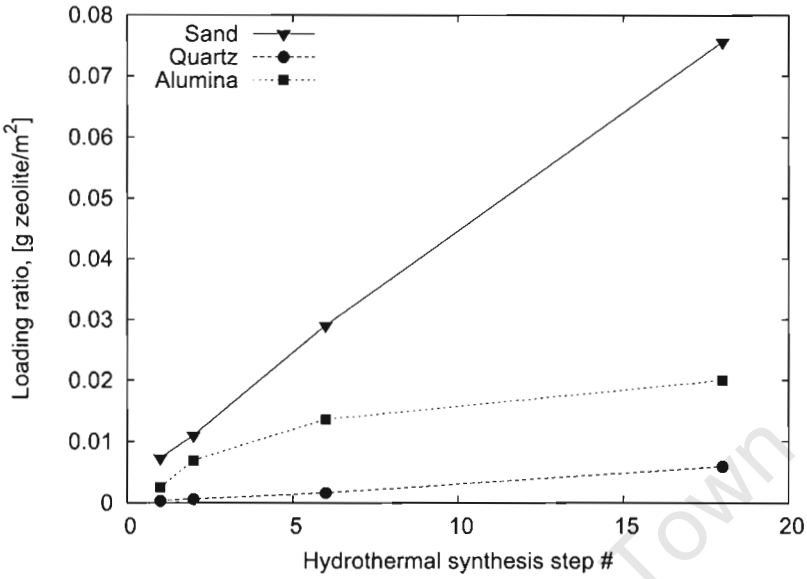

Figure 4.1: ZSM-5 loading on different supports (based on total catalyst mass).

Figure 4.1 shows that the amount of zeolite loaded is highest on the sand samples and lowest on the quartz. This is in proportion to the BET surface area observed for the supports as shown in table 4.1. The rate of zeolite loading (*i.e.*, the slope of the plot) onto the alumina support decreases with increased zeolite loading. This is in contrast to the other supports, where it remained constant with increasing number of hydrothermal synthesis. The initial rate of zeolite loading on the alumina support is higher than the quartz support and similar to the rate of loading of the sand supports, while at high zeolite loadings the rate of zeolite loading is similar to that on the quartz supports and lower than that on the sand supports.

The growth rate can be normalized with respect to the theoretical support surface area (A_{theory}) using equation 4.1,

$$A_{theory} = 4\pi \left(\frac{d_p}{2}\right)^2 \tag{4.1}$$

where d_p is the equivalent average particle diameter.

Figure 4.2 shows that both non-porous supports have the same zeolite loading on an area basis, whilst that of alumina has a significantly higher loading. Thus adequate account is taken of the differing particle size of the non-porous supports with this approach. The higher loading of the alumina is due to the zeolite being deposited in the pores and thus not accounted for by the theoretical surface area.

The secondary y-axis in figure 4.1 shows film thickness as a function of the number of hydrothermal synthesis steps. As previously observed [Sterte et al., 2001; Wang et al., 2002], the rate of growth of the film thickness is independent of support type and morphology. Table 4.2 shows

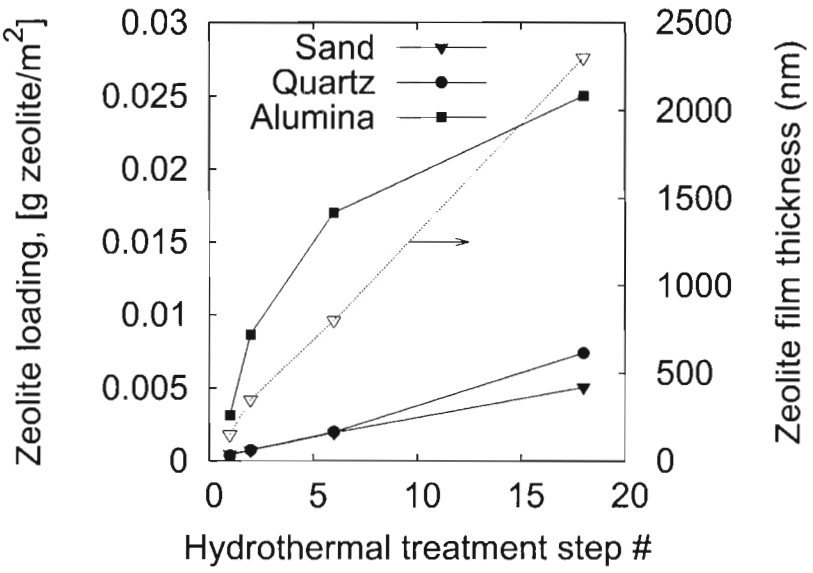

Figure 4.2: ZSM-5 loading on different supports (based on the theoretical external surface area of a smooth uniform-sized sphere, given by equation 4.1).

the apparent external surface areas calculated from the loading data assuming a smooth film of uniform thickness T_f.

Table 4.2: Apparent external surface area of ZSM-5 films on sand, alumina, and quartz supports.

Film thickness (T_f) nm	Theoretical external surface area (A_z[a]) m^2/g zeolite
150	3.8
350	1.6
800	0.71
2300	0.25

[a]Defined in equation 4.2.

Other definitions of area could be used (*e.g.* BET surface area given in table 4.1), but these will only cause a downward shift in the curve (relative to quartz it is about 3 times lower for sand and 23 times lower for alumina).

The BET surface area is higher than the theoretical surface area (equation 4.1), thus accounting for microscopic surface roughness and porosity in the case of alumina. This cannot explain the changing growth rate with zeolite loading observed on the alumina. However, this does indicate that on a BET surface area basis, the growth rate on the alumina is slower than on quartz and sand.

4.1.2 Film thickness and surface area

The film thickness (T_f) shown in table 4.2 is determined independently using SEM analysis. It increases linearly with the number of hydrothermal synthesis and is independent of the support

type. Hedlund [1998] has shown that this technique provides an accurate measure of the film thickness. SEM is a local technique and thus may not represent the particle as a whole. Using the loading (m_z) from figure 4.1 and assuming a *smooth uniform flat* zeolite film (*i.e.*, like a carpet covering the floor) the apparent external surface area (A_z) can be estimated from the volume average area (equation 4.2). The assumption of flat plate geometry was justified in §3.1.

$$A_z = \frac{m_z}{\rho_z T_f} \qquad [m^2/g_{zeolite}] \tag{4.2}$$

Figure 4.3 shows the apparent surface area of the supports on a total catalyst mass basis, *i.e.*, A_z is corrected to a per mass of catalyst basis from a per zeolite mass basis. This was done to enable comparison between BET and theoretical surface areas which are also based on a total catalyst mass.

If the zeolite film were to grow perfectly smoothly over the BET surface area and because the zeolite does not contribute significantly to the mass of catalyst, the external surface area of the film on a catalyst mass ratio should be similar to the BET surface area of the support irrespective of zeolite loading.

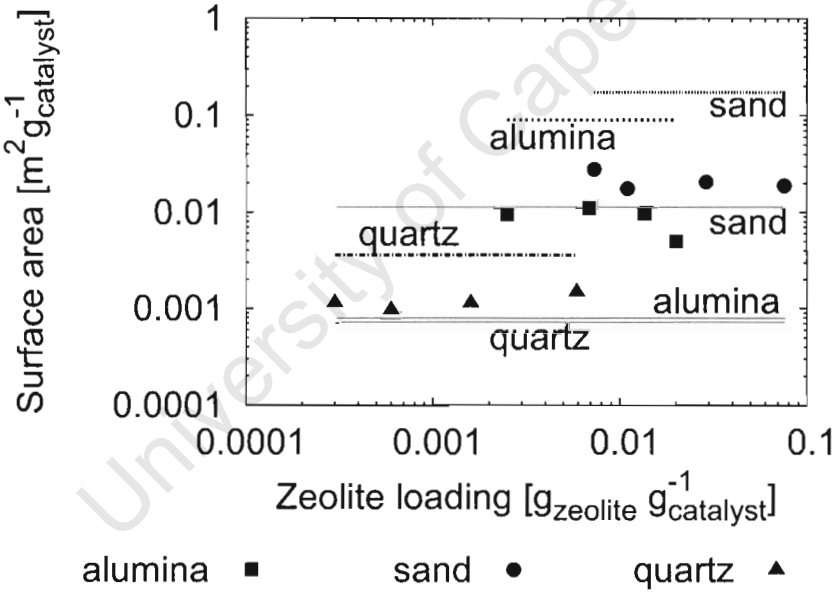

Figure 4.3: Apparent surface area of supported zeolites based on the total catalyst mass (points : support + zeolite, dashed lines : BET area of support, lines : theoretical non-porous area given by equation 4.1).

For the zeolite supported on alumina and sand the surface area was about an order of magnitude lower than the BET surface area of the support alone, while for the quartz it was about a factor of 4 lower. These results show that the BET surface area, which includes all micro and meso pores, is not suitable for describing the surface area over which film growth takes place.

As an alternative, if it could be assumed that the zeolite is uniformly distributed over the BET surface area, the film thickness T_f would be an order of magnitude smaller for the alumina and

sand supported zeolite. The alumina support has pore sizes of the order of 200 nm which would have to be filled by the zeolite film before an uniform film can be obtained. The seeds (60 nm in size) can also concentrate in these 200 nm pores creating sites for preferential growth. For the sand supported zeolite, the surface area estimated from SEM and zeolite loading is close to the non-porous external surface area. Most of the BET surface area of the sand arises due to small micropores not accessible to the seeds and thus zeolite growth occurs only on the external surface of the particles. This shows that the quartz and sand supported zeolite films maybe approximated as uniform, smooth films. The alumina supported zeolite cannot be assumed as a film with a uniform thickness which has been assumed by the SEM film thickness calculation and the estimation of A_z is a poor approximation of the external surface area. However, as no further analysis has been able to shed more light on the characteristics the external area of the alumina supported zeolites, the calculated surface area (A_z) will be assumed representative of the external surface area of all the supported zeolite catalysts.

4.1.3 SEM characterization

The support and zeolite film textures were also analyzed by SEM. Figure 4.4 shows that the alumina support is rough and tortuous when compared to sand and quartz. It is this roughness which contributes to the increased loading observed on the alumina supports in contrast to the quartz supports. Figure 4.5 shows that even with a 800 nm film thickness, the alumina films retain their surface roughness and have larger "crystals" than the sand and quartz supported zeolite which have smooth surfaces. At higher loadings the zeolite film smoothens out the alumina surface roughness by filling up the pores. Figure 4.6 shows that the zeolite film supported on alumina (a) has a considerably more tortuous surface when compared to the zeolite supported on quartz (b). However, although the alumina surface is rough, the film still adheres to the contours of the alumina particles and is thus still approximated as a flat plate except with considerably more surface area per gram catalyst as a result of the higher loading. These SEM results support the observations obtained from the loading and surface area interpretations.

During the hydrothermal preparation of samples S800 and S2300, it was observed that the resulting catalyst samples had grown together into clusters. An example of such a catalyst cluster is shown in figure 4.7. It was necessary to physically dislodge these clusters at the end of the sample preparation. This process could lead to less uniform films due to cracking and fragmentation of the zeolite layers. These clusters might also prevent access of the synthesis nutrients to the core of the cluster, leading to non-uniform film thicknesses. No attempt was made to further characterize these samples by SEM.

4.1.4 Ion exchange

To confirm that the Na^+ ion were exchanged with NH_4NO_3, an Energy Dispersive X-ray (EDX) analysis was carried out. Figure 4.8 shows that the NaKα peak at $\approx$1 keV for the Na^+ ions

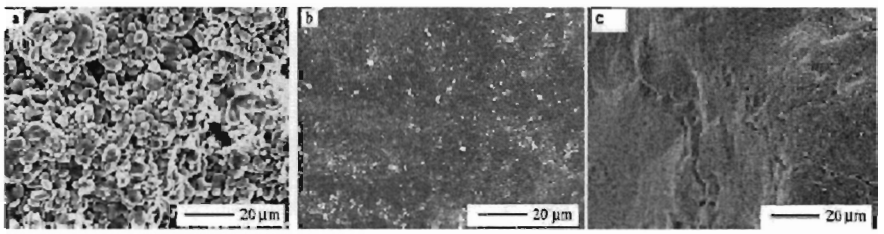

Figure 4.4: SEM images of supports. (**a**) Alumina; (**b**) Quartz; (**c**) Sand.

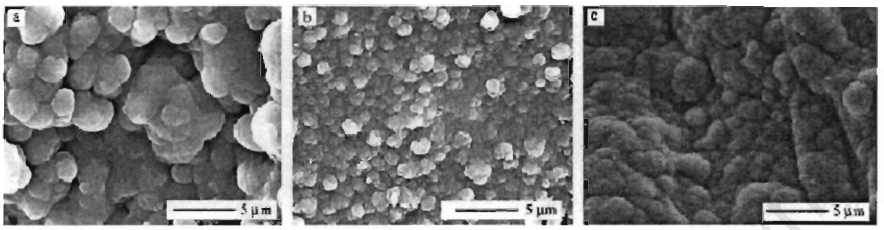

Figure 4.5: SEM image of six-step ZSM-5 films. (**a**) A800; (**b**) Q800; (**c**) S800.

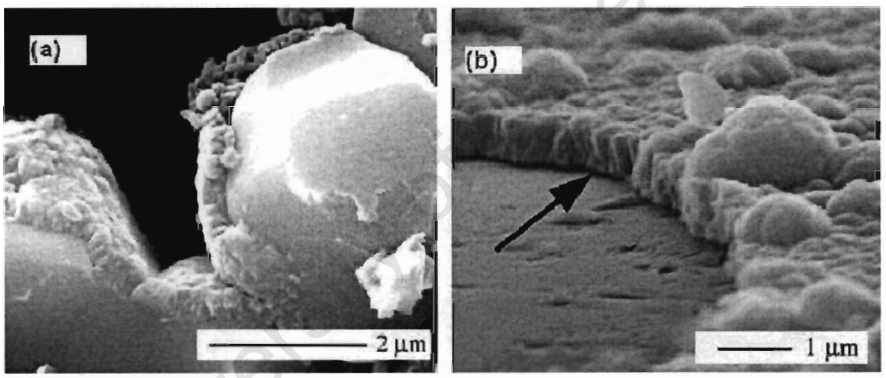

Figure 4.6: SEM side view images of (**a**) A350; (**b**) Q800.

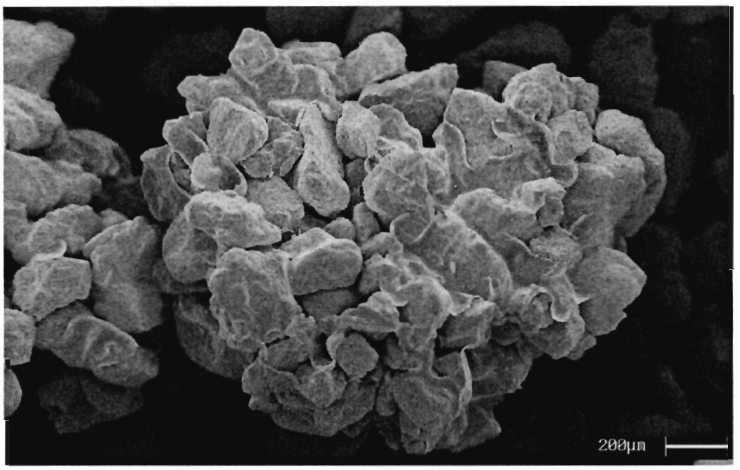

Figure 4.7: SEM image of lumps characteristic of samples S800 and S2300.

disappears after ion exchange for sample Q2300. It was thus concluded that the ion exchange procedure was adequate.

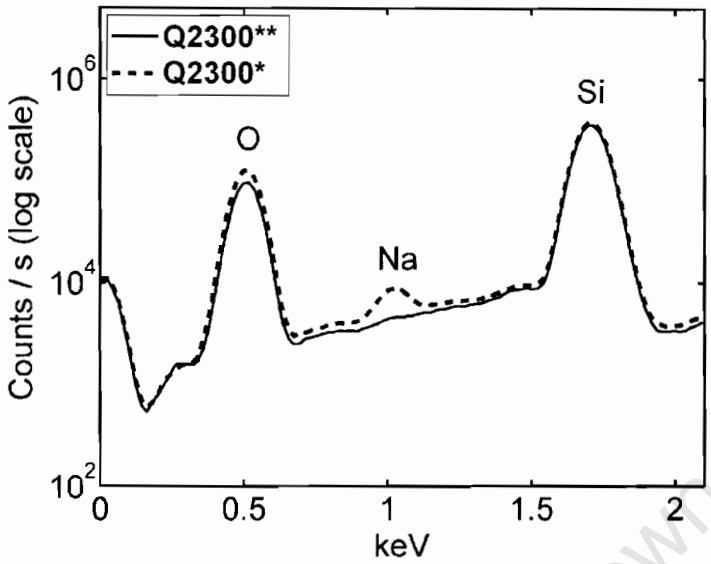

Figure 4.8: EDX profile of sample Q2300 prior to (*) and after (**) ion-exchange with NH_4NO_3.

4.1.5 Surface composition of the zeolite supported on alumina

When the alumina-supported zeolite is calcined, migration of the aluminium (Al^{3+}) and other cation impurities (notably Na^+ ions) from the support to the zeolite film is possible. The chemical composition of the zeolite film was analyzed using X-ray Photofluorecent Spectroscopy (XPS). This is a surface technique and should better reflect the properties of the zeolite film than using bulk analysis such as Atomic Absorption (AA), which would also measure trace impurities in the support, thereby masking any contribution that the zeolite might make to the bulk composition.

Table 4.3 shows that both aluminum (Al^{3+}) and sodium (Na^+) ion migration has occurred into the zeolite film. The aluminum content exceeds the amount added into the original synthesis solution which means that either Al^{3+} was preferentially incorporated and/or the alumina from the support was being incorporated into the zeolite. A silicon and aluminum mass balance was not carried out on the film synthesis as there were multiple steps for each. The Na^+ content was always less than the Al^{3+}, indicating that not all of the acid sites (H^+) were neutralized on or near the external surface. The migration of the Al^{3+} and Na^+ ions is more severe for the

Table 4.3: The surface composition of the zeolite films supported on alumina measured by XPS (synthesis Si/Al = 50).

	A150	A350	A800*	A800	A2300
Si/Al	8	13	19	18	27
Si/Na	18	30	112	24	35
Si/H	14	23	-	72	118
Si/N	∞	∞	22	∞	∞

*This sample was only ion-exchanged, not calcined.

thinnest films. In the A800* sample, the Al^{3+} content, to within experimental error (equation 4.3) matches the counter ion concentration of Na^+ and NH_4^+, as is expected for as synthesized samples.

$$\left(\frac{Si}{Al}\right) = \left(\frac{Na}{Si} + \frac{N}{Si}\right)^{-1} \tag{4.3}$$

A comparison of samples A800* and A800 shows that after calcination only the Na^+ ion content increased significantly. This indicates that most of the Al^{3+} incorporation occurs during synthesis while most of the Na^+ migration occurs during calcination.

Considering the Na^+ migration to be a diffusion driven process (concentration gradient), the Na/Al ratio of the thick films show that proportionately there was a greater exchange of H^+ ions when compared to thin films. This is not expected for a diffusion controlled process occurring over a fixed time interval but over varying path lengths (film thickness). However, the absolute quantity of Na^+ ions (given by Na/Si) decreases with increasing film thickness as expected. These results suggest that in the thin films additional Na is being measured which does not have ion exchange capacity. The remaining acid site concentration on the external surface can be estimated by equation 4.3.

Results in table 4.3 indicate that the remaining acid site concentration decreases with increasing film thickness. It is thus expected that the thin films are more catalytically active than the thick films. However, as observed by other workers [Hedlund et al., 1999a], it might be possible that thin films do not completely cover the alumina support and hence the XPS technique would measure bulk Al^{3+} ions from the support and thus overestimate the Al^{3+} content of the zeolite surface. It is also possible that a portion of the Na^+ appears as NaO_2 as opposed to ion migration, which indicates that the support is influencing the resuts.

It has not been possible to obtain a clear understanding of the interaction of the zeolite with the alumina surface during synthesis, the analysis being complicated by the presence of a large quantity of support material which would dominate any specific analysis of the zeolite film.

4.2 Reaction characterization

4.2.1 Activity of the supports

The supports were packed in the reactor and tested for activity under the same reaction conditions of pX isomerization and TIPB cracking as the supported zeolite catalysts. In all cases the conversion over the support was one to two orders of magnitude lower than the zeolite supported catalysts. It was thus assumed that the contribution of the support to the observed reactivity could be neglected in all cases.

4.2.2 Carbon balances

Figure 4.9 shows that the carbon balances for both TIPB and pX reactions are better than 80% within a standard deviation of 5%. The data indicate that the mass balance error on the TIPB conversion exceeds that of the pX conversion. The scatter in the mass balance data shows no systematic error. Except for the outliers indicated, the mass balances were accepted to be sufficiently accurate for the interpretation of the reaction data.

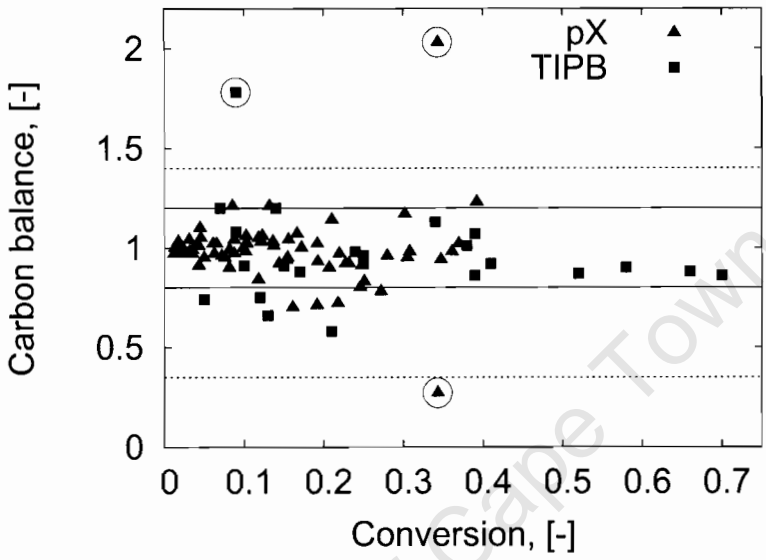

Figure 4.9: Carbon balances as a function of conversion. The solid and broken lines are bounds beyond which lie moderate outliers of the pX and TIPB data, respectively. The ringed data points are extreme outliers.

4.2.3 TIPB cracking over zeolite films

Table 4.4 and figure 4.10 show the rate constants evaluated from the reaction data based on the apparent external surface area which was shown (§4.1.2) to be representative of the surface properties of these films. Catalyst Q150 was inactive to TIPB cracking. General trends observed from figures 4.11 and 4.12 show that the zeolite supported on the alumina has the lowest external surface activity while the quartz has the highest external surface activity. The alumina supported zeolite showed a decrease in activity with decreasing film thickness while the trend with the other supports was not clear. The lines indicate that the first order model approximates the reaction data well.

The rate constant data confirm that the quartz and sand supported zeolites are more active than the alumina supported zeolite. Except for the alumina supported zeolite, in which Na^+ migration has altered the external surface properties, all the remaining film catalysts are expected to have the same rate constant on an external surface area basis. With the inclusion of A2300, the TIPB rate constants are all of the same order of magnitude which suggests that, with a few exceptions within the approximates made in the surface area, the external surface activity of all sand and

Table 4.4: TIPB rate constants estimated from the experimental data.

T_f nm	$k \times 10^6 \pm \sigma\%$ m/s		
	Sand	Quartz	Alumina
150	7.60±2.89	-	0.417±3.34
350	19.5±5.20	15.2±22.8	1.01±2.42
800	3.69±7.77	4.52±0.763	1.47±3.67
2300	8.52±1.71	17.3±2.91	10.4±18.1

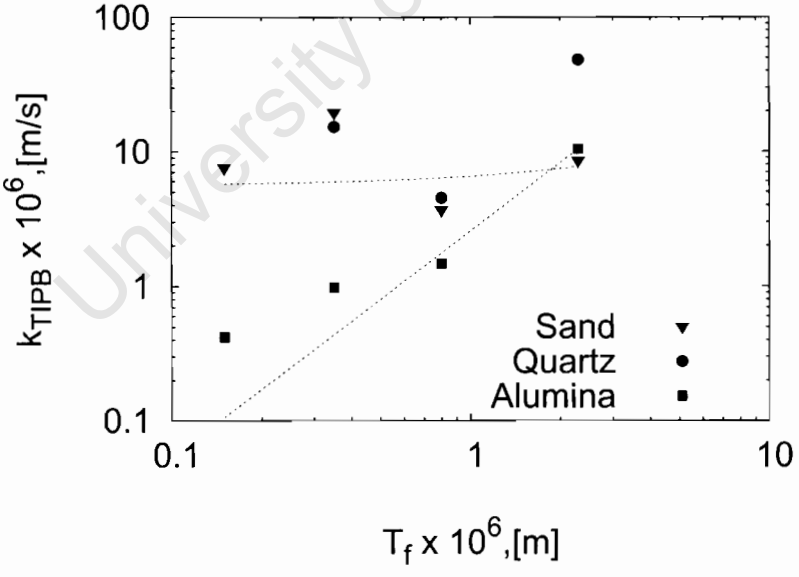

Figure 4.10: TIPB rate constants as a function of film thickness. Symbols - experimental data; dashed lines - trendlines. The 150nm quartz supported zeolite film was inactive.

quartz supported catalysts are similar.

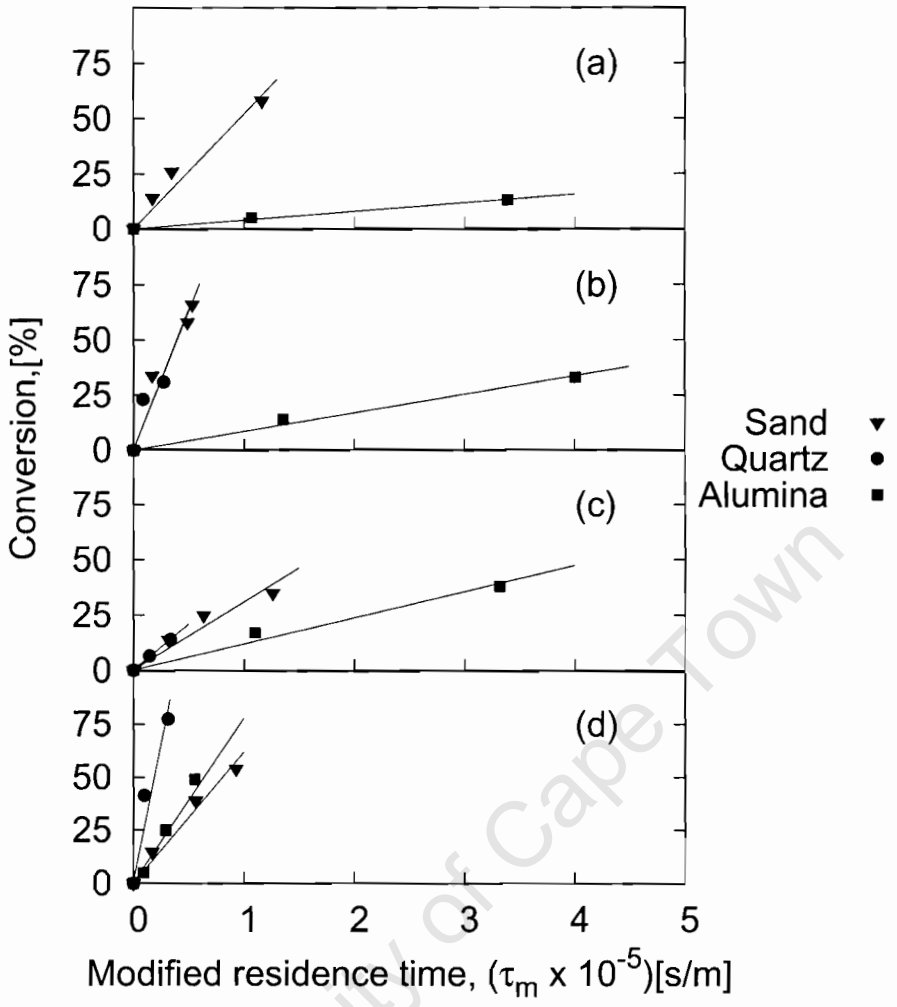

Figure 4.11: TIPB conversion as a function of modified residence time for zeolite ZSM-5 films on different supports. Symbols - experimental data; solid lines - model prediction. (a) 150 nm, (b) 350 nm, (c) 800 nm, (d) 2300 nm. The 150nm quartz supported zeolite film was inactive.

4.2.4 pX isomerization over zeolite films

Figure 4.13 shows that sand and quartz supported zeolite catalysts have similar conversions at the same residence time. The alumina supported zeolite catalyst is much less reactive than the other catalysts as observed by the lower conversions. This trend is consistent across all film thicknesses.

Figure 4.14 shows that the yields of mX and oX follow the correct trend for sequential reactions and are not strongly influenced by the film thickness. The sand supported zeolite catalysts, which have the most significant variation in yield with film thickness, show an increase in the yield of oX and a decrease in the yield of mX with increasing film thickness. The variation in the yields for the sand supported zeolites falls into two groups. The S800 and S2300 have a high oX yield while the S150 and S350 have the lower oX yield, which seems to suggest that these might have similar diffusion properties.

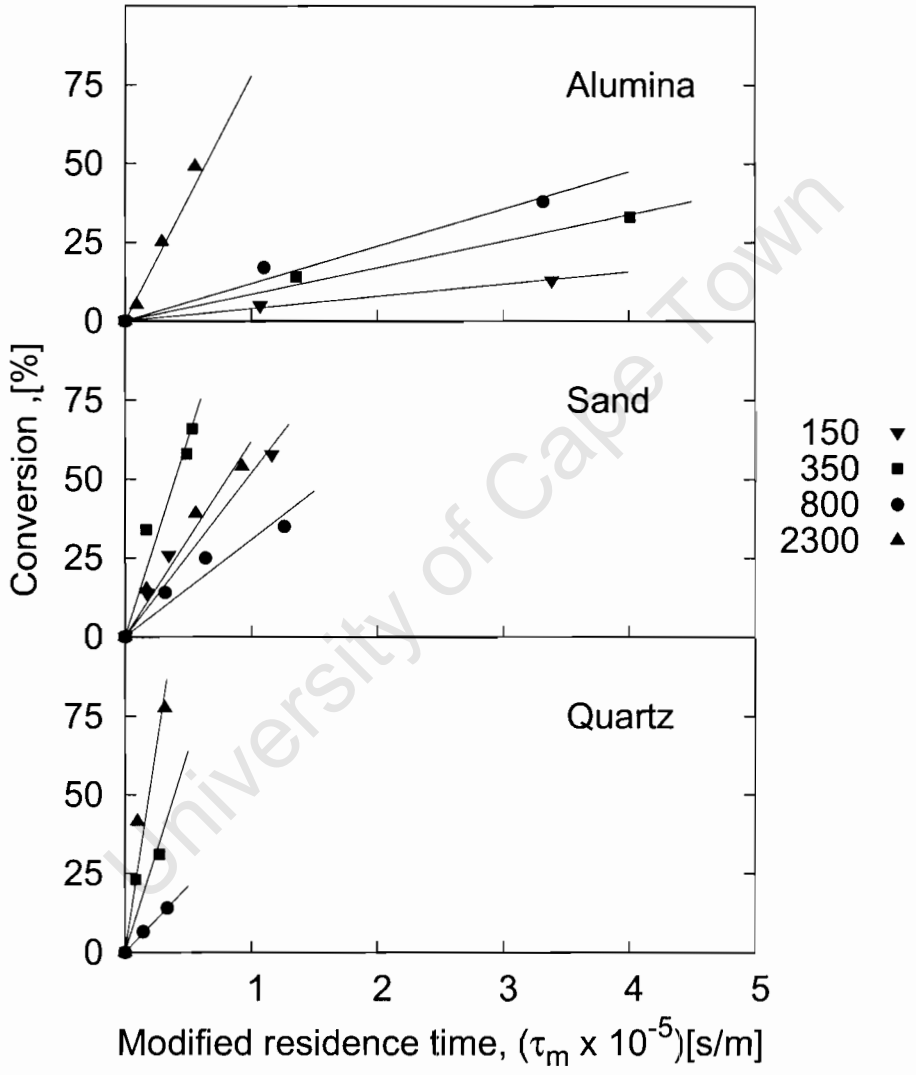

Figure 4.12: TIPB conversion as a function of modified residence time for zeolite ZSM-5 per support. Legend indicates film thickness (nm). Symbols - experimental data; solid lines - model prediction. The 150nm quartz supported zeolite film was inactive.

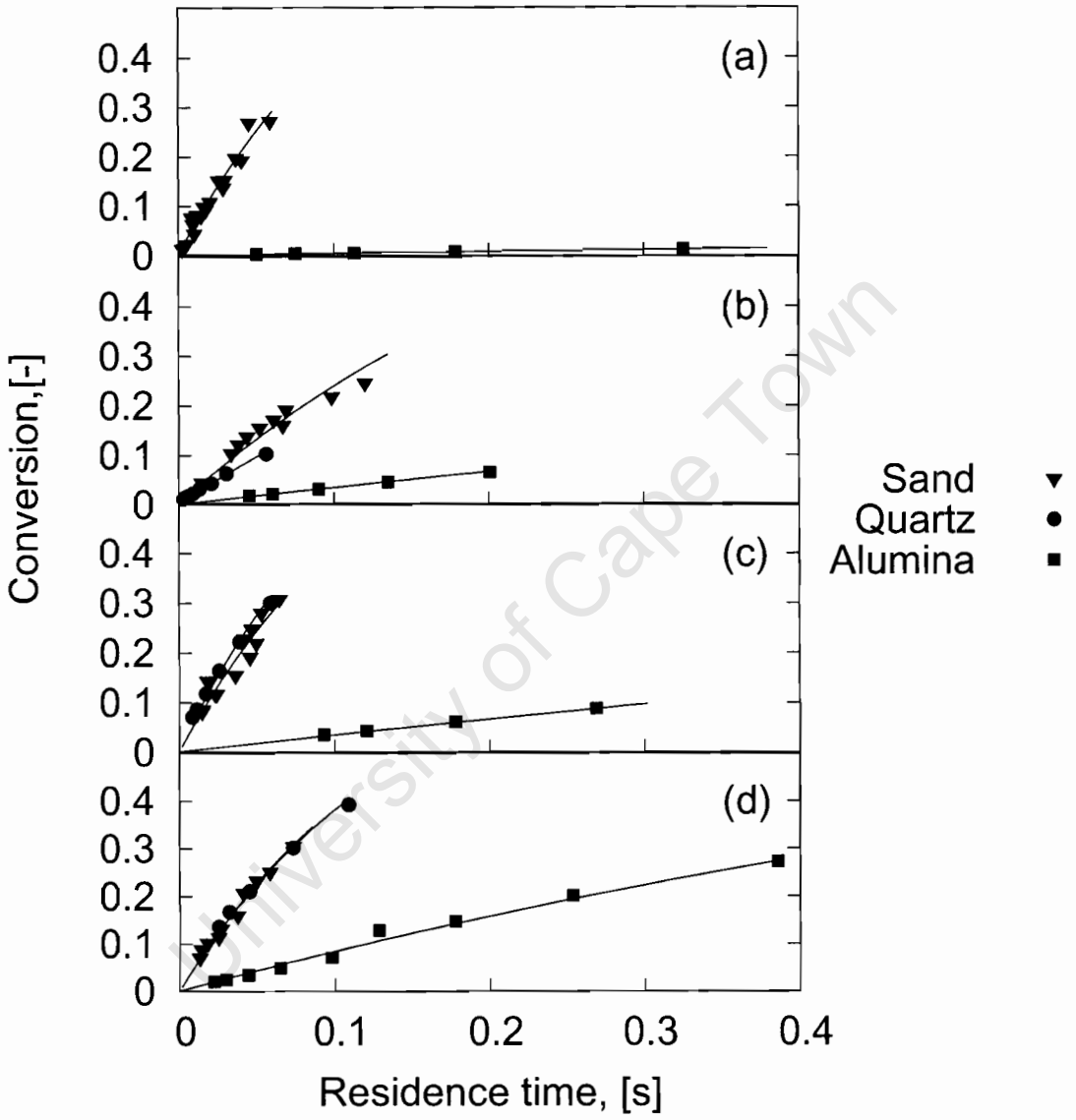

Figure 4.13: The variation of pX conversion with residence time. Symbols - experimental data; solid lines - model predictions; (a) 150 nm, (b) 350 nm, (c) 800 nm, (d) 2300 nm. The 150nm quartz supported zeolite film was inactive.

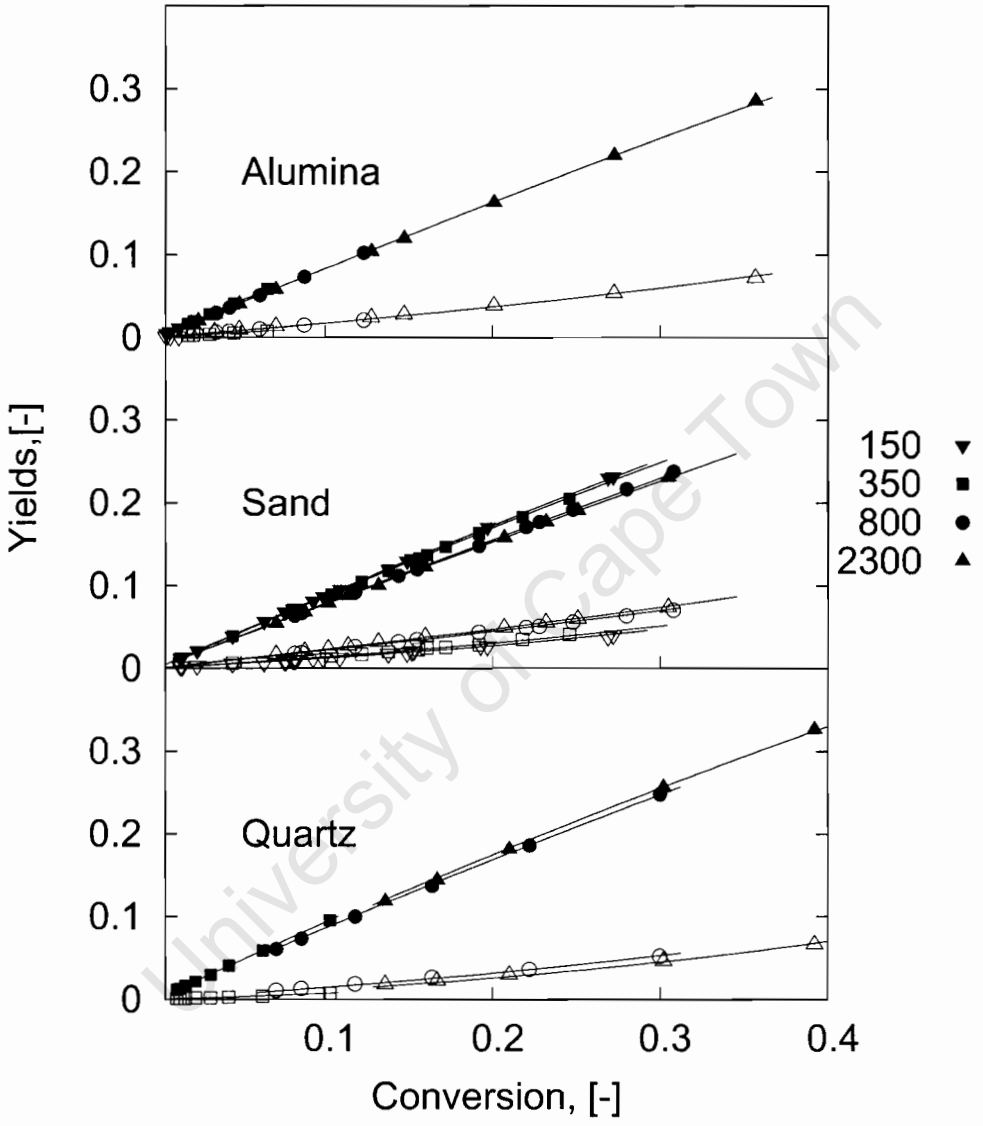

Figure 4.14: mX and oX yields as a function of conversion. Symbols - experimental data; closed symbols - oX yields; open symbols - mX yields; solid lines - model predictions. Legend indicates film thickness (nm). The 150nm quartz supported zeolite film was inactive.

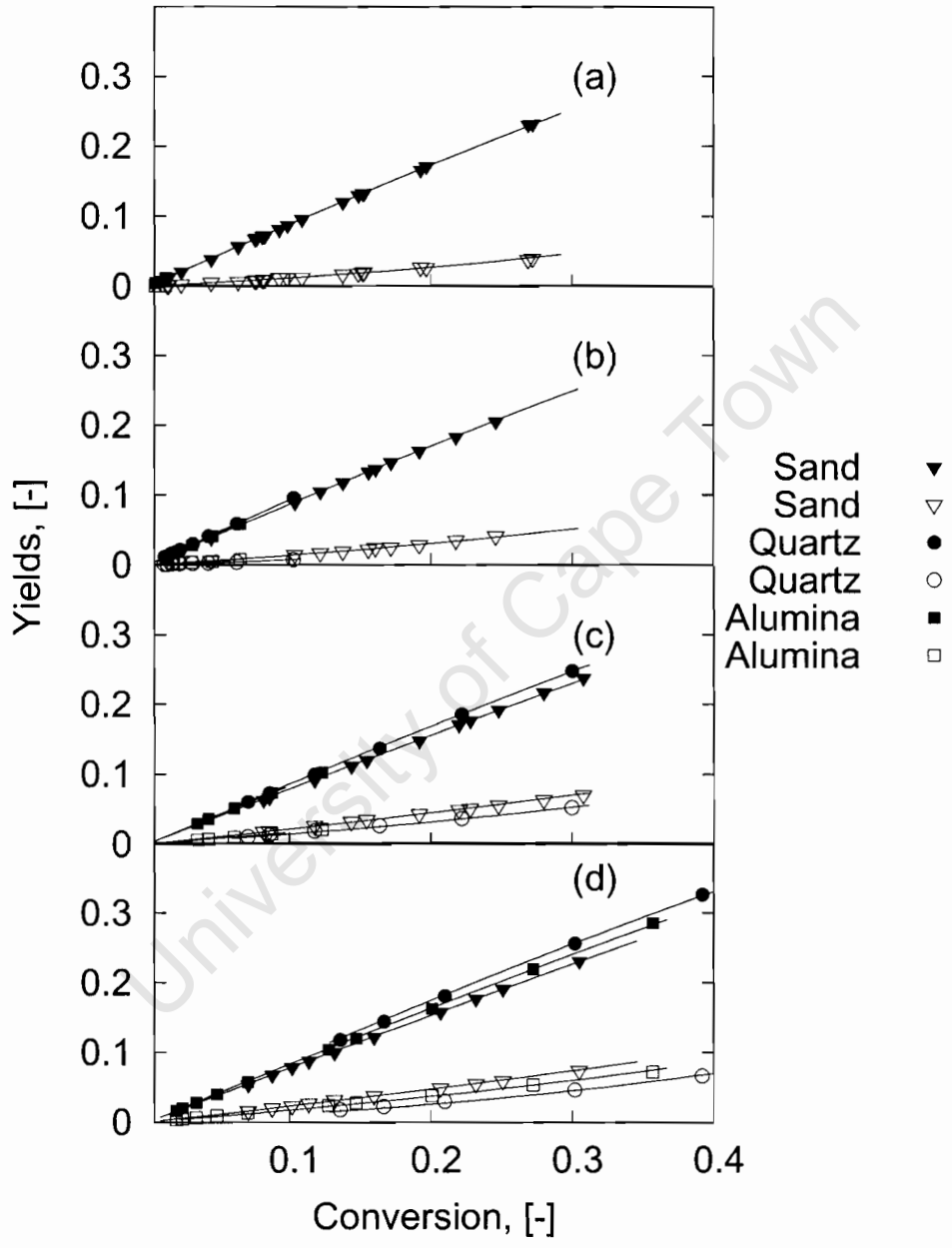

Figure 4.15: mX and oX yields as a function of conversion. Symbols - experimental data; open symbols - mX yields; closed symbols - oX yields; solid lines - model predictions; (a) 150 nm, (b) 350 nm, (c) 800 nm, (d) 2300 nm. The 150nm quartz supported zeolite film was inactive.

Figure 4.15 shows that oX yield increases in the order $quartz < alumina < sand$ and the mX yield decreases for two thickest films with support type in the order $quartz > alumina > sand$. For the thinner films the trend is not clear.

To compensate for the widely differing activities of the catalysts, the model has been used to extrapolate the data to provide similar conversions (figure 4.16). These data show that in all cases the zeolite supported on sand always has the smallest mX and highest oX yields respectively, indicating that these samples have the largest diffusion limitations. A more subtle observation is that the order of the yields observed for the thick films is repeated for both 800 and 350 nm films.

Figure 4.17, which was also plotted using the model to extrapolate the yield data, shows that the largest deviation in the yields with varying film thickness occurs in the alumina and sand supported zeolite films. This indicates that these films have larger diffusion resistances with increasing film thickness than the quartz supported zeolite film. Note that the diffusion-reaction interpretations on a yield-conversion diagram are independent of catalyst activity.

In order to illustrate the support and film thickness effects on selectivity, the ratio of mX : oX as a function of conversion has been plotted in figures 4.18 and 4.19. Figures 4.18 shows that the sand supported catalysts have the lowest mX : oX ratios, followed by alumina catalysts and then quartz catalysts. Figure 4.19 clearly shows that increasing the film thickness reduces the mX : oX ratio. From the theory (§1.10.1 and figure 3.6) the lower the mX : oX ratio the greater the diffusion limitations which indicates that the sand-supported catalysts have the strongest diffusion limitations.

The lines in figures 4.13-4.19 show that the diffusion model adequately represents the trend in the experimental data.

Further quantification of the reaction properties can be achieved by using the reaction diffusion model of §3.3.

Table 4.5: Estimated pX reaction-diffusion model parameters.

Catalyst	$k_1 \pm \sigma\%$	$\frac{D_{pX}}{T_f^2} \pm \sigma\%$	$D_{pX} \pm \sigma\%$	ϕ_{pX}
	s^{-1}	s^{-1}	10^{-10} m^2/s	
S150	6.68±2.5	9314±18	2.10±38	0.57±11.6
S350	3.21±3.7	3627±23	4.44±43	0.63±11.7
S800	7.03±3.6	3800±15	24±35	0.91±11.7
S2300	6.54±2.0	3144±7	166±27	0.96±11.9
A150	0.0378±1.4	126±20	0.028±40	0.37±11.5
A350	0.369±1.1	542±7	0.66±27	0.55±11.8
A800	0.387±1.6	318±7	2.0±27	0.74±11.7
A2300	1.01±2.0	797±10	42±30	0.75±11.8
Q150	-	-	-	-
Q350	2.15±3.3	6841±44	8.38±64	0.37±12.1
Q800	7.67±2.6	8063±15	52±35	0.65±11.8
Q2300	5.8±2.0	9266±17	490±37	0.53±11.7

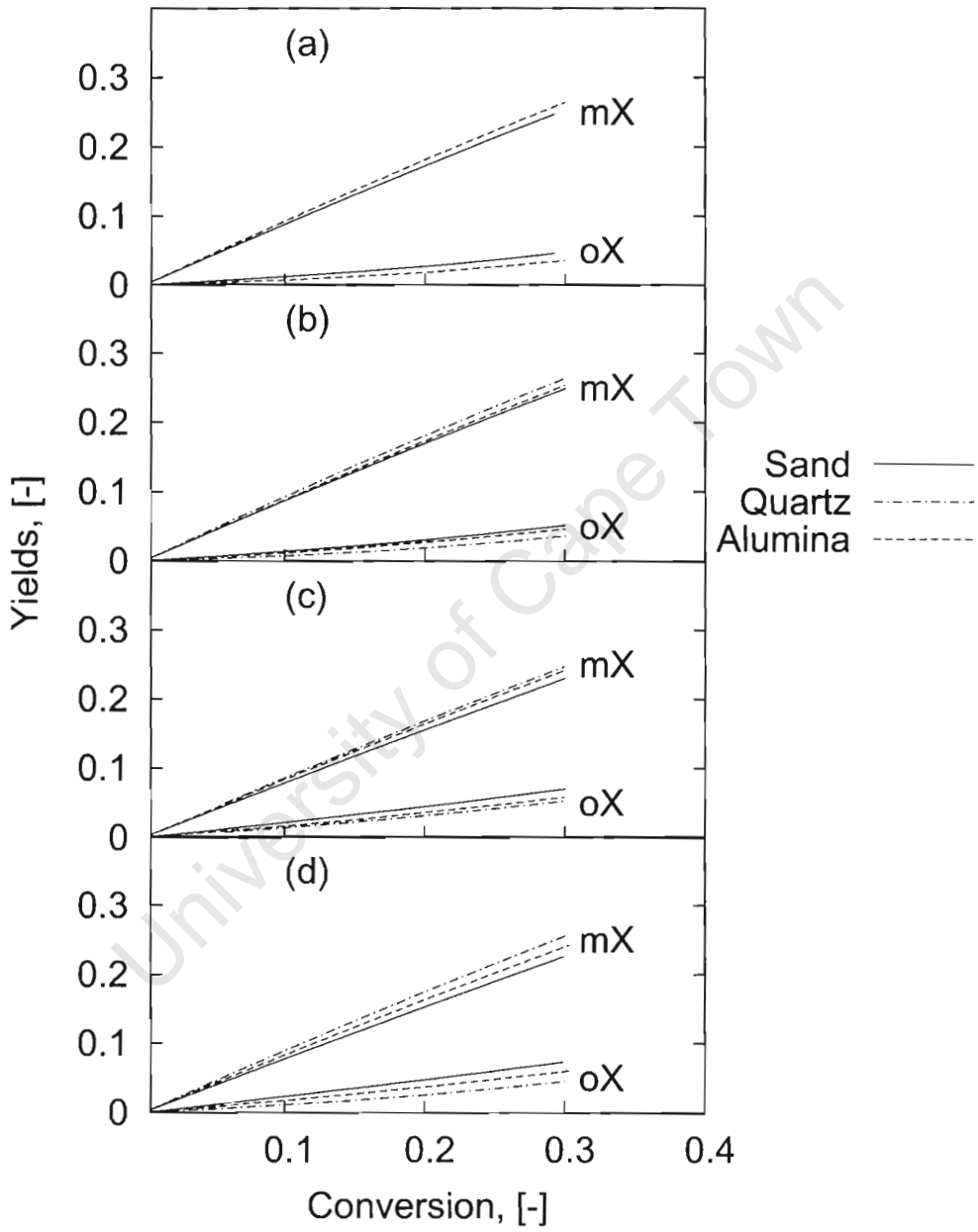

Figure 4.16: mX and oX yields extrapolated using the model as a function of conversion ; (a) 150 nm, (b) 350 nm, (c) 800 nm, (d) 2300 nm. The 150nm quartz supported zeolite film was inactive.

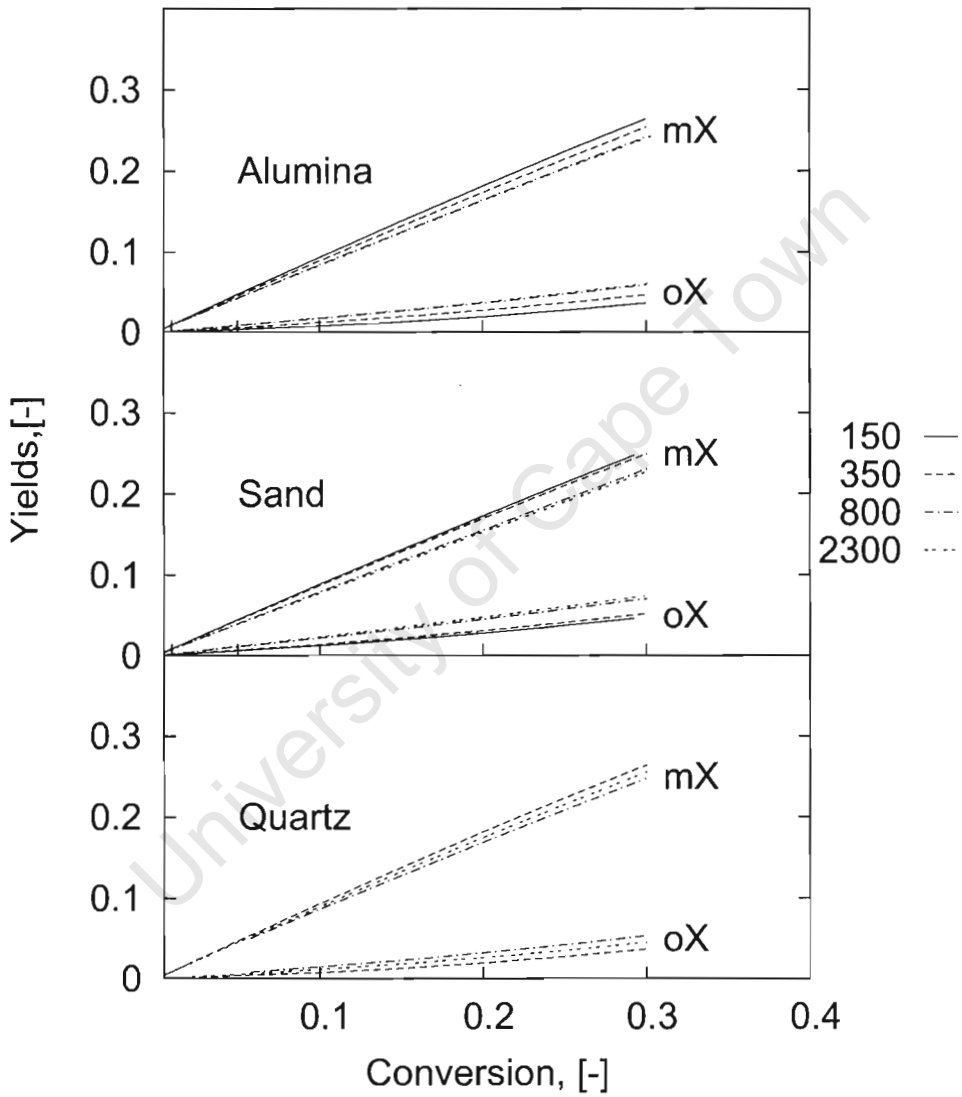

Figure 4.17: mX and oX yields extrapolated using the model as a function of conversion per catalyst. Legend indicates film thickness (nm). The 150nm quartz supported zeolite film was inactive.

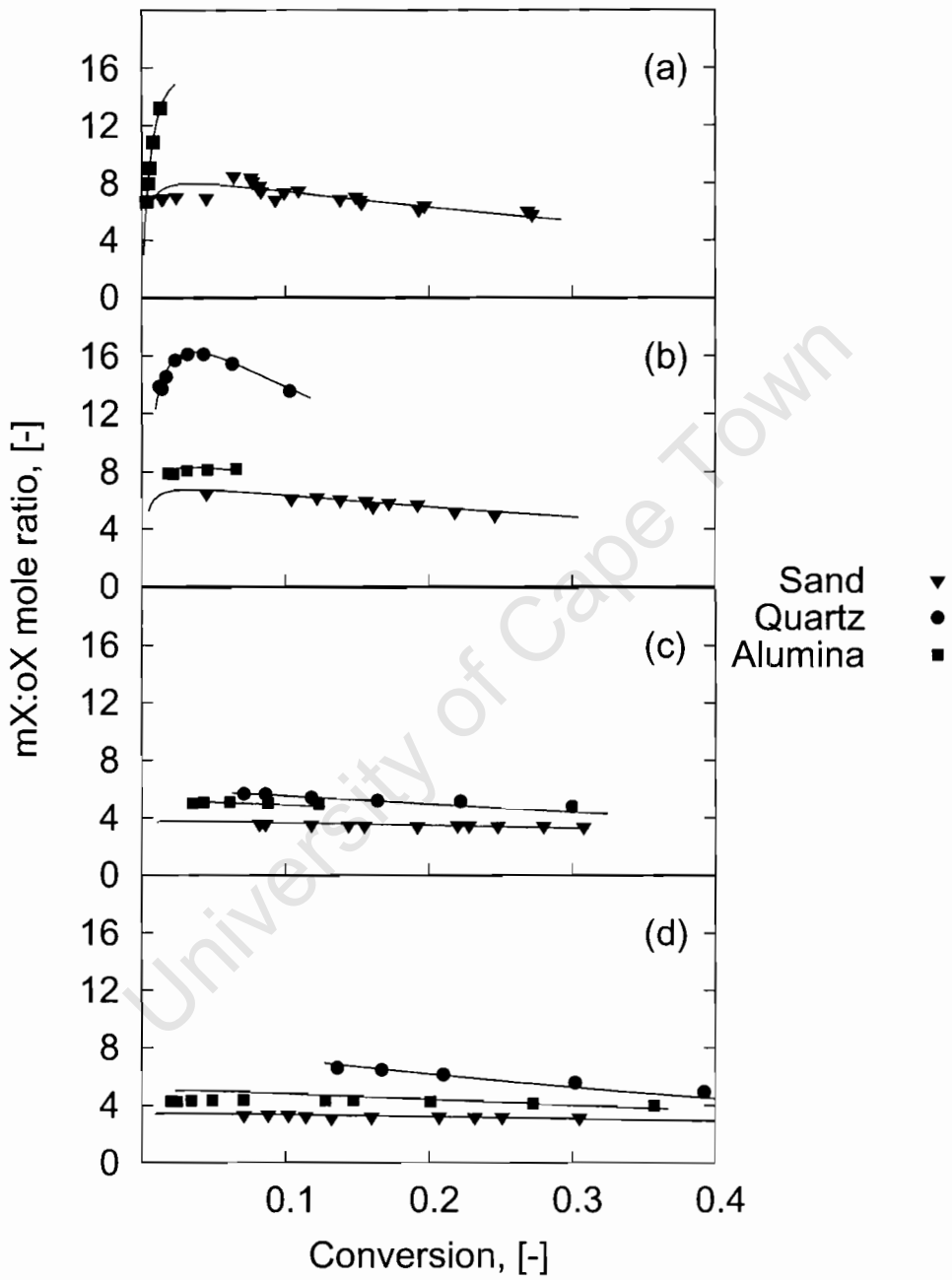

Figure 4.18: mX:oX mole ratio as a function of conversion. Symbols - experimental data; solid lines - model predictions; (a) 150 nm, (b) 350 nm, (c) 800 nm, (d) 2300 nm. The 150nm quartz supported zeolite film was inactive.

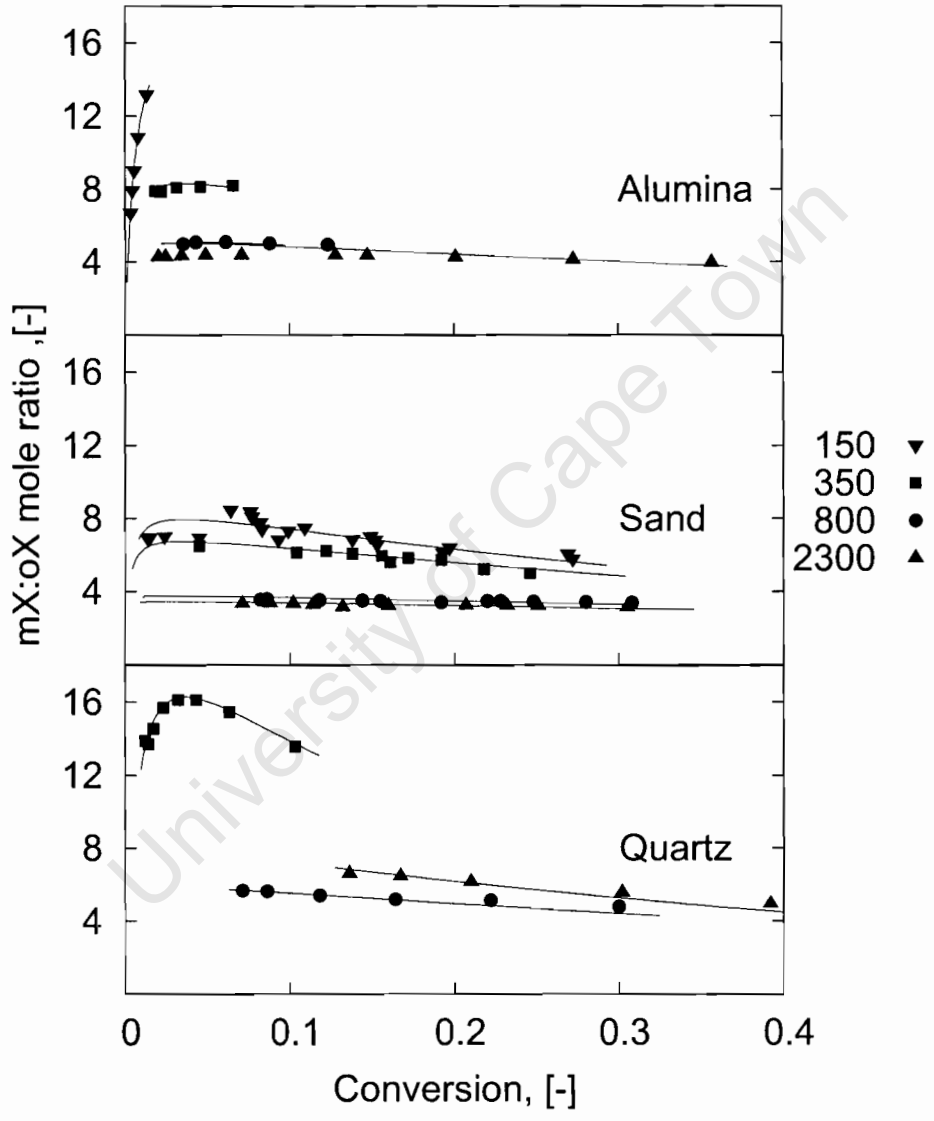

Figure 4.19: mX:oX mole ratio as a function of conversion per catalyst. Symbols - experimental data; solid lines - model predictions. Legend indicates film thickness (nm). The 150nm quartz supported zeolite film was inactive.

Table 4.5 shows the model parameters (diffusivity D_{pX} and rate constant k_1) that have been estimated from the experimental data.

It can be seen that the rate constant can be estimated more reliably (to within 3%) than the diffusion time constant (to within 20%). This is a result of the type of data that is being used for parameter estimation, the limited range of the conversion, and the sensitivity of the model to the model parameters. The rate constant is highly sensitive to the residence time vs conversion data. A small deviation in the rate constant leads to a significant shift in the conversion-residence time curve. On the other hand the diffusion coefficient is sensitive to the deviation of the yield vs conversion data from the intrinsic sequential reaction pathway dictated by ratio of k_1 to k_2 which is held constant in the model. The diffusivity has to vary by a few orders of magnitude to shift the mX and oX yield and ratio curves between a condition of no diffusion limitation to a condition of maximum limitation (figures 3.5 and 3.6). It is only within this region of diffusion time constants (D_{pX}/T_f^2) that the diffusivity can be reliably estimated, and even then its accuracy remains low unless experimental scatter can be eliminated. From the table (4.5)

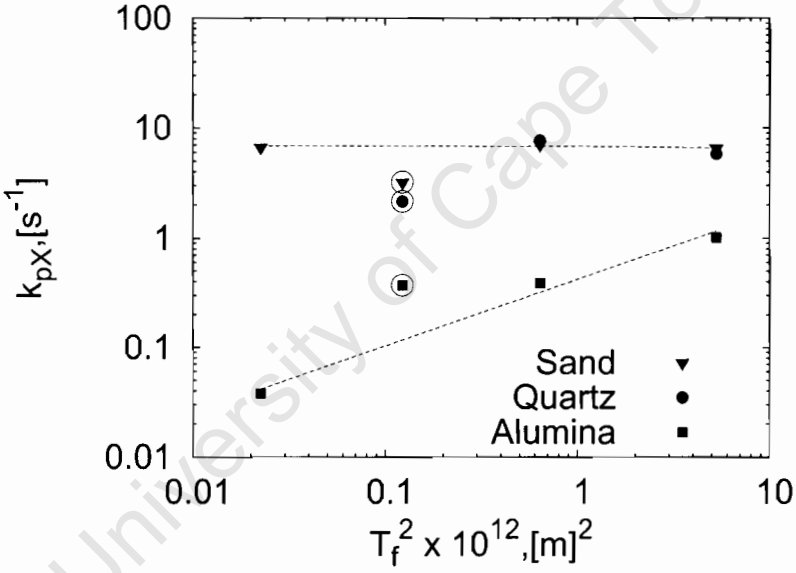

Figure 4.20: Plot of pX rate constant as a function of film thickness. Encircled data - outliers. The 150nm quartz film was inactive.

and figure 4.20, it is clear that the rate constants for the sand and quartz supported zeolite catalysts are within the same order of magnitude irrespective of film thickness. There is no consistent trend with film thickness for these catalysts. In contrast, the alumina catalysts have rate constants 1-2 orders of magnitude lower than the sand and quartz catalysts. These rate constants also increase with increasing film thickness.

Shown in figure 4.21, diffusion coefficients of the quartz supported catalysts are consistently higher than those of the sand-supported catalysts, although the diffusivities are within the same order of magnitude as the sand supported zeolite films. The alumina supported catalyst have an order of magnitude lower diffusion time constants than the sand and quartz catalysts. The diffusion coefficient is estimated to lie between 10^{-9} and 10^{-10} m^2s^{-1} and decreases in the order

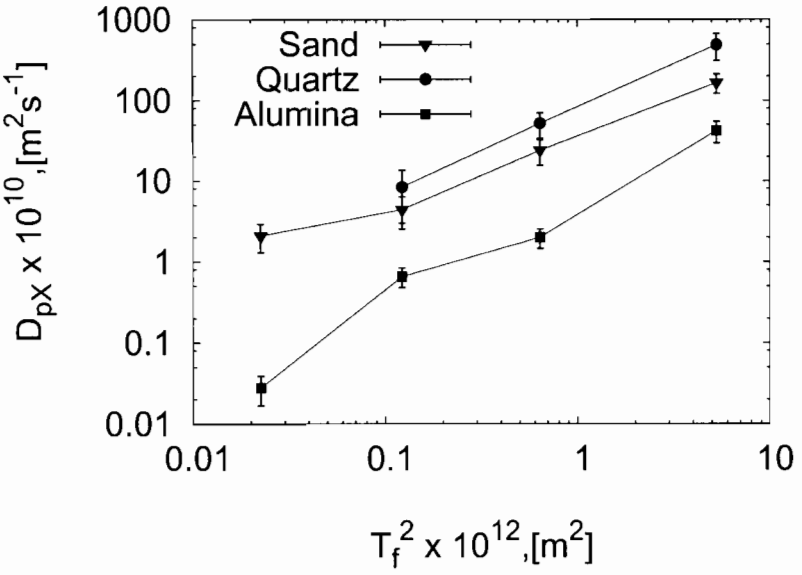

Figure 4.21: Plot of pX diffusivity as function of film thickness. Error bars shown. The 150nm quartz film was inactive.

quartz > *sand* > *alumina*. More importantly, the diffusion coefficient increases with increasing film thickness consistently for all catalyst supports. This contradicts the assumption that the film properties are uniform in that the diffusion coefficient should be independent of film thickness.

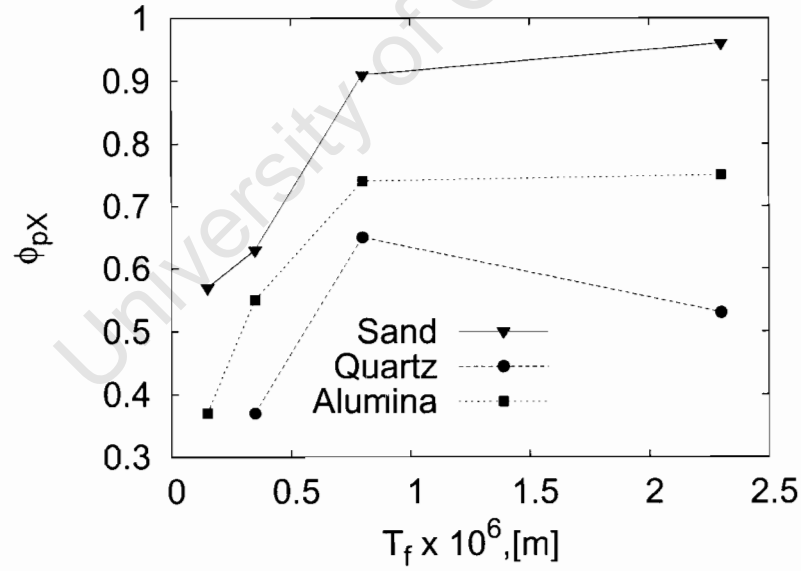

Figure 4.22: pX Thiele modulus as a function of film thickness. The 150nm quartz film was inactive.

The approximate Thiele modulus (equation 2.12) for pX varies between 0.4 and 1, the higher values being for the thick films. Illustrated in figure 4.22, the Thiele moduli decrease in the order *sand* > *alumina* > *quartz*. This corresponds to the selectivity changes observed in figures 4.14 - 4.19. Although a Thiele modulus less then 1 for first order irreversible reactions does not normally signify strong diffusion limitations, the diffusion coefficients of the mX and oX are 2-3 orders of magnitude smaller than those of pX, which means that both products would be subject

to strong diffusion limitations within the pores of the zeolite film. Thus large selectivity changes as a result of diffusion limitations might be expected, but this has not occurred here, which is a result of the reversibility of the reaction steps.

4.3 TEOS deposited onto the sand supported zeolite films

Figure 4.23 shows a typical breakthrough curve obtained for the deposition of TEOS on the sand supported zeolite catalysts. The 1^{st} and 15^{th} cycle show that the biggest difference in the deposition occurred during the first low temperature stage while the flushing step seemed to remain the same.

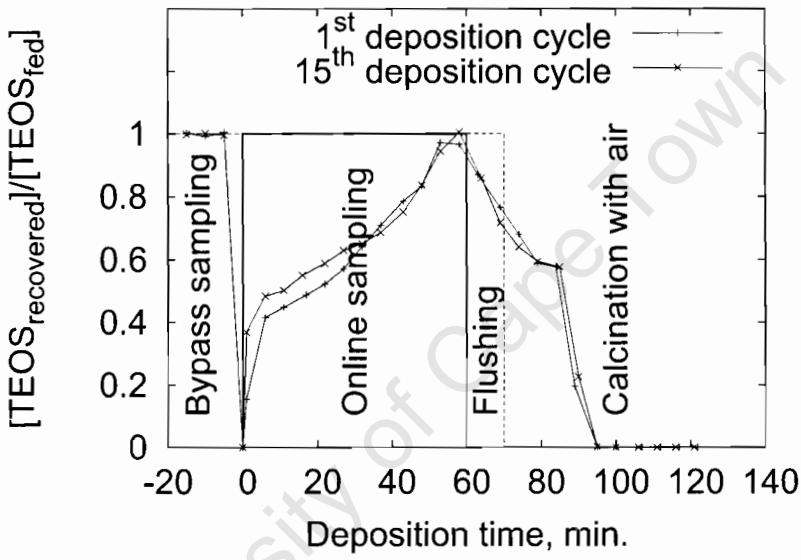

Figure 4.23: Breakthrough curves from CVD of TEOS on sample S350.

The scatter in the integral TEOS conversion shown in figure 4.24 shows how experimental and numerical difficulties affect the accuracy of evaluating the amount of SiO_2 deposited on the surface of the zeolite by this method. However, when viewed on a cumulative plot in figure 4.25, the approximate linear increase in the amount of silica deposited per cycle can be clearly seen.

4.3.1 TIPB cracking over sand supported zeolite films modified by CVD

Following the approach by Röger et al. [2001], the effects of stepwise silanisation are investigated by monitoring the fraction of the surface not deactivated after each silanisation step. This is done by using equation 4.4, which represents the fraction of accessible external acid sites (A/A_0) as a function of the number of cycles (n):

$$ln\left(\frac{A_n}{A_0}\right) = ln\left(\frac{k_n}{k_0}\right) = ln(\alpha^n) = n(ln\alpha) = n(slope) \tag{4.4}$$

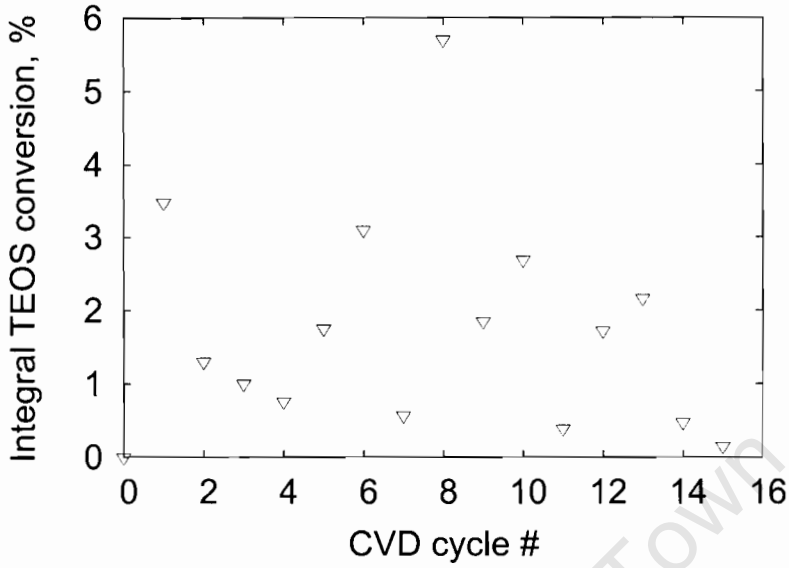

Figure 4.24: Integral TEOS conversions on sample S350.

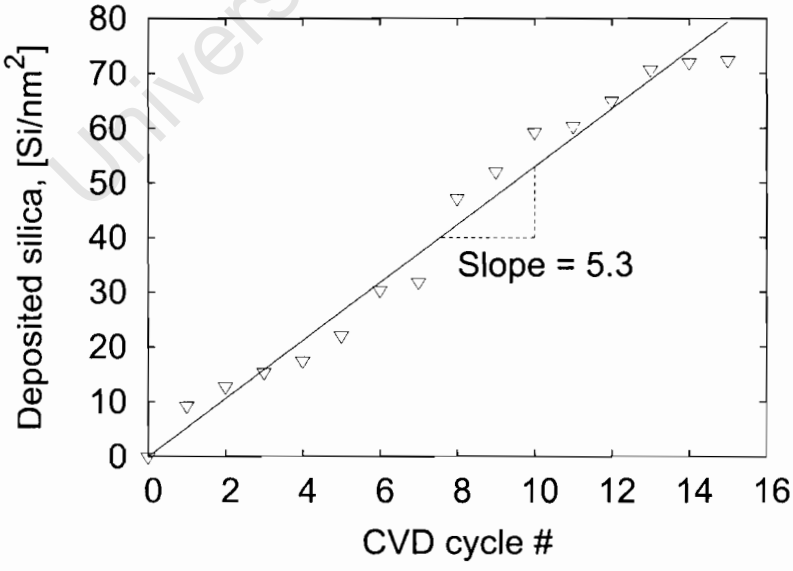

Figure 4.25: Cumulative silica deposition on sample S350.

where A_n is the number of accessible acid sites on the external surface after n deposition cycles, A_0 before deposition, and α^n the fraction of external sites still accessible after n deposition cycles. Application of equation 4.4 in figure 4.26 yields $\alpha = 0.63$, which implies that after each deposition cycle, 37% of external acid sites are rendered inaccessible. In their investigation of the inertization of ZSM-5 powder, Röger et al. [2001] found a 55% decrease of external sites per deposition cycle. Details of their experimental conditions are shown in table 4.6.

Table 4.6: Experimental conditions for the silanization (with TEOS) of ZSM-5 powder. After Röger et al. [2001].

Si/Al	25
d_p (μ)	0.5-1.5
mass (mg)	100
Diluent	2.9g quartz
XTEOS (%)	< 5
T_{CVD} (℃)	100
p_{TEOS} (kPa)	0.4
WHSV (h-1)	1.5
# CVD steps	16

The amount of Si deposited can be related to the cycle number by assuming a linear relationship in figure 4.25. In analogy to equation 4.4, figure 4.27 can be represented by equation 4.5:

$$\frac{k_n}{k_o} = \alpha_s^{n_s} \tag{4.5}$$

where n_s= (slope of figure 4.25)$\cdot n$ and $\alpha_s = \alpha^{\frac{1}{5.3}}$.

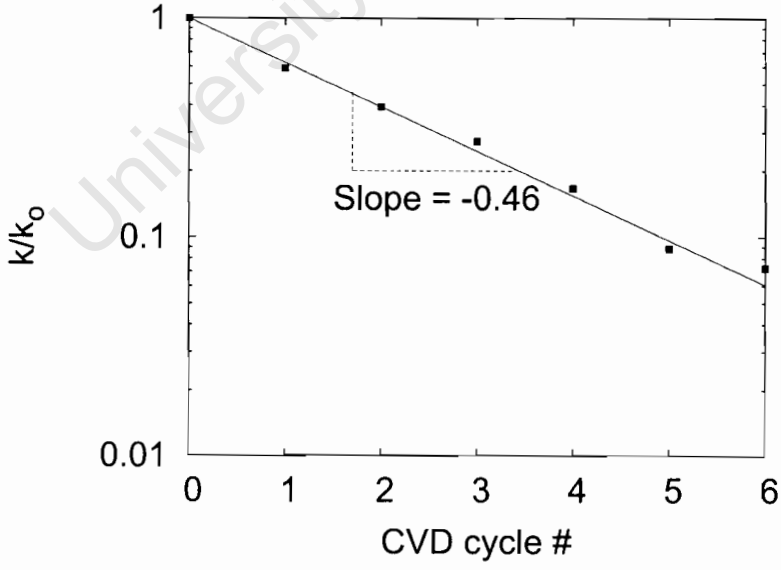

Figure 4.26: Plot of $k/k_{o_{TIPB}}$ as a function of the number of silica deposition cycles.

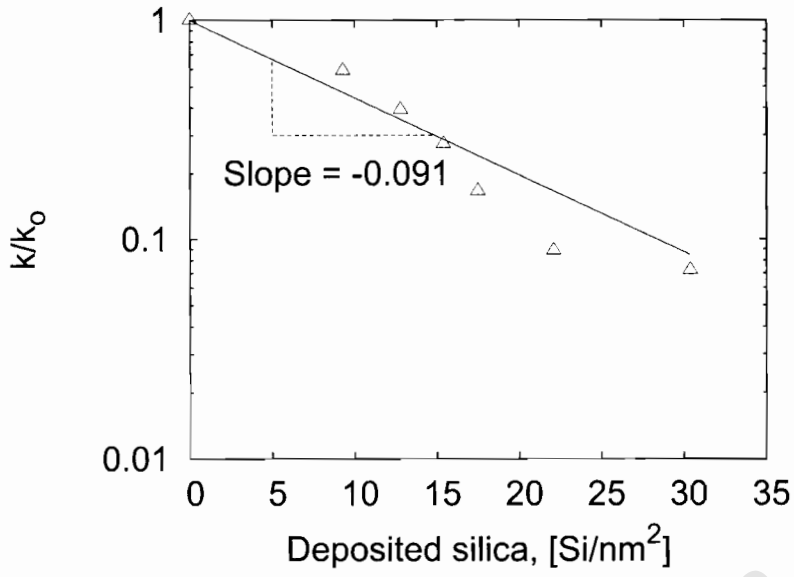

Figure 4.27: Plot of k/k_{oTIPB} as a function of silica density.

4.3.2 pX isomerization over sand supported zeolite films modified by CVD

Figures 4.28 and 4.29 show that the both the mX and oX yields decrease with an increase in the amount of silica deposited (increasing cycle number) which is largely due to the decrease in conversion. The model adequately represents the data, the 0 and 15 cycles enveloping all the intermediate results.

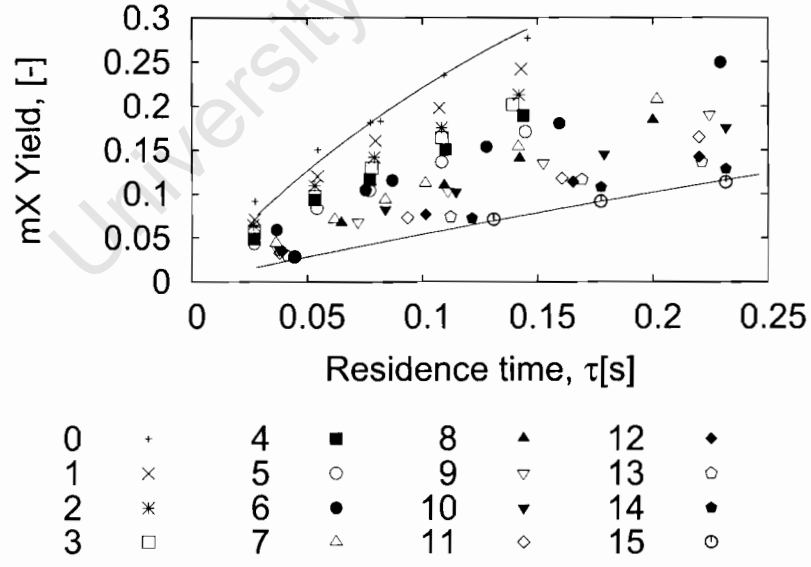

Figure 4.28: mX yields as a function of residence time. The legend shows the number of CVD cycles on sample S350. Solid lines are model fits after 0 and 15 CVD cycles.

Figure 4.30 shows that the relative Thiele modulus for pX is approximately constant as a function of the silica deposited. This shows that CVD has no influence on the diffusion properties and hence selectivity of the catalyst. The decrease in diffusivity can be coupled to the decrease in

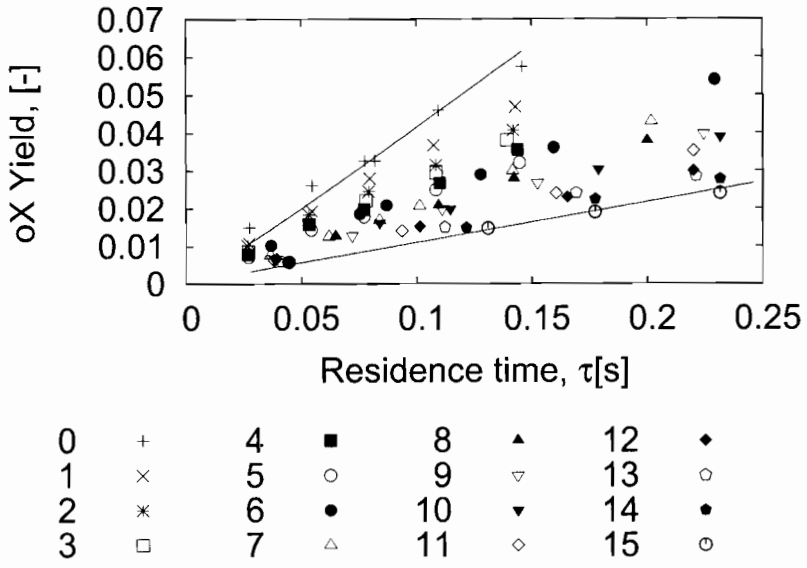

Figure 4.29: oX yields as a function of residence time. The legend shows the number of CVD cycles on sample S350. Solid lines are model fits after 0 and 15 CVD cycles.

the rate constant[1], the scatter in the data, and the parameter estimation procedure. This poor influence of CVD is confirmed by figures 4.31 and 4.32, which show that there is no variation of selectivity with silica deposition and that, as is more lucidly illustrated in figure 4.33, the increased silica deposition only modifies the activity of the film.

Figures 4.33 and 4.34 show that pX activity and diffusivity decrease with an increase in the silica deposited onto the sand supported zeolite film. The pX rate constant and diffusivity after 30 Si/nm^2 has been deposited is about 2.5 times greater than the TIPB rate constant. The diffusivity shows a larger decrease with increasing Si deposited than the pX rate constant.

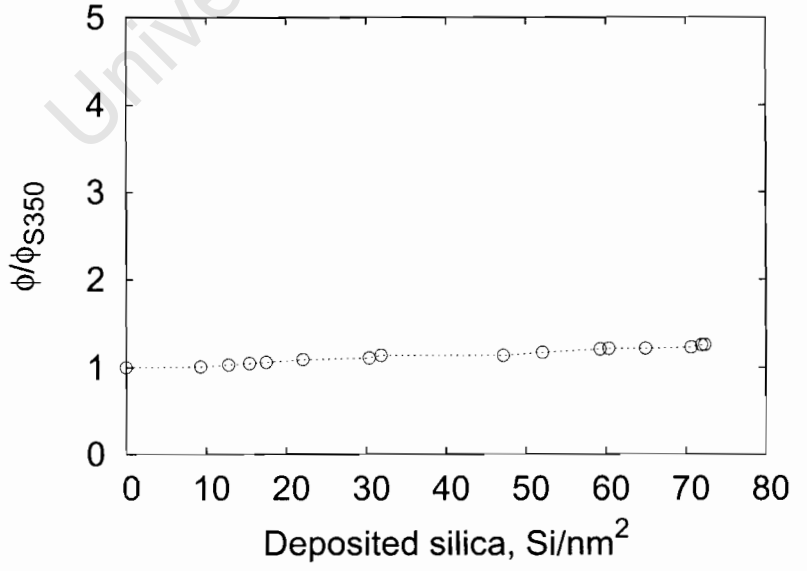

Figure 4.30: Thiele modulus dependency on silica deposition on sample S350.

[1]This coupling was observed in §3.3.5.

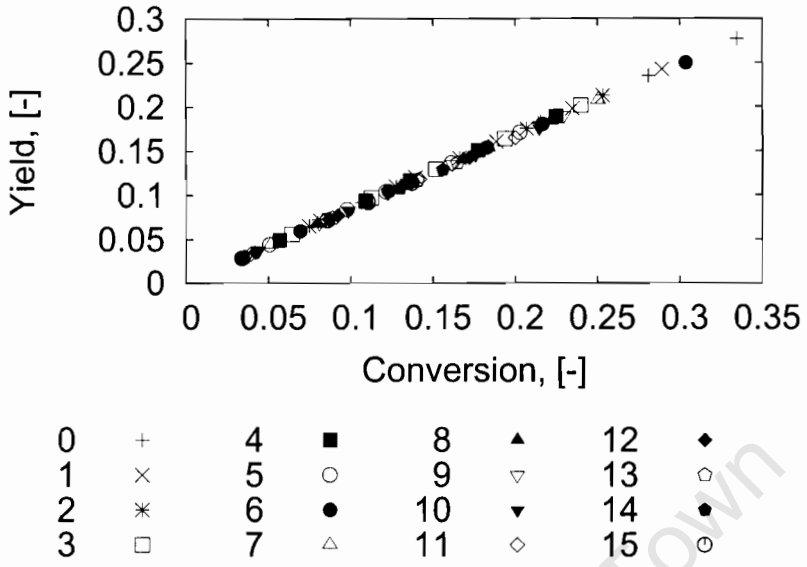

Figure 4.31: mX yields as a function of conversion. The legend shows the number of CVD cycles on sample S350.

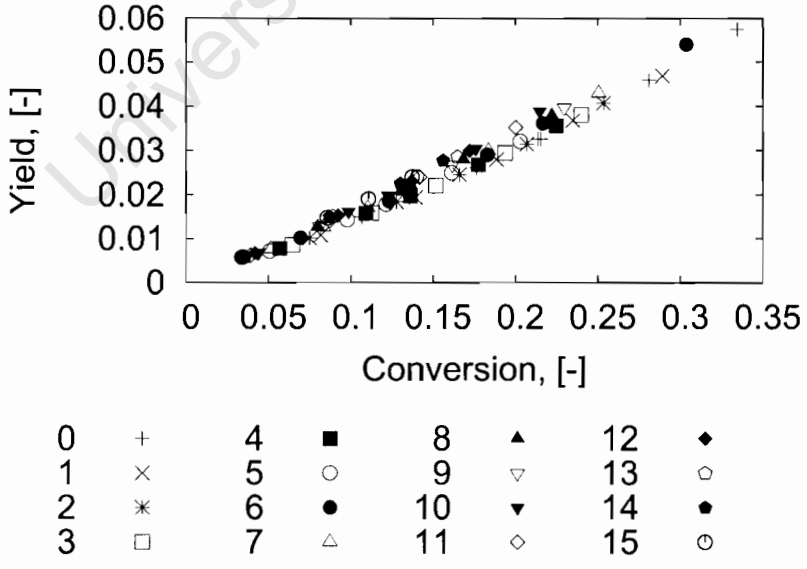

Figure 4.32: oX yields as a function of conversion. The legend shows the number of CVD cycles on sample S350.

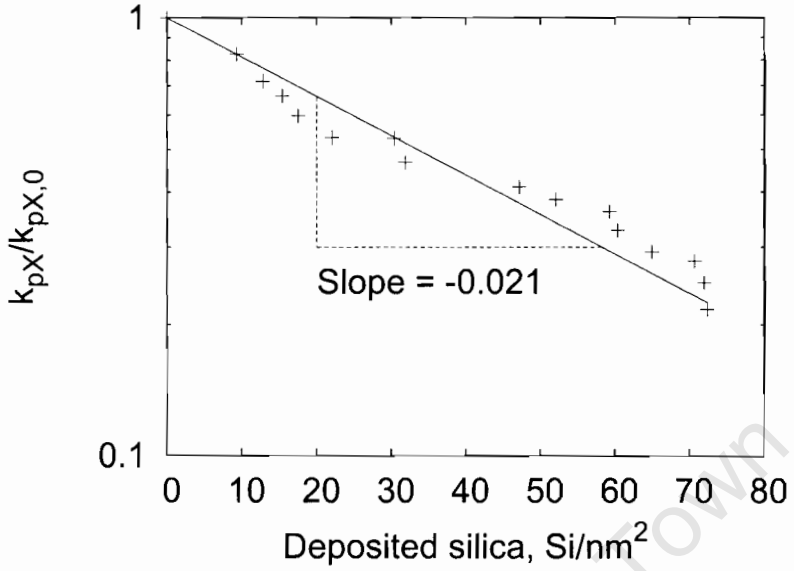

Figure 4.33: pX rate constant as a function of silica deposition.

D

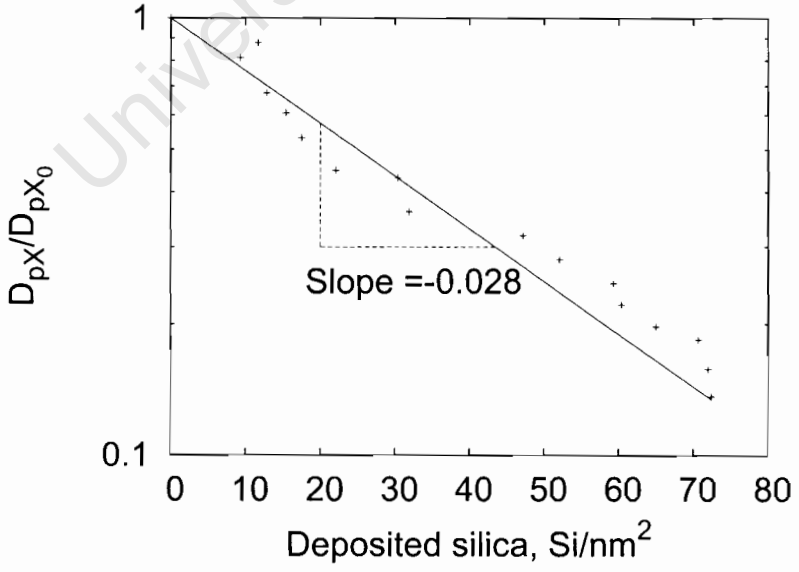

Figure 4.34: Variation of pX diffusivity with silica deposition.

Chapter 5

Discussion

This chapter discusses results of the physical and reaction work characterization. The results are also interpreted using the current understanding of catalysts and reactor modelling, and compared to available literature data.

5.1 Film synthesis and physical characterization

Before any attempt is made to discuss the reaction results, a clear picture of the film properties based on physical characterization is necessary.

Zeolite loading (or growth rate) is strongly dependent on the available surface area based on the support geometry and not on the support BET surface area which includes micro and meso pores. The seeds being approximately 60 nm in size would preferentially fill/block all pores less than 200 nm. Film growth would then essentially be on a smooth surface approximated by the particle geometry. The quartz and the sand supports conform to this regime of film growth (figure 4.3).

The alumina, as shown by the SEM (figure 4.6 (a)) and BJH surface area results (figure C.1) has surface voids larger than 100 nm, thus an extended surface area which is greater than the surface area based on the geometry but less than that determined by BET analysis (figure 4.3). Zeolite growth thus occurs on a continuously decreasing area as the zeolite film proceeds to block the voids with increasing film thickness. However, figure 4.3 shows that the estimated surface area for the alumina remains constant with increased zeolite loading and does not show the expected decreasing trend towards the non-porous surface area. Therefore the alumina film does not grow on a smooth surface and most likely does not produce a smooth film, thus questioning the validity of the SEM film thickness approximations.

Film thickness, as determined by SEM, is proportional to the number of growth cycles. SEM analysis confirms the interpretations made from the surface area analysis. These results show that the quartz and sand films, although not microscopically smooth, may be assumed to be macroscopically smooth. In contrast, the alumina supported zeolite is macroscopically rough,

resulting in significant irregularities in the film thickness and possibly incomplete coverage as suggested by the EDX analysis of the surface properties. However, SEM analysis was unable to provide a deeper understanding of the film properties which would lead to better quantification of the surface properties of the zeolite film supported on alumina.

Further in depth analysis of the film using SEM and other techniques would lead to a 2- or 3-dimensional representation of the zeolite film geometry. However, this would defeat the objective of applying a simple 1-dimensional reaction-diffusion model to interpret the reaction data. Such a model would in any case require averaging of the zeolite film properties to a 1-dimensional geometry and thus for further analysis, it has been assumed that the film thickness and surface area as estimated from N_2 adsorption and SEM will be used as a first approximation to all samples.

More complications also arise with regard to the sand and alumina supported films. At higher zeolite loadings, agglomeration of the sand particles due to the film filling the voids between the particles occurred. The mechanical breakage of these agglomerates and growth limitations due to nutrient limitations into the agglomerate, are expected to cause irregularities in the film growth and a variation in the surface area. Figure 4.3 does not show any significant variation in the surface area and thus it appears that the zeolite films have remained uniform. However, agglomeration might lead the additional reactant/product diffusion limitations during pX isomerization.

The alumina support allowed the migration of Na^+ ions into the zeolite film during calcination and also during reaction (at the high reaction temperatures viz. 450℃), leading to acid site deactivation and a variation of catalytic properties through the zeolite film. Results in table 4.3 show that the acid site concentration near the external surface decreases with increasing film thickness, although these results are subject to strong interference from the support, as the H was not measured, but obtained from equation 4.3 using the Al and Na measurements. This result is not expected if the Na^+ migration follows a diffusion mechanism (see §4.1.5). Estimation of the bulk acid site content, using for example temperature programmed desorption, is complicated by the migration of the Na^+ ions during pretreatment and analysis. Further evaluation of the acid site content of the alumina sample was not attempted. Thus, strictly speaking, only the quartz supported zeolite film conforms to the idealized smooth film concept and obeys the reactor model assumptions with respect to physical properties.

No large cracks were observed in the SEM images, although as will be shown later, these have very little bearing on the performance[1] of the catalyst samples, in particular the pX reaction.

In summary, the surface areas and film thicknesses in table 4.2 are assumed to be valid for all samples. The decrease in the surface area with film thickness is largely due to the increased loading as shown in figure 4.3. Thus for the same total catalyst loading (support + zeolite) in the reactor, the surface area exposed to the reactants is approximately constant for each support

[1] In zeolite membranes, however, cracks impact negatively on the desired molecular sieving effect [Geus and van Bekkum, 1995].

and in proportion to each different support (sand : alumina : quartz is approximately 0.02 : 0.01 : 0.0015) as estimated from figure 4.3. These thus represent the approximate active surface areas for the TIPB cracking reaction. In contrast, for the pX reaction, increasing the zeolite loading (*i.e.*, film thickness) does not change the external surface area (as would be the case for flat plate geometry) thus preempting the occurrence of diffusion limitations for the thick films. This is in contrast to increasing zeolite crystallite size (assumed spherical), in which the external surface area also increases. However, this increase on a per mass basis is not as rapid as it would be by adding more crystals of the same size. With this conceptual image of the zeolite supported films, the interpretation of the reaction data can proceed.

5.2 Reaction characterization

These data are to a certain degree dependent on the interpretation and assumptions made with regard to the physical characterization of the film. Assumptions made in §4.1 and §5.1 are embedded in the analysis strategy taken in the reaction work *i.e.*, smooth films, surface area and homogeneous acid site distribution.

5.2.1 Activity of the external surface

TIPB cracking rate constants are directly proportional to the acid site concentration on the external surface. Figure 4.10 shows that for the quartz and sand supported zeolite the activity and hence the acid site concentration of the external surface is approximately constant with increasing film thickness when account is taken of the possible variation in film thickness, surface area and zeolite loading. These results thus support the assumption that these zeolite films are smooth and uniform.

The alumina supported zeolites show that the acid site concentration on the external surface increases with increasing film thickness and that for the thickest film equals that of the sand supported zeolite film. These results contradict the EDX measurements in table 4.3 but support the theory that the Na^+ migration is a diffusion controlled process (see §4.1.5).

Another explanation for this behavior is that the incomplete coverage and non-uniform film thickness could lead to less external surface acid sites for the thin films than predicted by the uniform film thickness assumption, leading to the lower rate constants and the increase with increasing film thickness. This is supported by the decrease in the Al content with increasing film thickness shown in table 4.3. Thus the zeolite film supported on alumina is most likely non-uniform and, in the case of the thinner films, incomplete. Furthermore, Na^+ exchange has also occurred to a significant extent as shown by the variation of the Na/H ratio representing the degree of exchange obtained on the external surface.

In their investigation of the viability of a single step iron-based Fischer Tropsch (using an alkali as the promoter and H-ZSM-5 powder as co-catalyst), Botes and Böhringer [2004] found that

severe alkali migration results from mixing the two catalysts. Their experiment was carried out under conditions specified in table 5.1.

Table 5.1: Experimental conditions. After Botes and Böhringer [2004].

Catalyst loading	
Iron	5g (unreduced mass)
HZSM-5	5g
Reduction conditions	
Reduction gas	Hydrogen
Gas space velocity	200 ml/min/g unreduced iron catalyst
Temperature	420℃
Pressure	20 bar

5.2.2 Activity and selectivity of the zeolite film

Intrinsic activity of the zeolite pores

These supported zeolite films all followed the same preparation procedures and should therefore show similar activity. Results indicate that this is the case for the sand and quartz supports but not for alumina supports (figure 4.13). Based on the intrinsic first order isomerization rate constant, k_{pX} (table 4.5), which represents the true active site activity without any influence of diffusion limitations, the activity follows the order : $sand \approx quartz > alumina$. k_{pX} thus provides a direct measure of the "homogeneous" acid site concentration within the zeolite pores.

These results are also consistent with the activity of the external surface (k_{TIPB}), which show that the activity for the alumina supported zeolite increases while the activity of the sand and quartz supported zeolite remained constant with increasing film thickness (figures 4.10 and 4.20). However, the difference in bulk activity between the alumina supported zeolite and the sand and quartz supported zeolite is an order of magnitude larger for the pX isomerization than for the TIPB cracking. Furthermore, the pX activity of the thickest alumina supported zeolite film, A2300, remains an order of magnitude below that of S2300 and Q2300 while the external surface activity is similar.

These observations are supported by the physical characterization of §5.1. While the quartz and alumina supported zeolite films behave more like smooth homogeneous films (based on activity), the alumina supported zeolite shows large variation with film thickness.

If the migration of the Na^+ ions were to homogeneously distribute over the zeolite intracrystalline surface, then it would be expected that the activity ratio between alumina supported zeolites and the other supports for both TIPB and pX reactions should be the same, which is not supported by the results in figure 5.1. If, in contrast, the migration of Na^+ ions follows a diffusion mechanism, then there would be an acid site concentration gradient within the alumina supported zeolite films in which the lowest number of active sites would be located at the support-zeolite interface.

This leads to a larger decrease in activity of the zeolite pores when compared to the external surface activity because the average acid site concentration, as estimated by the pX rate constant (k_{pX}), is considerably lower than the surface acid site concentration. Furthermore, the exchange of H^+ with Na^+ will be much higher in the thin films leading to the increasing activity with film thickness. Thus it is also possible that for the thickest films, there is considerable Na^+ migration into the pores of the zeolite without significantly influencing the external surface activity, which is described by figure 5.1.

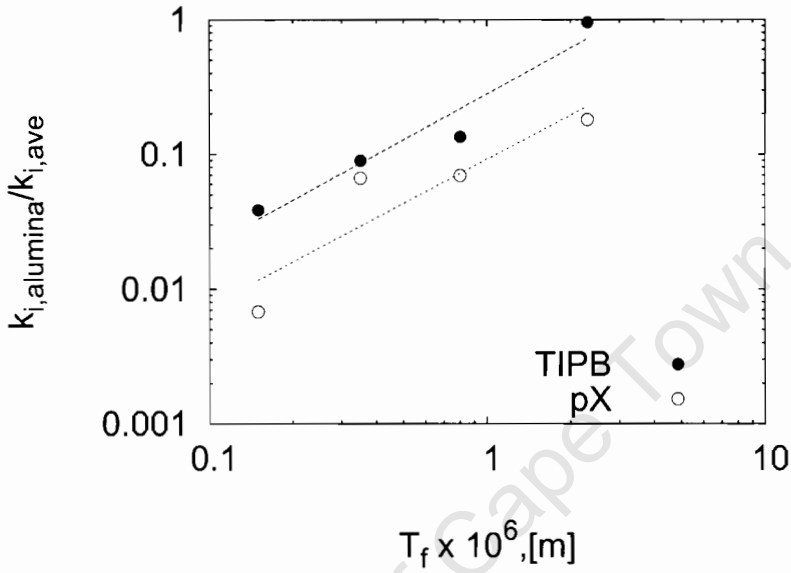

Figure 5.1: Normalized reaction rate constants as a function of film thickness for pX isomerization and TIPB cracking on the alumina catalysts. Normalization is with respect to the average values for the quartz and sand catalysts. Symbols - data; broken lines - trendlines.

The reaction-diffusion model provides only an average intrinsic rate constant and is not able to provide any information regarding the acid site (or activity) profile that might exist within the zeolite film. A concentration profile within the zeolite film not only reduces the activity, but also modifies the selectivity, over and above any diffusion limitations that might be occurring.

It is difficult to compare absolute rate constants for pX isomerization with literature data. However, previous work [Manstein, 2001] using ZSM5 pellets (Si/Al = 44) and toluene disproportionation as a test reaction at 450℃, estimated a rate constant for xylene isomerization of 28 s^{-1} using a first order reaction network and a reaction diffusion model with the incorporation of deactivation due to CVD. The average rate constant obtained from this work for the quartz and sand supported zeolite film was 6. These are of the same order of magnitude and is surprising considering the different preparation methods and reactions that were used.

Influence of film thickness on selectivity

Both support type and film thickness influence the selectivity of the pX reaction. Due to the variation in activities, especially for the alumina supported zeolite films, it is more convenient to

base the discussion on trends observed using model data and yield ratios over a similar conversion range (figures 4.16-4.19) and the intrinsic diffusion parameters of table 4.5.

The yield to oX decreases with respect to support type for all film thicknesses in the order *sand* > *alumina* > *quartz*. Theory (§3.3.5 and figure 3.6) indicates that increasing yields of oX represent increasing influence of diffusion limitations on the reaction pathway. In this model it has been assumed that the intrinsic reaction pathway (kinetics) is the same for all catalysts as the same reaction is being studied and the same acid sites (same zeolite) are being used to catalyze the reaction. Thus the ratio $\frac{k_2}{k_1} = 2$ determines the intrinsic yield of oX and mX as a function of conversion independently of the magnitude of the rate constants, and, *ipso facto*, all the catalysts studied should have the same yield - conversion (or mX:oX ratio - conversion) plots when diffusion limitations are negligible. This is clearly not the case (see figures 4.18 and 4.19). It follows, then, that all samples have significant deviations from intrinsic kinetics, indicating significant diffusion limitations, except the thinner quartz and alumina supported zeolite films.

Increasing the film thickness also increases the yield of oX, as would be expected for increased diffusion limitations (§3.3.5). However, the film thickness increases by a factor of 15, which leads to an increase in diffusion time constant, D/T_f^2, by a factor of 225. This is not observed in the data in table 4.5, which show less than a factor of 5 variation in the diffusion time constants. If the thinnest active film for each supported zeolite is used as a reference and the rate constant is held constant, predicting the selectivity of the thickest film leads to significantly lower conversions (figure 5.2) and higher selectivities to oX (figure 5.3) than is observed for the experimental data.

Theoretically it is shown (figures 3.4 and 3.5) that an approximately 2 orders of magnitude increase in D/T_f^2 is sufficient to shift the selectivity from no diffusion limitations to maximum diffusion limitations with strong reduction in conversion. This is what is observed in figures 5.2 and 5.3 when the diffusion time constant is decreased 225 times.

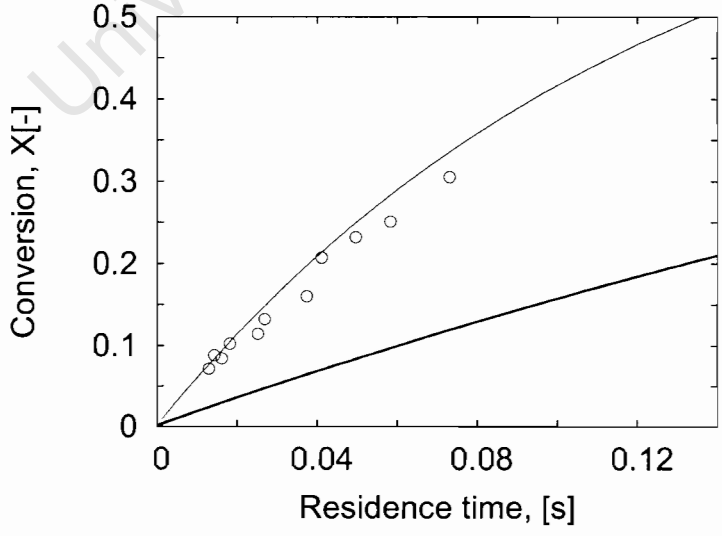

Figure 5.2: pX conversion as a function of residence time. Open symbols - S2300 data; Closed symbols - Q2300 data; Thin line - model predicted data for S150; Thick line - model predicted data for S2300. Model predicted data assumes constant k_{pX} $(6.7s^{-1})$.

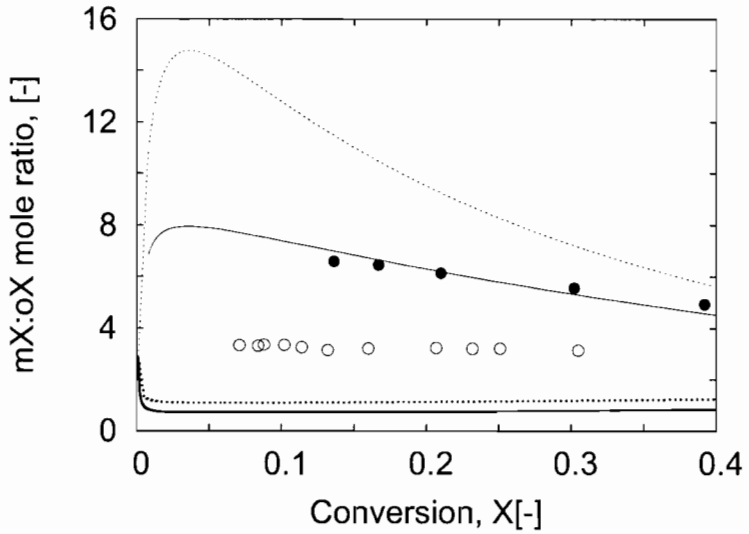

Figure 5.3: mX:oX variation with conversion. Open symbols - S2300 data; Closed symbols - Q2300 data; Thin broken line - model predicted data for Q350; Thick broken line - model predicted data for Q2300; Thin solid line - model predicted data for S150; Thick solid line - model predicted data for S2300. Model predicted data assumes constant k_{pX} ($6.7s^{-1}$ for sand and $2.15s^{-1}$ for quartz).

The reaction rate constants in the model predictions are held constant in keeping with the observations in section 4.2.4. The experimental Thiele moduli show maximum variation of 2.5 (between 0.37 and 0.95, see table 4.5) with increasing film thickness, while a factor of 15 variation in the film thickness indicates that the Thiele modulus should also increase by a factor of 15. As the rate constant is approximately constant with film thickness, the diffusion coefficient must also be varying with film thickness as confirmed by figure 4.21. Results indicate that the observed diffusion limitations are considerably less than expected for the variation in zeolite film thickness.

The Thiele modulus for pX, which is easily and conveniently calculated and used in the discussion represents only an approximation to the diffusion behavior of the pX reaction (table 4.5). For sequential first order reversible reactions there are a number of Thiele moduli like parameters and it is not possible to characterize the effects of diffusion as a single parameter as can be done for single reversible reactions [Aris, 1975]. However, provided that the concentration profile is known, the effectiveness factor can always be estimated irrespective of the reaction kinetics. The oX effectiveness factor, which depends on conversion (figures 5.4 and 5.5), can only be calculated once the model parameters have been estimated and thus represents data which is biased to the model being used. Considering that increased diffusion limitations correspond to higher η_{oX}, the results in figures 5.4 and 5.5 provide the same trends with film thickness and support type as observed in figures 4.16 - 4.19. By keeping the conversion constant, figure 5.6 shows that η_{oX} increases with increasing film thickness signifying larger diffusion limitations. Also the trend between the different supports indicates that the diffusion resistance follows the order $sand > alumina > quartz$ as observed above.

Comparing figure 4.22 to figure 5.6 shows that ϕ_{pX} follows the same behavior with increasing film thickness as is observed for η_{oX}, and thus the ϕ_{pX} provides a convenient analogy to represent

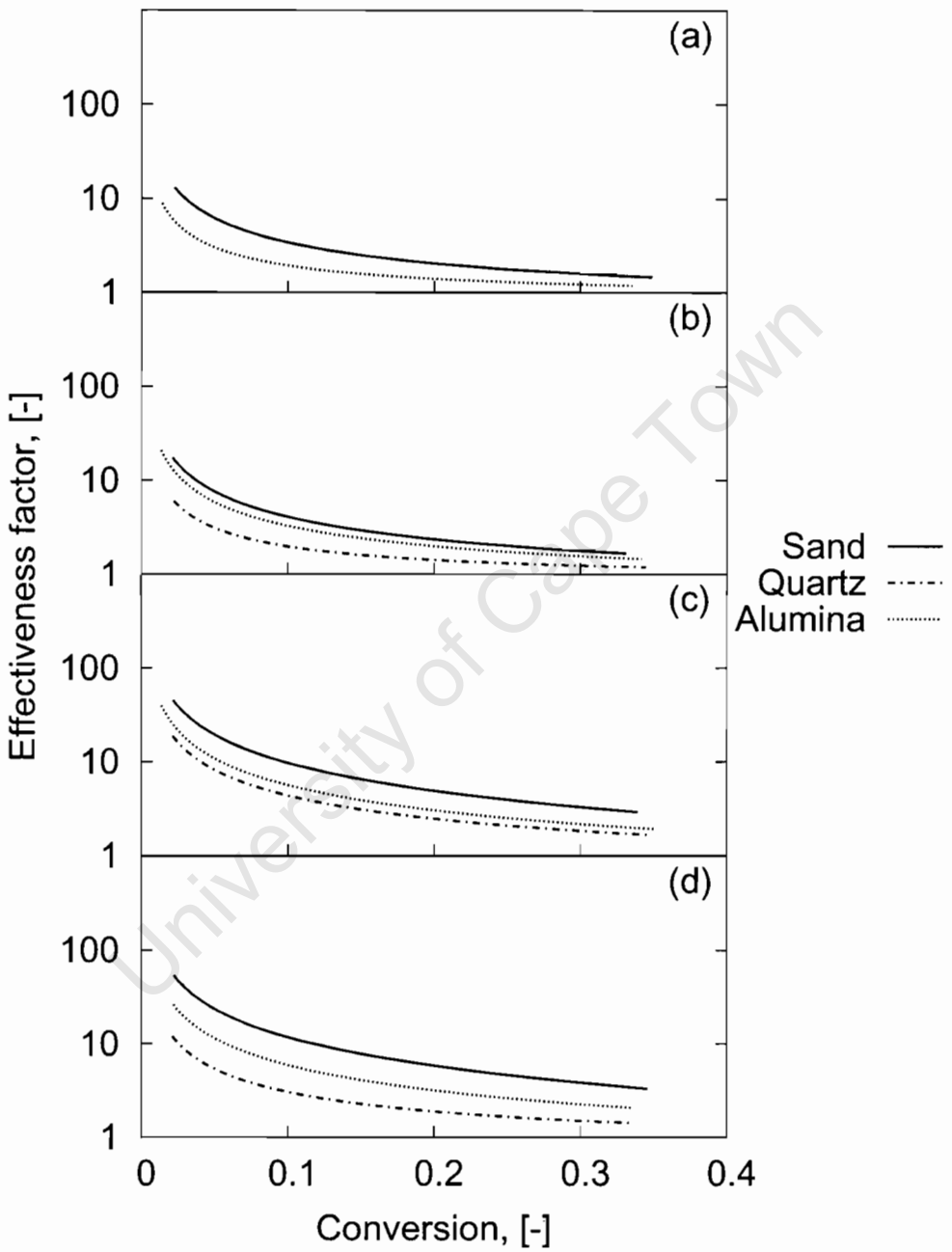

Figure 5.4: oX effectiveness factors as a function of conversion; (a) 150 nm, (b)350 nm, (c)800 nm, (d)2300 nm. The 150nm quartz film was inactive.

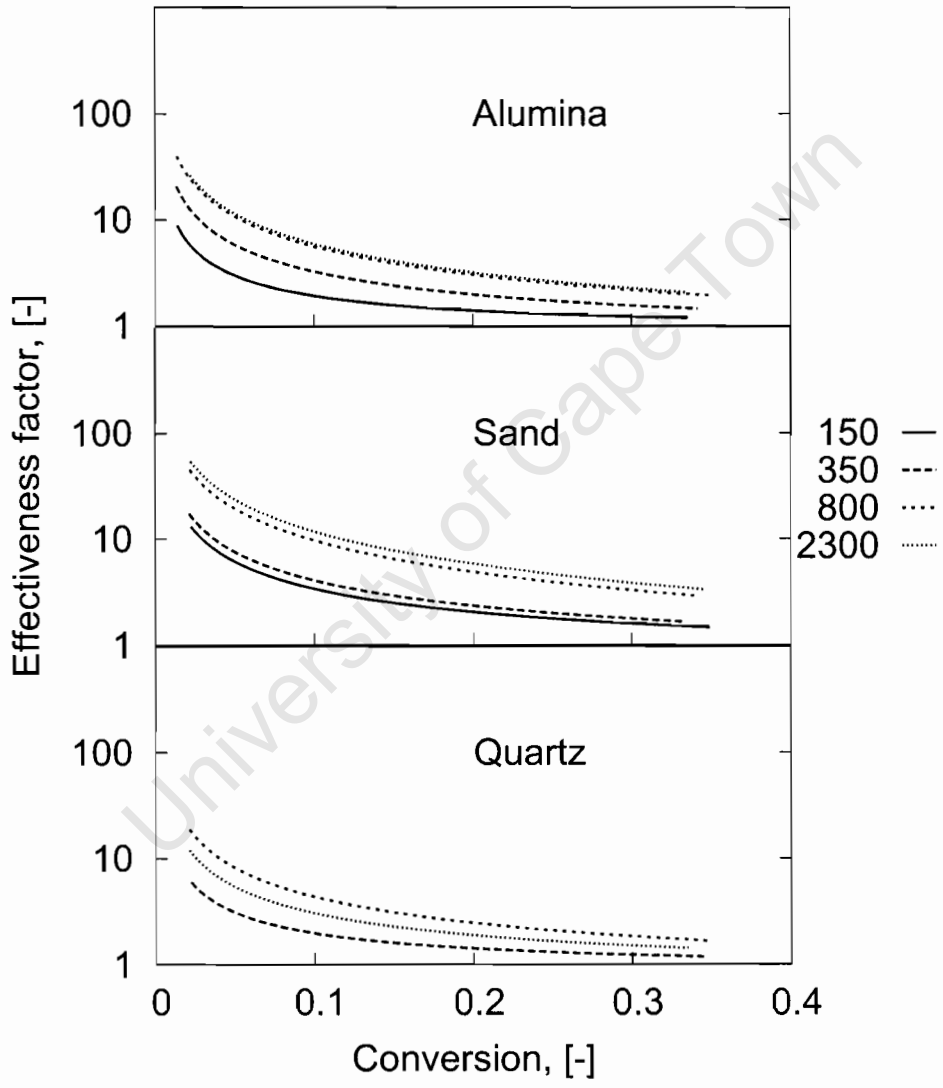

Figure 5.5: oX effectiveness factors as a function of conversion per catalyst. The legend indicates film thickness (in nm). The 150nm quartz film was inactive.

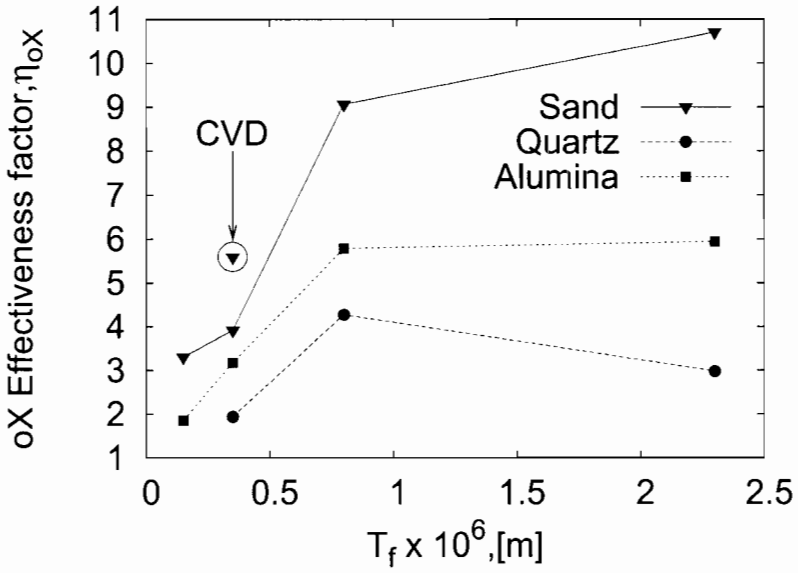

Figure 5.6: oX effectiveness factors as a function of film thickness at $X = 10\%$. The encircled data point represents sample S350 after 15 CVD cycles. The 150nm quartz film was inactive.

the diffusion behavior of the pX reaction system. This analogy functions because all the Thiele moduli are coupled to each other via the assumptions that $k_1 = 2k_2$, $D_{px} : 100D_{oX} : 1000D_{mX}$, and thus ϕ_{pX} represents the response of the complete reaction system.

The diffusion coefficient, like the rate constant, is an intrinsic property of the zeolite structure and for smooth homogeneous films should be constant with increasing film thickness. Figure 4.21 shows that in all cases the diffusivity increases with increasing film thickness which suggests that, although the films are smooth, their structural properties are not homogeneous. These changes are thought to be due to defects and changing of the preferred growth orientation with increasing film thickness [Hedlund, 1998].

Defects can result from cracks formed during the calcination steps or the creation of mis-aligned crystal grain boundaries. Variation in crystal growth direction leads to a change in the channel orientated perpendicular to the surface. The diffusivity in the zig-zag channel is slower than that in the straight channel [Kärger and Ruthven, 1992], and thus the effective diffusivity would appear to change with film thickness. These results suggest that the straight channels, which have an order of magnitude higher diffusivity [Song and Rees, 2000], are orientated such to provide the main access in thick films. Figure 4.21 indicates that the variation in the diffusion coefficient with film thickness is more than 2 orders of magnitude. Thus the variation in zeolite orientation alone cannot be responsible for the variation of the diffusion coefficients with film thickness.

The defects (*i.e.*, cracks, grain boundaries, *etc.*) can be analyzed by considering the limiting case that the film can be fragmented into cubes with a length equivalent to the film thickness T_f, accessible from 5 sides, the 6th side being attached to the support. Assumed also is that the accessibility to the zeolite is not limited by mass transfer through the cracks. The cube can then

be approximated as a sphere of the same volume *i.e.*, the same volume reactivity. The radius of a sphere representing the cubes will then be $R_{defect} \approx \frac{1}{2}T_f$. The slab geometry ($T_f$) may be converted into spherical geometry when the Thiele modulus remains constant, which yields an equivalent radius $R = 3T_f$. A comparison of R and R_{defect} shows that cracks would reduce the effective pathlength of the zeolite film from T_f to $T_{f,defect} = \frac{1}{6}T_f$.

The model parameters of the zeolite film, k_{pX} and D/T_f^2, estimated from the data using the reactor model, are independent of the film thickness, and thus so is the estimated value of ϕ_{pX}. Consequently, the same ϕ_{pX} will give rise to the same selectivity. Thus keeping ϕ_{pX} and k_{pX} constant means that $D/T_{f,defect}^2$ for the defective film is modified to $36D/T_f^2$. As T_f is measured, this translates into an effective diffusion coefficient that is 36 times larger than the true diffusion coefficient. The observed increase in the diffusivity with film thickness is approximately a factor of 80 (figure 4.21) for the thickest film. It is highly unlikely that any of the synthesized films can have so many defects. Furthermore, although the SEM is not ideally suited, this degree of crack formation was not observed, nor has it been observed for similarly synthesized membranes [Jareman, 2004].

When comparing diffusivities of the different films, alumina has an order of magnitude lower diffusivity than sand which is a factor of 2-3 times lower than the quartz. As this is the same zeolite with the same film thicknesses, and the same growth properties, these should all have the same diffusivities as a function of film thickness. Therefore cracks might contribute to but cannot be responsible for the increase in diffusivity with film thickness.

The quartz supported zeolite is the best approximation of a smooth, uniform film and thus can be assumed to be a reference catalyst. The fact that the sand supported zeolite has a lower diffusivity than the quartz supported one, may be due to the agglomeration of the sand particles during preparation, which lowers the effective diffusion resistance. The alumina sample is more complex.

The diffusivity in the alumina supported zeolite film being more than one order of magnitude lower than the quartz supported one, is difficult to qualitatively explain. These films do not have a uniform path length due to the porous nature of the support (§5.1). Also, the activity of these films is considerably lower due to cation exchange. Na^+ cations would cause a greater resistance to the diffusion of critically sized xylene isomers than H^+ cations. Cation exchange has also been shown to decrease with film thickness (see above). This would lead to a diffusivity that is significantly lower than those of the other supported zeolite films. Additionally, it would increase increase more rapidly with increasing film thickness, because thicker films contain less cations.

To a first approximation, the trends in figure 4.21 are correct as the error bars do not show any overlap, notwithstanding the large variances observed in the estimation of the diffusivity.

It has been shown [Aris, 1975] that under diffusion limitations, when there is an activity profile such that the activity is highest near the surface and lowest in the center (eggshell type catalysts),

then the intermediate product B, in a series reaction, A $\longrightarrow$ B $\longrightarrow$C, is favored. This suggests that, for the alumina film, the selectivity to mX should be enhanced by the activity profile and as a result the observed diffusivity should be increased above that of the other supported zeolites. This activity profile in the alumina supported zeolite films would be steepest for the thickest films and thus these should have the largest decrease in oX yield. The activity profile thus opposes the diffusion decrease suggested by the cation exchange and thus cannot be responsible for the observed trend in the diffusion coefficients.

It is difficult to find diffusion coefficients measured at these high temperatures and even more difficult to find these under reaction conditions. Again consulting previous work of Manstein [2001], the diffusion time constant of toluene was estimated as 300 s^{-1}. However, in the model it was assumed that the diffusivity of toluene and para-xylene were equal. This value is about an order of magnitude lower (3000 - 6000) than estimated in this work for sand and quartz supported zeolite films. Noting that the confidence interval of the diffusion time constant can be quite large and that the work of Manstein [2001] used pelleted samples which might result in a reduction of the effective diffusion coefficient, the agreement can be considered reasonable.

The absolute magnitude of the diffusion coefficients obtained under reaction conditions are within an order of magnitude of those extrapolated from table 1.1, and is within the current available accuracy of zeolitic diffusion coefficients.

5.3 Chemical vapor deposition (CVD) on sand supported zeolites

This technique of external surface modification has been applied previously [Manstein et al., 2001] in order to inertize the external surface and modify the selectivity (via the effective diffusivity) of the catalyst during toluene disproportionation TDP. Practical limitations prevented the carrying out of the TDP reaction the zeolite supported film catalysts. However, as shown in §5.2 and in chapter 3, the xylene isomerization reaction responds effectively to changes in diffusion limitations. The discussion addresses the observed response of S350 to 15 cycles of CVD.

5.3.1 Deposition of Silica

The deposition of silica on the external surface follows a linear trend as previously observed [Röger et al., 2001; Manstein, 2001], indicating that the amount of silica deposited per cycle is approximately constant. The amount of silica deposited over 15 cycles (70 Si/nm^2) is considerably higher than that deposited over ZSM5 powder (25 Si/nm^2, [Manstein et al., 2002]) even though less surface area per mass of zeolite was exposed. Previous work [Manstein et al., 2002] has shown that too high deposition of silica can lead to rapid deactivation of the catalyst. It has been observed that the Si deposition per cycle decreases with cycle number over the first few cycles before remaining constant [Manstein et al., 2002]. The lower TEOS conversions obtained

in this work do not show this behavior, and the deposition per cycle was approximately constant (figure 4.25).

5.3.2 Activity of the external surface

The TIPB activity, as represented by the ratio of the first order rate constant, decreases exponential with cycle number (see figure 4.26) [Röger et al., 2001; Manstein et al., 2002]. A similar decrease in activity is observed as a function of silica loading (figure 4.27), but the trend is not as clear as the relationship with cycle number.

The value of $\alpha = 0.91$ based on silica loading obtained in this work is considerably higher than observed by other researchers (table 5.2), indicating that the efficiency of the deposition is low (*i.e.*, only 9% of the activity is reduced per Si/nm^2 deposited).

Table 5.2: Deactivation constants α for the respective temperature series for 1,3,5-TiPB-cracking. Adapted from Manstein [2001].

CVD-series	α	R^2
50	0.75	0.95
100	0.83	0.90
150	0.61	0.79
200	0.63	0.75
300	0.77	0.90
400	0.90	0.81
Pe100°C	0.76	0.96
Pe200°C	0.61	0.99
100°C (This work)	0.91	0.93
100°C [Röger, 1998] [a]	0.57	0.99
320°C [Hibino et al., 1991] [b]	0.97	0.94

[a] TEOS in flow-through system; assuming the uniform deposition of 1.39 Si/nm^2 per CVD cycle at 100°C).
[b] TMOS modification in static vacuum system.

Considering the low catalyst loading, the additional surface area available for silica deposition provided by the inert reaction packing competes with the deposition of silica on the catalyst surface. Thus all of the calculated amount of silica deposited does not deposit on the zeolite. Therefore the amount deposited on the film might well be lower than the observed. However, the amount of silica deposited on the inert packing would be proportional to the total amount deposited, subsequently reducing the amount deposited on the zeolite but not changing the deactivation observed.

If a proportional amount $\beta < 1$ of the total Si deposited is deposited on the zeolite, then the value of α is modified to (equation 5.1):

$$\alpha_{zeolite} = \alpha_{total}^{\frac{1}{\beta}} \tag{5.1}$$

Thus the value of α is reduced and is more comparable with expected literature values (e.g for $\beta = 0.3$, $\alpha = 0.76$). This does not improve the quality of the trend of the deactivation with silica

loading. Increased scatter in the data is a result of the difficulty of estimating the loading of silica from breakthrough experiments, in particular when the TEOS conversion is small, leading to scatter in the Si loading and hence a poor correlation with loading.

5.3.3 Activity and selectivity of the zeolite film

Results show that CVD decreases the activity (figures 4.28 and 4.29) of the sand supported zeolite film without any significant increase in the diffusion limitations (figure 4.30-4.32). Model analysis shows that the diffusivity (figure 4.34) decreases faster than the rate constant (figure 4.33) with increasing silica loading which results in a small increase in the Thiele modulus (figure 4.30). However, this difference in behavior is not enough to justify any significant selectivity changes due to CVD.

In contrast to this work, previous work [Manstein, 2001] has shown that the internal activity remains unaffected during CVD of ZSM-5 pellets when using toluene disproportionation as a probe reaction. Analysing the deactivation as a function of silica loading shows that the activity of the internal surface (k_{pX}) has an $\alpha_{k_{pX}}$ value of 0.98 compared to the activity of the external surface (k_{TiPB}) with an α_{TIPB} value of 0.91. This shows that the decrease in activity per Si/nm^2 loaded is 5 times lower for the internal surface than the external surface. The diffusion coefficient also decreases with an $\alpha_{D_{pX}}$ value of 0.97, although the decrease was expected to follow α_{TIPB} for an external surface area pore blockage model [Manstein, 2001].

Initial deactivation of the external surface may be ascribed to the deactivation of the surface activity, which, for supported films, contribute only a few percent to the overall activity of the xylene isomerization due to the low external surface area. However, continued deactivation with increasing silica loading suggests that bulk blockage of active sites must be occurring. This leads to the situation in which reduced activity but the same selectivity are obtained with the same total catalyst mass. If the model parameters were to be adjusted for the reduction in active catalyst mass according to α_{kpX}, both the intrinsic rate constant and the diffusivity would remain unchanged. This suggests that the CVD process simply blocks the zeolite structure and the active sites with the remaining open structure and sites having no change in activity and diffusivity. Thus CVD on zeolite supported films does not appear as efficient as a technique to enhance selectivity as observed for powdered and pelleted catalysts [Manstein, 2001; Manstein et al., 2002].

Nevertheless, an interesting question remains. How does CVD compete with increasing film thickness? Figure 5.7 shows the simulated behavior of the parent S350 catalyst under conditions of constant D_{pX} or k_{pX} compared to the actual observed variation with CVD. If only the rate constant was changing, then the path indicated by the arrow labelled k_{pX} would have been followed. If only the diffusion coefficient was changing, the path labeled D_{pX} would have been followed. These results show that the catalyst follows an intermediate path in which both the rate constant and diffusion coefficient decrease with increasing silica deposition as indicated by the α evaluations above. However, after 15 CVD cycles, the modified catalyst is is less active

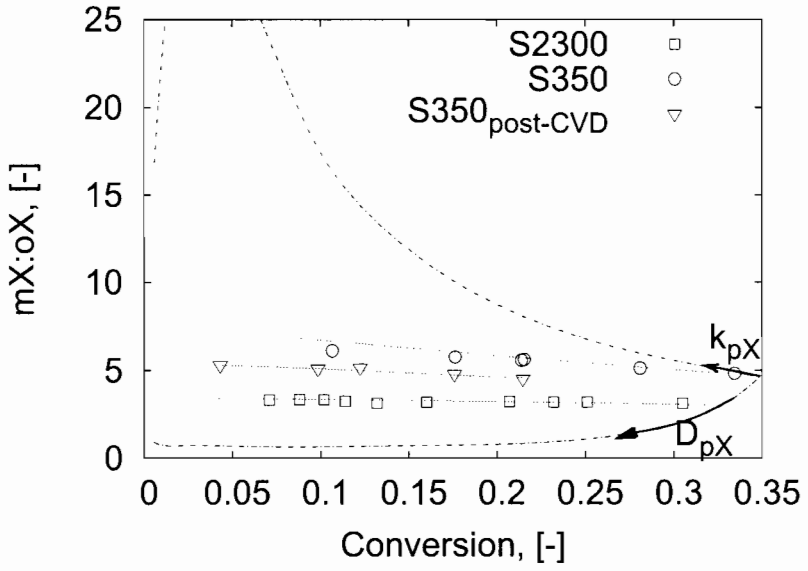

Figure 5.7: mX:oX mole ratio as a function of conversion. The upper dash-dot line represents k_{pX} changes with D_{pX} constant using the model, and the lower one D_{pX} changes with k_{pX} constant (also using the model). Symbols - experimental data; dotted lines - reaction-diffusion model. $S350_{post-CVD}$ is data for the 350 nm film after 15 CVD cycles.

and has less diffusion limitations than the thickest sand supported zeolite film (S2300). This is confirmed by the effectiveness factor (figures 5.6 and 5.8) which is above S350 but remains below S800 and S2300 and for that matter also A800 and A2300. These results indicate that, for zeolites supported on smooth, inert materials, inducing diffusion limitations and increased para-selectivity is more readily obtained by growing thicker films as opposed to CVD.

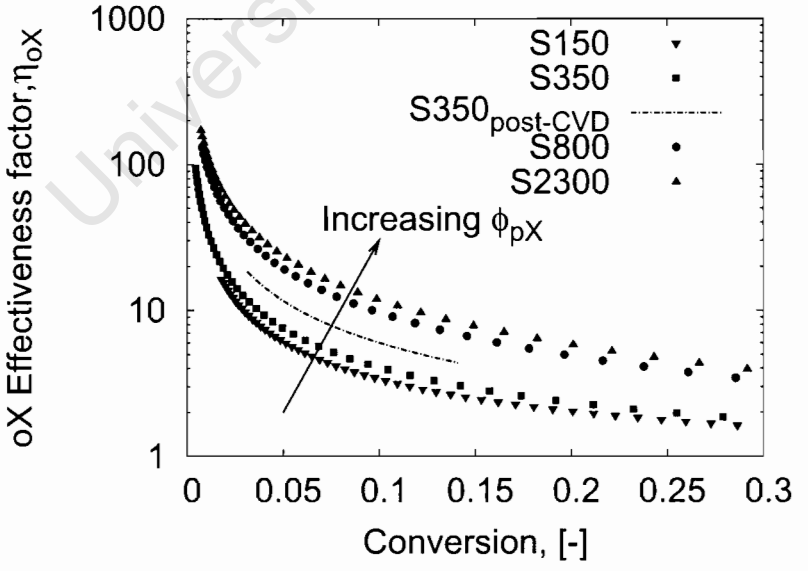

Figure 5.8: oX effectiveness factors on sand catalysts of different thicknesses (in *nm*). The legend indicates film thickness in nm. $S350_{post-CVD}$ is data for the 350 nm film after 15 CVD cycles.

5.4 Implications for commercial applications of zeolite films

This work has shown that increasing the film thickness by a factor of 15 was not able to provide inreased diffusion limitations that would enhance the shape selective properties of the zeolite catalyst for the reactions and conditions of this work. Diffusion limitations were also not large enough so that only the outside layers of a catalyst particle is required for reaction and thus provide justification for the use of thin catalytic films.

Although not investigated, films of the order of 10's of microns are expected to have significant diffusion limitations under conditions used in this work. These zeolite films can be prepared on any irregular structure, provided that it is smooth and inert. Candidates for such procedures are structured distillation packings (meshes and shaped materials) and foils. However, the preparation method is time consuming and expensive. Alternative technologies would be to simply adhere pre-synthesized zeolite crystals to the support or to simply grow crystals on the support using a large excess preparation [Bein, 1996]. The limitations of alternative technologies are that the zeolite crystallite structure is retained and layers might be several 10's of microns thick which might not provide suitable activity and selectivity behavior, but preparation would be cheaper. Thus, should the application justify the expense and if there was a need for very specific activity and selectivity properties, the use of zeolite films could well be justified.

Chapter 6

Conclusions

- Inert smooth supports are needed to obtain smooth zeolite films that are defect free and can be used for efficient catalysis. In this regard, the suitability of the supports for use to make zeolite films follows the order *quartz* > *sand* > *alumina*. However, it should be noted that the sand supports would be as good as the quartz supports if agglomeration during preparation could be avoided. Supports must be free of mobile cations to efficiently support zeolite materials for use as acid catalysts.

- A simple first order reaction-diffusion model provides an excellent description of the behavior of xylene isomerization over supported zeolite catalytic films.

- For ideal smooth films, the intrinsic reactivity of the external and internal surface is independent of film thickness.

- The activity and selectivity did not depend strongly on film thickness.

- Diffusion limitations increase with increasing film thickness, but this increase does not conform to the trend expected from the variation in film thickness *i.e.*, it was not possible to predict all the reaction data for a particular support as a function of film thickness using a single diffusion coefficient. A consequence of this is that the diffusion coefficient varies with film thickness.

- Physical characterization indicates that the films are smooth, homogeneous and uniform. This is in contrast to the estimated intrinsic reaction-diffusion model parameters, which indicate that the films are not homogeneous and uniform.

- These films have not provided model systems to study the influence of diffusion path length on reaction performance. The intrinsic model parameters are in reasonable agreement with those estimated as part of a toluene disproportionation reaction-diffusion model over ZSM-5 catalyst. As a first approximation, diffusion coefficients estimated under reaction conditions are of the same order of magnitude of those extrapolated from literature measured under non-reactive conditions.

- CVD does not provide a means to enhance the selectivity of supported zeolite films and only causes deactivation of the catalyst. For supported zeolite film catalysts, selectivity enhancement is more efficiently achieved by growing thicker films.

Publications

The following publications were generated out of this work:

J. Hedlund, O. Öhrman, V. Msimang, E. van Steen, W. Böhringer, S. Sibiya, K. Möller. The synthesis and testing of thin film ZSM-5 catalysts. Chemical Engineering Science, Volume 59. p2647 - 2657. (2004)

K. P. Möller, J. Hedlund, O. Öhrman, V. Msimang. The catalytic evaluation of structured zeolite catalysts. International Journal of Chemical Reactor Engineering, Volume 2. Article A4, (2004)

O. Öhrman, J. Hedlund, V. Msimang, K. Möller, and J. Sterte. ZSM-5 structured catalysts coated with silicalite-1. Proceedings: 14th International Zeolite Conference 25 . 30 April 2004, Editors: E. van Steen et al.

O. Öhrman, J. Hedlund, V. Msimang, and K. Möller. Thin ZSM-5 film catalysts on quartz and alumina supports. Microporous and Mesoporous Materials. in press. (2004)

Bibliography

Aboul-Gheit, A., Abdel-Hamid, S., and El-Desouki, D. (2001). Catalytic para-xylene maximization IV. hydroisomerization of meta-xylene on catalysts containing platinum on differently steamed H-ZSM-5. *Applied Catalysis A: General*, 209:179–191.

Al-Khattaf, S. and de Lasa, H. (2002). The role of diffusion in alkyl-benzenes catalytic cracking. *Applied Catalysis A: General*, 226:139–153.

Amelse, J. (1993). The influence of diffusion limitations on xylene isomerization. In von Ballmoos, R., Higgins, J., and Treacy, M., editors, *Proceedings of the 9th International Zeolite Conference*, pages 457–464.

Anastas, P., Bartlett, L., Kirchoff, M., and Williamson, T. (2000). The role of catalysis in the design, development, and implementation of green chemistry. *Catalysis Today*, 55:11–22.

Argauer, R. and Landolt, G. (1972). US patent 3,702,886.

Aris, R. (1975). *The mathematical theory of diffusion and reaction in permeable catalysts*, volume 1. Claredon Press.

Au, L. and Yeung, K. (2001). An investigation of the relationship between microstructure and permeation properties of zsm-5 membranes. *Journal of Membrane Science*, 194(1):33–55.

Baba, T., Inoue, Y., and Ono, Y. (1996). Long-range interaction of alkali cations with the acidic OH groups in H-ZSM-5. *Journal of Catalysis*, 159:230–235.

Baiker, A., New, M., and Richarz, W. (1982). Determination of intraparticle diffusion coefficients in catalyst pellets - a comparative study of measuring methods. *Chemical Engineering Science*, 37(4):643–656.

Barrer, R. (1978). *Zeolites and Clay Minerals as Sorbents and Molecular Sieves*. Academic Press, London.

Bauer, F., Dermietzel, J., and Jockisch, W. (1991). Diffusion effects on the kinetics of toluene methylatio and xylene isomerization on HZSM-5 zeolites. In Öhlmann, G., Pfeifer, H., and Fricke, R., editors, *Catalysis and adsorption by zeolites*, volume 65 of *Studies in Surface Science and Catalysis*, pages 305–313. Elsevier Science.

Bein, T. (1996). Synthesis and applications of molecular sieve layers and membranes. *Chemical Materials*, 8:1636–1653.

Benesi, H. and Winquist, B. (1978). Surface acidity of solid catalysts. In Eley, D., Pines, H., and Weisz, P., editors, *Advances in catalysis*, volume 27, pages 97–182. Academic Press.

Bird, R., Stewart, W., and Lightfoot, E. (2002). *Transport Phenomena.* John Wiley and Sons, Inc., 2 edition.

Botes, F. and Böhringer, W. (2004). The addition of HZSM-5 to the FischerTropsch process for improved gasoline production. *Applied Catalysis A: General*, 267(1-2):217–225.

Bowman, R. (2003). Applications of surfactant-modified zeolites to environmental remediation. *Microporous and Mesoporous Materials*, 61(1-3):43–56.

Bozell, J. (2002). Green chemistry in practice. In Clark, J. and Macquarrie, D., editors, *Handbook of Green Chemistry & Technology*, chapter 14, pages 338–365. Blackwell Publishing.

Breck, D. (1974). *Zeolite Molecular Sieves: Structure, Chemistry, and Use.* John Wiley and Sons, New York.

Budd, P., Makhseed, S., Ghanem, B., Msayib, K., Tattershall, C., and McKeown, N. (2004). Microporous polymeric materials. *Materials Today*, 7(4):40–46.

Burton, S., Garbow, K., Hillstrom, J., and More, J. (1980). *MINPACK.* Argonne National Laboratory.

Cannella, W. (1997). Xylenes and Ethylbenzene. In Howe-Grant, M., editor, *Encyclopedia of Chemical Technology*, volume Supplement, pages 831–863. John Wiley and Sons.

Caro, J., Noack, M., Kölsch, P., and Schäfer, R. (2000). Zeolite membranes - state of their development and perspective. *Microporous and Mesoporous Materials*, 38:3–24.

Catana, G., Baetens, D., Mommaerts, T., Schoonheydt, R., and Weckhuysen, B. (2001). Relating structure and chemical composition with Lewis acidity in zeolites: A spectroscopic study with probe molecules. *Journal of Physical Chemistry B*, 105:4904–4911.

Chen, N., Garwood, W., and Dwyer, F. (1996). *Shape selective catalysis in industrial applications.* Marcel Dekker, Inc., 2 edition.

Chen, N., T.F. Degnan, J., and Smith, C. (1994). *Molecular Transport and Reaction in Zeolites.* VCH.

Chen, W.-H., Tsai, T.-C., Jong, S.-J., Zhao, Q., Tsai, C.-T., Wang, I., Lee, H.-K., and Liu, S.-B. (2002). Effects of surface modification on coking, deactivation and para-selectivity of H-ZSM-5 zeolites during ethylbenzene disproportionation. *Journal of Molecular Catalysis A: Chemical*, 181(1-2):41–55.

Chiang, A. S. T. and Chaob, K. (2001). Membranes and films of zeolite and zeolite-like materials. *Journal of Physics and Chemistry of Solids*, 62(9-10):1899–1910.

Chon, H., Lee, K., Park, D., and Ahn, B. J. (1991). Diffusion controlled alkylation of aromatic compounds in cation-exchanged ZSM-5 zeolites. *Bulletin of the Korean Society*, 12(6):625–628.

Choplin, A. (1994). Surface organometallic chemistry on zeolites: A tool for modifying the sorption properties of zeolites. *Journal of Molecular Catalysis*, 86:501–512.

Chu, Y., Keweshan, C., and Vansant, E. (1989). Control of pore-opening size of zeolites. In Karge, H. and Weitkamp, J., editors, *Zeolite as Catalysts, Sorbents and Detergent Builders*, pages 749–758. Elsevier Science.

Chun, Y., Chen, X., Yan, A.-Z., and Xu, Q.-H. (1994). Chemical vapour deposition of TEOS on zeolite HB. In Weitkamp, J., Karge, H., Pfeifer, H., and Hölderich, W., editors, *Zeolites and Related Microporous Materials: State of the Art 1994*, volume 84 of *Studies in Surface Science and Catalysis*, pages 1035–1042. Elsevier Science.

Clark, M. (1996). *Transport modeling for environmental engineers and scientists*. Environmental science and technology. John Wiley and Sons, Inc.

Collins, D., Medina, R., and Davis, B. (1983). Xylene isomerization by ZSM-5 zeolite catalyst. *The Canadian Journal of Chemical Engineering*, 61(1):29–35.

Cundy, C. and Cox, P. (2003). The hydrothermal synthesis of zeolites: History and development from the earliest days to the present time. *Chemical Reviews*, 103(3):663–701.

Cybulski, A. and Moulijn, J. (1998). The present and the future of structured catalysts - an overview. In Cybulski, A. and Moulijn, J., editors, *Structured catalysts and reactors*, volume 71 of *Chemical Industries*. Marcel Dekker, Inc., New York.

Das, J., Bhat, Y., and Halgeri, A. (1994). Selective toluene disproportionation over pore size controlled MFI zeolite. *Industrial & Engineering Chemistry Research*, 33:246–250.

Davis, M. (1991). Zeolites and molecular sieves: not just ordinary catalysts. *Industrial & Engineering Chemistry Research*, 30(8):1675–1683.

Davis, M. (2003). Distinguishing the (almost) indistinguishable. *Science*, 300:438–439.

Davis, M. and Lobo, R. (1992). Zeolite and molecular sieve synthesis. *Chemical Materials*, 4:756–768.

den Exter, M., Jansen, J., van de Graaf, J., Kapteijn, F., Moulijn, J., and van Bekkum, H. (1996). Zeolite-based membranes preparation, performance and prospects. In Chon, H., Woo, S., and Park, S.-E., editors, *Studies in Surface Science and Catalysis*, volume 102 of *Recent Advances and New Horizons in Zeolite Science and Technology*, pages 413–454. Elsevier Science.

Derouane, E. (1998). From shape selective zeolites to zeozymes: Confinement effects in sorption and catalysis by zeolites. In Derouane, E., editor, *A molecular view of heterogeneous catalysis*, Proceedings of the First Francqui Colloquium, pages 5–27. De Boeck Université.

Dewing, J. (1984). Are shape-selective reactions tools for zeolite characterisation? *Journal of Molecular Catalysis*, 27:25–33.

Dixon, A. (2003). Recent research in catalytic inorganic membrane reactors. *International Journal of Chemical Reactor Engineering*, 1(R6). http://www.bepress.com/ijcre/vol1/R6.

Doelle, H.-J., Heering, J., and Riekert, L. (1981). Sorption and catalytic reaction in pentasil zeolites. Influence of preparation and crystal size on equilibria and kinetics. *Journal of Catalysis*, 71:27–40.

Dong, J., Lin, Y., Hu, M. Z., Peascoe, R., and Payzant, E. (2000). Template-removal-associated microstructural development of porous-ceramic-supported MFI zeolite membranes. *Microporous and Mesoporous Materials*, 34:241–253.

Doğu, T. (1998). Diffusion and reaction in catalyst pellets with bidisperse pores size distribution. *Industrial & Engineering Chemistry Research*, 37:2158–2171.

Doyle, A. M., Rupprechtera, G., Pfändera, N., Schlögla, R., Kirschhockb, C. E. A., Martensb, J. A., and Freunda, H. J. (2003). Ultra-thin zeolite films prepared by spin-coating silicalite-1 precursor solutions. *Chemical Physics Letters*, 382(3-4):404–409.

Farcasiu, M. and Degnan, T. (1988). The role of external surface activity in the effectiveness of zeolites. *Industrial & Engineering Chemistry Research*, 27:45–47.

Fuller, E., Ensley, K., and Giddings, J. (1969). Diffusion of halogenated hydrocarbons in helium. The effect of structure on collision cross sections. *The Journal of Physical Chemistry*, 73(11):3679–3685.

Fuller, E., Schettler, P., and Giddings, J. C. (1966). A new method for prediction of binary gas-phase diffusion coefficients. *Industrial & Engineering Chemistry*, 58(5):19–27.

Garcia, S. and Weisz, P. (1990). Effective diffusivities in zeolites: 1. Aromatics in ZSM-5 crystals. *Journal of Catalysis*, 121:294–311.

Garcia, S. and Weisz, P. (1993). Effective diffusivities in zeolites: 2. Experimental appraisal of effective shape-selective diffusivity in ZSM-5 catalysis. *Journal of Catalysis*, 142:691–696.

Gates, B. (1992). *Catalytic Chemistry*. John Wiley and Sons, Inc.

Geus, E. and van Bekkum, H. (1995). Calcination of large MFI-type single crystals, Part 2:Crack formation and thermomechanical properties in view of the preparation of zeolite membranes. *Zeolites*, 15:333–341.

Gierman, H. (1988). Design of laboratory hydroteating reactors scaling down of trickle-flow reactors. *Applied Catalysis*, 43:277–286.

Guisnet, M., Gnep, N., and Morin, S. (2000). Mechanisms of xylene isomerization over acidic solid catalysts. *Microporous and Mesoporous Materials*, 35-36:47–59.

Haag, W. (1994). Catalysis by zeolites - science and technology. In Weitkamp, J., Karge, H., Pfeifer, H., and Hölderich, W., editors, *Zeolites and Related Microporous Materials: State of the Art 1994*, volume 84 of *Studies in Surface Science and Catalysis*, pages 1375–1394. Elsevier Science.

Haag, W. and Chen, N. (1987). Catalyst design with zeolites. In Hegedus, L., editor, *Catalyst design - Progress and Perspectives*, chapter 6, pages 163–212. John Wiley and Sons.

Haag, W., Lago, R., and Weisz, P. (1982). Transport and reactivity of hydrocarbon molecules in a shape-selective zeolite. *Faraday Discussions of the Chemical Society*, 72:317–330.

Hedlund, J. (1998). *Thin films of molecular sieves.* PhD thesis, Luleä University of Technology.

Hedlund, J., Mintova, S., and Sterte, J. (1999a). Controlling the preferred orientation in silicalite films synthesized by seeding. *Microporous and Mesoporous Materials*, 28:185–194.

Hedlund, J., Noack, M., Kölsch, P., Creaser, D., and Sterte, J. (1999b). ZSM-5 membranes synthesized without organic templates using a seeding technique. *Journal of Membrane Science*, 159:263–273.

Hedlund, J., Schoeman, B., and Sterte, J. (1997). Synthesis of ultrathin films of molecular sieves by the seed film method. In Chon, H., Ihm, S.-K., and Uh, Y., editors, *Progress in Zeolites and Microporous Materials*, volume 105 of *Studies in Surface Science and Catalysis*, pages 2203–2210. Elsevier Science.

Heering, J., Kotter, M., and Reikert, L. (1982). Diffusion and catalytic reaction in zeolite ZSM-5. *Chemical Engineering Science*, 37(4):581–584.

Hibino, T., Niwa, M., and Murakami, Y. (1991). Shape-selectivity over HZSM-5 modified by chemical vapor deposition of silicon alkoxide. *Journal of Catalysis*, 128:551–558.

Hibino, T., Niwa, M., and Murakami, Y. (1993). Inactivation of external surface of modernite and ZSM-5 by chemical vapor deposition of silicon alkoxide. *Zeolites*, 13:518–523.

Hougen, O. and Watson, K. (1943). Solid catalysts and reaction rates. *Industrial & Engineering Chemistry*, 35(5):529–541.

Impens, N., van der Voort, P., and Vansant, E. (1999). Silylation of micro-, meso- and non-porous oxides: a review. *Microporous and Mesoporous Materials*, 28:217–232.

Jansen, J., Koegler, J., van Bekkum, H., Calis, H., van den Bleek, C., Kapteijn, F., Moulijn, J., Geus, E., and van der Puil, N. (1998). Zeolitic coatings and their potential use in catalysis. *Microporous and Mesoporous Materials*, 21:213–226.

Jareman, F. (2004). *Properties and modeling of MFI membranes.* PhD thesis, Luleä University of Technology.

Kärger, J. and Ruthven, D. (1992). *Diffusion in Zeoliltes and Other Microporous Solids.* John Wiley and Sons.

Keil, F. (1996). Modelling of phenomena within catalyst particles. *Chemical Engineering Science*, 51(10):1543–1567.

Keipert, O. and Baerns, M. (1998). Determination of the intracrystalline diffusion coefficients of alkanes in H-ZSM-5 zeolite by a transient technique using the temporal-analysis-of-products (TAP) reactor. *Chemical Engineering Science*, 53(20):3623–3634.

Klemm, E. and Emig, G. (1997). A method for the determination of diffusion coefficients in product-shape-selective catalysis on zeolites under reaction conditions. *Chemical Engineering Science*, 52(23):4329–4344.

Koriabkina, A., de Jong, A., Schuring, D., van Grondelle, J., and van Santen, R. (2002). Influence of the acid sites on the intracrystalline diffusion of hexanes and their mixtures within MFI-Zeolites. *Journal of Physical Chemistry B*, 106:9559–9566.

Lai, Z., Bonilla, G., Diaz, I., Nery, J., Sujaoti, K., Amat, M., Kokkoli, E., Terasaki, O., Thomson, R., Tsapatsis, M., and Vlachos, D. (2003). Microstructural optimization of a zeolite membrane for organic vapor separation. *Science*, 300:456–460.

Lanewala, M. and Bolton, A. (1969). The isomerization of the xylenes using zeolite catalysts. *The Journal of Organic Chemistry*, 34(10):3107–3112.

Lassinantti, M., Hedlund, J., and Sterte, J. (2000). Faujasite-type films synthesized by seeding. *Microporous and Mesoporous Materials*, 38(1):25–34.

Li, Q., Hedlund, J., Creaser, D., and Sterte, J. (2001). Zoned MFI films by seeding. *Chemical Communications*, 7:527–528.

Li, Y., Chang, X., and Zeng, Z. (1992). Kinetics study of the isomerization of xylene on HZSM-5 zeolite. 1. Kinetics model and reaction mechanism. *Industrial & Engineering Chemistry Research*, 31:187–192.

Llopis, F., Sastre, G., and Corma, A. (2004). Xylene isomerization and aromatic alkylation in zeolites NU-87,SSZ-33, β, and ZSM-5: molecular dynamics and catalytic studies. *Journal of Catalysis*, 227:227–241.

Mahgoub, K. and Al-Khattaf, S. (2004). Catalytic cracking of hydrocarbons in a riser simulator: The effect of catalyst accessibility and acidity. *Energy & Fuels*.

Manstein, H. (2001). *The chemical vapour deposition of tetraethoxysilane on zeolite ZSM-5*. PhD thesis, University of Cape Town.

Manstein, H., Möller, K., and O'Connor, C. (2001). Cyclic chemical vapor deposition of TEOS on ZSM-5: Effect of deposition temperature on shape selective performance. In Galarneau, A., Renzo, F. D., Fajula, F., and Vedrine, J., editors, *Zeolites and mesoporous materials at the dawn of the 21st century*, volume 135 of *Studies in Surface Science and Catalysis*. Elsevier Science.

Manstein, H., Möller, K. P., Böhringer, W., and O'Connor, C. T. (2002). Effect of the deposition temperature on the chemical vapour deposition of tetraethoxysilane on zsm-5. *Microporous and Mesoporous Materials*, 51:35–42.

Martens, J., Perez-Pariente, J., Sastre, E., and Corma, A. (1988). Isomerization and disproportionation of m-xylene selectivities induced by the void structure of the zeolite framework. *Applied Catalysis*, 45:85–101.

Masuda, T., Fujikata, Y., Ikeda, H., and Hashimoto, K. (2000). Diffusivities in the binary components system within MFI-type zeolite crystals. *Microporous and Mesoporous Materials*, 38:323–332.

Masuda, T., Fujikata, Y., Nishida, T., and Hashimoto, K. (1998). The influence of acid sites on intracrystalline diffusivities within MFI-type zeolites. *Microporous and Mesoporous Materials*, 23:157–167.

Mears, D. (1971). The role of axial dispersion in trickle-flow laboratory reactors. *Chemical Engineering Science*, 26:1361–1366.

Mintova, S., Hedlund, J., Valtchev, V., Schoeman, B., and Sterte, J. (1997). Preparation of ZSM-5 films from template free precursors. *Journal of Materials Chemistry*, 7(12):2341–2342.

Mintova, S., Hedlund, J., Valtchev, V., Schoeman, B., and Sterte, J. (1998). ZSM-5 films prepared from template free precursors. *Journal of Materials Chemistry*, 8(10):2217–2221.

Mirth, G., Čejka, J., and Lercher, J. (1993). Transport and isomerizaton of xylenes over HZSM-5 zeolites. *Journal of Catalysis*, 139:24–33.

Miyauchi, T. (1971). Film coefficients of mass transfer of dilute sphere-packed beds in low flow rate regime. *Journal of Chemical Engineering of Japan*, 4(3):238–245.

Moulijn, J., Tarfaoui, A., and Kapteijn, F. (1991). General aspects of catalyst testing. *Catalysis Today*, 11:1–12.

Nair, S., Lai, Z., Nikolakis, V., Xomeritakis, G., Bonilla, G., and Tsapatsis, M. (2001). Separation of close-boiling hydrocarbon mixtures by MFI and FAU membranes made by secondary growth. *Microporous and Mesoporous Materials*, 48:219–228.

Nakazawa, T., Sadakata, M., and Okubo, T. (1998). Early stages of MFI film formation. *Microporous and Mesoporous Materials*, 21:325–332.

Namba, S., Inaka, A., and Yashima, T. (1986a). Effect of selective removal of aluminium from external surfaces of HZSM-5 zeolite on shape selectivity. *Zeolites*, 6:107–110.

Namba, S., Inaka, A., and Yashima, T. (1986b). Effect of selective removal of aluminium from external surfaces of HZSM-5 zeolite on shape selectivity. *Zeolites*, 6:107–110.

Nijhuis, T., van den Broeke, L., Linders, M., van de Graaf, J., Kapteijn, F., Makkee, M., and Moulijn, J. (1999a). Measurement and modeling of the transient adsorption, desorption and diffusion processes in microporous materials. *Chemical Engineering Science*, 54:4423–4436.

Nijhuis, T., van den Broeke, L., Linders, M., van de Graaf, J., Kapteijn, F., Makkee, M., and Moulijn, J. (1999b). Modeling of the transient sorption and diffusion processes in microporous materials at low pressure. *Catalysis Today*, 53:189–205.

Nishiyama, N., Ueyama, K., and Matsukata, M. (1995). Synthesis of defect-free zeolite-alumina composite membranes by a vapor-phase transport method. *Microporous Materials*, 7:299–308.

Niwa, M., Kato, S., Hattori, T., and Murakami, Y. (1984). Fine control of the pore-opening size of the zeolite mordenite by chemical vapour deposition of silicon alkoxide. *Journal of the Chemical Society, Faraday Transactions I*, 80:3135–3145.

Öhrman, O., Nordgren, U., Hedlund, J., Creaser, D., and Sterte, J. (2001). Structured zeolite ZSM-5 coatings on ceramic packing materials. In Galarneau, A., Renzo, F. D., Fajula, F., and Vedrine, J., editors, *Zeolites and mesoporous materials at the dawn of the 21st century*, volume 135 of *Studies in Surface Science and Catalysis*, page 20. Elsevier Science.

Olson, D. and Haag, W. (1984). Structure-selectivity relationship in xylene isomerization and selective toluene disproportionation. In Jr, T. W., Betta, R., Derouane, E., and Baker, R., editors, *Catalytic Materials: Relationship Between Structure and Reactivity*, volume 248 of *ACS Symposium Series*, pages 275–307. American Chemical Society, Washington, DC.

Olson, D., Kokotailo, G., and Lawton, S. (1981). Crystal structure and structure-related properties of ZSM-5. *Journal of Physical Chemistry*, 85(15):2238–2243.

Palekar, M. and Rajadhyaksha, R. (1986). Sorption accompanied by chemical reaction in zeolites. *Catalysis Reviews - Science and Engineering*, 28(4):371–429.

Paschek, D. and Krishna, R. (2001). Inter-relation between self- and jump-diffusivities in zeolites. *Chemical Physics Letters*, 333:278–284.

Perry, R., Green, W. D., and Maloney, J. (1984). *Perry's Chemical Engineers' Handbook*. McGraw-Hill, 6 edition.

Petropoulos, J., Petrou, J., and Liapis, A. (1991). Network model investigation of gas transport in bidisperse porous adsorbents. *Industrial & Engineering Chemistry Research*, 30:1281–1289.

Post, M. (1991). Diffusion in zeolite molecular sieves. In van Bekkum, H., Flanigen, E., and Jansen, J., editors, *Introduction to zeolite science and practice*, volume 58 of *Studies in Surface Science and Catalysis*, pages 391–443. Elsevier Science.

Rabo, J. and Schoonover, M. (2001). Early discoveries in zeolite chemistry and catalysis at Union Carbide, and follow-up in industrial catalysis. *Applied Catalysis A: General*, 222(1-2):261–275.

Ratnasamy, P., Babu, G., Chandwadkar, A., and Kulkarni, S. (1986). Influence of crystal size of HZSM-5 on activity and shape selectivity in xylene isomerization. *Zeolites*, 6:98–100.

Resnick, W. and Golt, M. (1981). Particle-to-gas mass-transfer measurements and coefficients in fixed beds at low Reynolds numbers. *International Journal of Heat and Mass Transfer*, 24:387–394.

Rexwinkel, G., Heesink, A., and Swaaij, W. (1997). Mass transfer in packed beds at low Peclet numbers-wrong experiments or wrong interpretations? *Chemical Engineering Science*, 52(21-22):3995–4003.

Rice, R. and Do, D. (1995). *Applied Mathematics and Modeling for Chemical Engineers.* John Wiley and Sons.

Röger, H. (1998). *Application of the transformation of 1,2,4-Trimethylbenzene to monitor the chemical vapour deposition of tetraethoxysilane over ZSM-5.* PhD thesis, University of Cape Town.

Röger, H., Krämer, M., Möller, K., and O'Connor, C. (1998). Effects of in-situ chemical vapour deposition using tetraethoxysilane on the catalytic and sorption properties of zsm-5. *Microporous and Mesoporous Materials*, 21:607–614.

Röger, H., Manstein, H., Böhringer, W., Möller, K., and O'Connor, C. (2001). Unravelled from the back: kinetics of alkoxysilane CVD on zeolites and evidence for pore mouth plugging determined from model conversion over stepwise silanised samples. In Renzo, F. D., Fajula, F., Vedrine, J., and Galarneau, A., editors, *Zeolites and Mesoporous Materials at the Dawn of the 21st Century*, volume 135 of *Studies in Surface Science and Catalysis.* IZC, Elsevier Science.

Saracco, G., Neomagus, H. W. J. P., Versteeg, G. F., and van Swaaij, W. P. M. (1999). High-temperature membrane reactors: potential and problems. *Chemical Engineering Science*, 54(13-14):1997–2017.

Satterfield, C. (1969). *Mass transfer in heterogeneous catalysis.* M.I.T. Press.

Schuring, D. (2002). *Diffusion in Zeolites: Towards a Microscopic Understanding.* PhD thesis, Eindhoven University of Technology, The Netherlands.

Schwan, P. and Möller, K. (2003). Estimation of cumene cracking reaction-diffusion model parameters: Uniqueness and parametric sensitivity analysis. *International Journal of Chemical Reactor Engineering*, 1(A16).

Sokol, A., Richard, C., Catlow, A., Garcés, J., and Kuperman, A. (2000). Computational investigation into the origins of Lewis acidity in zeolites. *Advanced Materials*, 12(23):1801–1805.

Song, L. and Rees, L. (2000). Adsorption and diffusion of cyclic hydrocarbon in MFI-type zeolites studied by gravimetric and frequency-response techniques. *Microporous and Mesoporous Materials*, 35-36:301–314.

Sterte, J., Hedlund, J., D.Creaser, Öhrman, O., Zheng, W., and Lassinantti, M. (2001). Application of the seed-film method for the preparation of structured molecular sieve catalysts. *Catalysis Today*, 69:323–329.

Stewart, W. and Caracotsios, M. (1996). *GREGPAK*. Stewart and Associates Engineering Software Inc., Madison, Wisconsin, USA.

Stone, F. (2003). Research perspectives during 40 years of the Journal of Catalysis. *Journal of Catalysis*, 217:2–11.

Sun, Y., Han, Y., Yuan, L., Ma, S., Jiang, D., and Xiao, F.-S. (2003). Microporosity in ordered mesoporous aluminosilicates characterized by catalytic probing reactions. *Journal of Physical Chemistry B*, 107:1853–1857.

Szostak, R. (1991). Modified zeolites. In van Bekkum, H., Flanigen, E., and Jansen, J., editors, *Introduction to zeolite science and practice*, volume 58 of *Studies in Surface Science and Catalysis*, chapter 5, pages 153–199. Elsevier Science.

Szostak, R. (1992). *Handbook of Molecular Sieves*. Van Nostrand Reinhold, New York.

Tavolaro, A. and Drioli, E. (1999). Zeolite membranes. *Advanced Materials*, 11(12):975–996.

Thiele, E. (1939). Relation between catalytic activity and size of particle. *Industrial & Engineering Chemistry*, 31(7):916–920.

Tsai, T.-C., Liu, S.-B., and Wang, I. (1999). Disproportionation and transalkylation of alkylbenzenes over zeolite catalysts. *Applied Catalysis A: General*, 181:355–398.

Tynjälä, P. and Pakkanen, T. (1997). Shape selectivity of ZSM-5 zeolite modified with chemical vapor deposition of silicon and germanium alkoxides. *Journal of Molecular Catalysis A: Chemical*, 122:159–168.

van Bekkum, H., Geus, E., and Kouwenhoven, H. (1994). Supported zeolite systems and applications. In Jansen, J., Stöcker, M., Karge, H., and Weitkamp, J., editors, *Advanced Zeolite Science and Applications*, volume 85 of *Studies in Surface Science and Catalysis*. Elsevier Science.

van der Puil, N., Dautzenberg, F., van Bekkum, H., and Jansen, J. (1999). Preparation and catalytic testing of zeolite coatings on preshaped alumina supports. *Microporous and Mesoporous Materials*, 27:95–106.

Vansant, E. (1997). Molecular engineering of oxides and zeolites. *Journal of Molecular Catalysis A: Chemical*, 115:379–387.

Čejka, J., Žilková, N., Wichterlová, B., Eder-Mirth, G., and Lercher, J. (1996). Decisive role of transport rate of products for zeolite para-selectivity: Effect of coke deposition and external surface silylation on activity and selectivity of HZSM-5 in alkylation of toluene. *Zeolites*, 17:265–271.

Čejka, J. and Wichterlová, B. (2002). Acid-catalyzed synthesis of mono- and dialkyl benzenes over zeolites: Active sites, zeolite topology, and reaction mechanisms. *Catalysis Reviews*, 44(3):375–421.

Venuto, P. (1994). Organic catalysis over zeolites: a perspective on reaction paths within micropores. *Microporous and Mesoporous Materials*, 2:297–411.

Villadsen, J. and Michelsen, M. (1978). *Solution of Differential Equation Models by Polynomial Approximation.* Prentice-Hall international series in the physical and chemical engineering sciences. Prentice-Hall.

Vroon, Z., Keizer, K., Burggraaf, A., and Verweij, H. (1998). Preparation and characterization of thin zeolite MFI membranes on porous supports. *Journal of Membrane Science*, 144:65–76.

Wang, Z., Hedlund, J., and Sterte, J. (2002). Synthesis of thin silicalite-1 films on steel supports using a seeding method. *Microporous and Mesoporous Materials*, 52:191–197.

Weber, R., Möller, K., and O'Connor, C. (2000). The chemical vapour and liquid deposition of tetraethoxysilane on ZSM-5, mordenite and beta. *Microporous and Mesoporous Materials*, 35-36:533–543.

Wegner, K., Dong, J., and Lin, Y. (1999). Polycrystalline MFI zeolite membranes: Xylene pervaporation and its implication on membrane microstructure. *Journal of Membrane Science*, 158:17–27.

Wei, J. (1962a). Intraparticle diffusion effects in complex systems of first order reactions: 1. The effects in single particles. *Journal of Catalysis*, 1:526–537.

Wei, J. (1962b). Intraparticle diffusion effects in complex systems of first order reactions: Ii. The influence of diffusion on the performance of chemical reactors. *Journal of Catalysis*, 1:538–546.

Wei, J. (1982). A mathematical theory of enhanced para-xylene selectivity in molecular sieve catalysts. *Journal of Catalysis*, 76:433–439.

Wei, J. and Prater, C. (1962). The structure and analysis of complex reaction systems. *Advances in Catalysis*, 13:203–392.

Weisz, P. (1973). Zeolites - New horizons in catalysis. *CHEMTECH*, pages 498–505.

Weisz, P. (1980). Molecular shape selective catalysis. *Pure and Applied Chemistry*, 52:2091–2103.

Weisz, P. (2000). Some classical problems of catalytic science: resolution and implications. *Microporous and Mesoporous Materials*, 35-36:1–9.

Weisz, P. and Prater, C. (1954). Interpretation of measurements in experimental catalysis. *Advances in Catalysis*, 6:143–196.

Weisz, P. and Swegler, E. (1955). Effect of intra-particle diffusion on the kinetics of catalytic dehydrogenation of cyclohexane. *Journal of Physical Chemistry*, 59:823–826.

Weitkamp, J. (2000). Zeolites and catalysis. *Solid State Ionics*, 131:175–188.

Weitkamp, J. and Ernst, S. (1994). Catalytic test reactions for probing the pore width of large and super-large pore molecular sieves. *Catalysis Today*, 19:107–150.

Wheeler, A. (1951). Reaction rates and selectivity in catalyst pores. *Advances in Catalysis*, 3:249–327.

Wong, W., Au, L., Ariso, C., and Yeung, K. (2001a). Effects of synthesis parameters on the zeolite membrane growth. *Journal of Membrane Science*, 191:143–163.

Wong, W., Au, L., Lau, P., Ariso, C., and Yeung, K. (2001b). Effects of synthesis parameters on the zeolite membrane morphology. *Journal of Membrane Science*, 193:141–161.

Wu, P., Takayuki, K., and Tatsuaki, Y. (1998). Selective formation of p-xylene with disproportionation of toluene over MCM-22 catalysts. *Microporous and Mesoporous Materials*, 22(1-3):343–356.

Yan, Y., Davis, M., and Gavalas, G. (1997). Preparation of highly selective zeolite ZSM-5 membranes by a post-synthetic coking treatment. *Journal of Membrane Science*, 123:95–103.

Yue, Y.-H., Tang, Y., and Gao, Z. (1997). Zeolite pore size engineering by chemical liquid deposition. In Chon, H., Ihm, S.-K., and Uh, Y., editors, *Progress in Zeolites and Microporous Materials*, volume 105 of *Studies in Surface Science and Catalysis*, pages 2059–2065. Elsevier Science.

Ziolek, M. (2004). Catalytic liquid-phase oxidation in heterogeneous system as green chemistry goal - advantages and disadvantages of MCM-41 used as catalyst. *Catalysis Today*, 90:145–150.

Appendix A

Calculations

A.1 Linear velocity, u

At reaction conditions in an empty reactor, u is:

$$u = \frac{\dot{n}RT}{p\frac{\pi}{4}(d^2_{reactor} - d^2_{thermowell})} \tag{A.1}$$

A.1.1 Further Reaction Conditions

All reactions were performed at 450^oC and atmospheric pressure. At these conditions, the density of Argon ρ (g/m^3) is 674. Its viscosity $\mu_{Ar,450^oC}$ (cP) is [Perry et al., 1984] 0.0436. The linear velocity u (cm/s) ranged between 0.234 and 1.87. The rest of the reaction conditions are given in tables 2.3, 2.4, and 2.5.

A.2 Film diffusion

Alluded to in §1.2 and discussed extensively elsewhere [Miyauchi, 1971; Resnick and Golt, 1981; Rexwinkel et al., 1997; Bird et al., 2002; Clark, 1996], gas film diffusion across the stationary layer bordering the zeolite-coated support can be the rate-controlling step in the reaction cycle. To show that this is not the case, it has to be proven that the difference between the surface and bulk concentration of the diffusing species is negligible. Traditionally, this is done with the help of mass transfer correlations, a large number of which have been presented for a range of flow conditions. Here, the correlation (equation A.2) by Bird et al. [2002] was used to estimate the gas film mass transfer coefficient k_f.

$$Sh = 2 + 0.991(ReSc)^{1/3} \tag{A.2}$$

For sand catalysts, the particle Reynolds number $Re_p = \frac{\rho u d_p}{\mu}$ was $0.0054 < Re_p < 0.0433$. For quartz and alumina catalysts ($d_p = 3\ mm$), it was $0.081 < Re_p < 0.641$.

From equation A.3 [Fuller et al., 1966], the binary gas-phase diffusion coefficient D_{AB} (m^2/s) (with A and B representing pX and Ar in this case) is estimated (at 450℃) to be $1.72 \cdot 10^{-5}$.

$$D_{AB} = \frac{1.00 \cdot 10^{-3} T^{1.75} (1/M_A + 1/M_B)^{1/2}}{P[(\sum_v)_A^{1/3} + (\sum_v)_B^{1/3}]^2} \tag{A.3}$$

Here, T (in ^oK) is the temperature, M_A and M_B (in g/mol) the molecular weights of A and B, P (in atm) the pressure, and $\sum_v$ the sum of atomic diffusion volumes given in tables by the same authors [Fuller et al., 1966, 1969].

The Schmidt number $Sc = \frac{\mu}{\rho D_{AB}}$ is 3.8. The Sherwood number (equation A.2), therefore, lies in the range $2.54 < Sh < 3.33$, and since it is also $Sh = \frac{d_p k_f}{D_{AB}}$, the film mass transfer coefficient k_f (m/s) is 0.22 for sand, and 0.02 for the other catalysts.

The concentration of pX at the surface is evaluated by manipulating equation A.4, which represents the concentration drop across a gas film.

$$r_{pX,max} = k_f (c_{pX,b} - c_{pX,s}) \frac{A_z}{V_z} \tag{A.4}$$

Rearranged to make $c_{pX,s}$ the subject of the formula, this equation gives[1] :

$$c_{pX,s} = \frac{c_{pX,b}}{1 + C_o} \tag{A.5}$$

where $C_o = \frac{k_{pX,b} V_z}{k_f A_z}$. For all catalysts tested, this value is insignificant. Equation A.5 is thus reduced to $c_{pX,s} \approx c_{pX,b}$. In other words, film resistance is negligible.

A.3 Plug flow

The plug flow criteria by Chu et al. [1989] was employed to evaluate the flow regime (table A.1).

Table A.1: L/d_p values for all catalysts.

	L/d$_p$		
Tf(nm)	Sand	Alumina	Quartz
150	114	67	-
350	49	67	53
800	49	67	53
2300	16[a]	11[b]	40

[a] 49 for the 3 gram sample
[b] 67 for the 36 gram sample

[1] It is assumed that the consumption of pX follows first order kinetics. This is valid because the maximum reaction rate is obtained at zero conversion.

$$\frac{L}{d_p} > \frac{20n}{Pe_p} ln\left(\frac{1}{1-x}\right) \tag{A.6}$$

The axial dispersion criterion by Mears [1971], Gierman [1988] and Moulijn et al. [1991] is shown in equation A.6, where L is the bed height (given in tables 2.3, 2.4, and 2.5), Pe_p is the particle Peclet number (proposed to be 0.5 for particle Reynolds numbers less than 1 [Gierman, 1988]), n the reaction order number (assumed to be one for both pX isomerization and TIPB cracking), and x the conversion ($x_{pX,max} = 0.4$ and $x_{TIPB,max} = 0.7$). Using these values, the right hand side of equation A.6 is therefore 20 for pX isomerization and 48 for TIPB cracking.

Appendix B

Sketches

Figure B.1: Sketch of reactor.

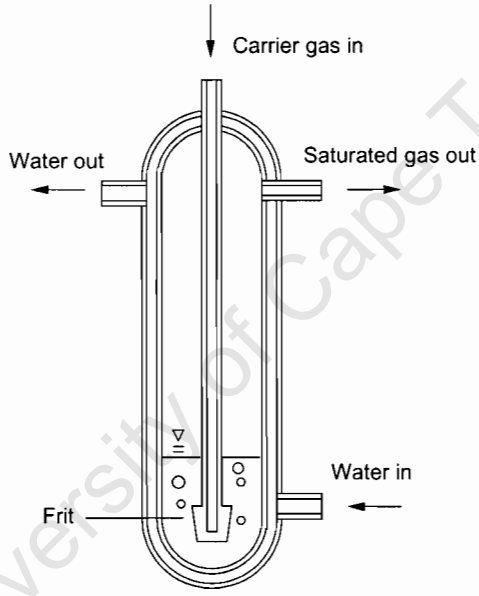

Figure B.2: Sketch of saturator.

Appendix C

BJH

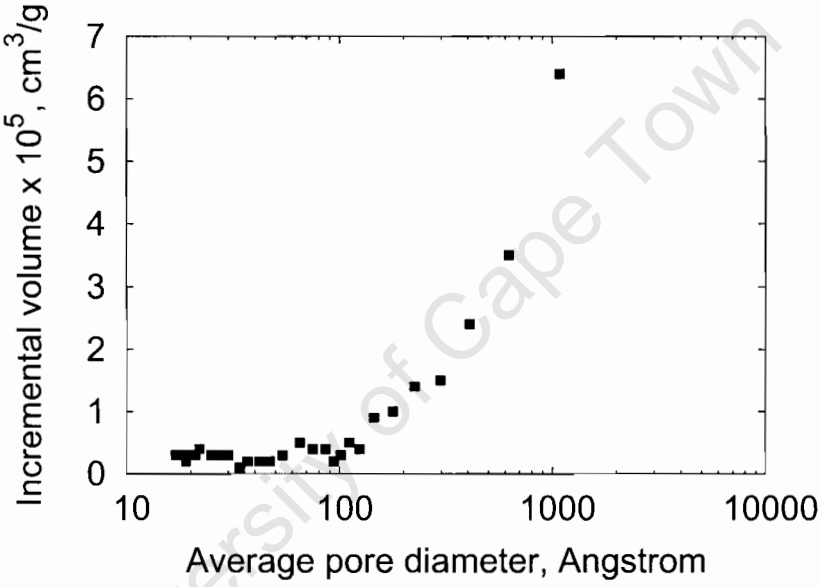

Figure C.1: BJH data showing incremental volume as a function of pore diameter for alumina supports.

Appendix D

Tables

Table D.1: pX data for 7 grams of sample S150

τ(s)	Ypx	Ymx	Yox
8.77E-03	9.24E-01	6.80E-02	8.12E-03
1.20E-02	9.18E-01	7.25E-02	9.30E-03
1.65E-02	9.01E-01	8.73E-02	1.19E-02
2.97E-02	8.47E-01	1.33E-01	2.02E-02
4.07E-02	8.07E-01	1.66E-01	2.71E-02
5.90E-02	7.28E-01	2.32E-01	4.01E-02

Table D.2: pX data for 7.1 grams of sample S150

τ(s)	Ypx	Ymx	Yox
9.19E-03	9.23E-01	6.88E-02	8.50E-03
1.22E-02	9.17E-01	7.28E-02	9.80E-03
2.60E-02	8.48E-01	1.33E-01	1.95E-02
3.70E-02	8.03E-01	1.71E-01	2.67E-02
4.54E-02	7.31E-01	2.31E-01	3.82E-02

Table D.3: pX data for 7.2 grams of sample S350

τ(s)	Ypx	Ymx	Yox
3.83E-02	8.78E-01	1.05E-01	1.69E-02
4.40E-02	8.62E-01	1.18E-01	1.95E-02
5.21E-02	8.44E-01	1.33E-01	2.24E-02
6.12E-02	8.28E-01	1.47E-01	2.52E-02
6.92E-02	8.08E-01	1.63E-01	2.85E-02
2.52E-01	4.99E-01	4.00E-01	1.02E-01

Table D.4: pX data for 3.0 grams of sample S350

τ(s)	Ypx	Ymx	Yox
1.48E-02	9.55E-01	3.88E-02	5.99E-03
3.38E-02	8.96E-01	8.93E-02	1.46E-02
6.71E-02	8.39E-01	1.37E-01	2.45E-02
9.84E-02	7.82E-01	1.83E-01	3.51E-02
1.20E-01	7.54E-01	2.05E-01	4.10E-02

Table D.5: pX data for 3.0 grams of sample S800

τ(s)	Ypx	Ymx	Yox
1.49E-02	9.14E-01	6.68E-02	1.87E-02
1.81E-02	8.56E-01	1.12E-01	3.20E-02
2.31E-02	8.82E-01	9.22E-02	2.61E-02
4.96E-02	7.80E-01	1.71E-01	4.91E-02
1.01E-01	6.57E-01	2.63E-01	8.01E-02

Table D.6: pX data for 8.0 grams of sample S800

τ(s)	Ypx	Ymx	Yox
4.22E-02	7.72E-01	1.77E-01	5.09E-02
4.66E-02	7.52E-01	1.92E-01	5.58E-02
5.29E-02	7.20E-01	2.17E-01	6.34E-02
6.47E-02	6.92E-01	2.38E-01	7.05E-02
8.10E-02	6.30E-01	2.84E-01	8.55E-02
1.64E-01	4.66E-01	4.04E-01	1.30E-01

Table D.7: pX data for 1.0 grams of sample S2300

τ(s)	Ypx	Ymx	Yox
1.30E-02	9.29E-01	5.42E-02	1.63E-02
1.62E-02	9.16E-01	6.42E-02	1.94E-02
3.74E-02	8.40E-01	1.22E-01	3.80E-02
2.52E-02	8.86E-01	8.75E-02	2.69E-02
5.05E-02	8.04E-01	1.49E-01	4.71E-02

Table D.8: pX data for 3.0 grams of sample S2300

τ(s)	Ypx	Ymx	Yox
4.11E-02	7.93E-01	1.58E-01	4.89E-02
4.96E-02	7.68E-01	1.77E-01	5.53E-02
7.31E-02	6.95E-01	2.31E-01	7.37E-02
9.98E-02	6.39E-01	2.72E-01	8.93E-02
1.46E-01	5.54E-01	3.34E-01	1.12E-01

Table D.9: pX data for 36.0 grams of sample A150

τ(s)	Ypx	Ymx	Yox
4.81E-02	9.97E-01	2.95E-03	4.41E-04
7.20E-02	9.96E-01	3.88E-03	4.89E-04
1.08E-01	9.95E-01	4.92E-03	5.45E-04
1.71E-01	9.92E-01	7.15E-03	6.59E-04
3.11E-01	9.87E-01	1.20E-02	9.10E-04

Table D.10: pX data for 36.0 grams of sample A350

τ(s)	Ypx	Ymx	Yox
4.60E-02	9.82E-01	1.63E-02	2.08E-03
6.19E-02	9.78E-01	1.93E-02	2.47E-03
8.88E-02	9.69E-01	2.79E-02	3.46E-03
1.34E-01	9.54E-01	4.08E-02	5.03E-03
2.01E-01	9.34E-01	5.85E-02	7.14E-03

Table D.11: pX data for 36.0 grams of sample A800

τ(s)	Ypx	Ymx	Yox
9.44E-02	9.65E-01	2.94E-02	5.91E-03
1.23E-01	9.57E-01	3.59E-02	7.10E-03
1.80E-01	9.39E-01	5.12E-02	1.01E-02
2.72E-01	9.12E-01	7.32E-02	1.46E-02
4.11E-01	8.77E-01	1.02E-01	2.07E-02

Table D.12: pX data for 36.0 grams of sample A2300

τ(s)	Ypx	Ymx	Yox
1.30E-01	8.72E-01	1.04E-01	2.39E-02
1.80E-01	8.53E-01	1.20E-01	2.76E-02
2.57E-01	7.99E-01	1.63E-01	3.83E-02
3.91E-01	7.27E-01	2.19E-01	5.32E-02
5.78E-01	6.36E-01	2.81E-01	8.35E-02

Table D.13: pX data for 6.0 grams of sample A2300

τ(s)	Ypx	Ymx	Yox
2.24E-02	9.78E-01	1.74E-02	4.01E-03
3.03E-02	9.75E-01	1.99E-02	4.67E-03
4.49E-02	9.65E-01	2.79E-02	1.73E-02
6.56E-02	9.50E-01	3.98E-02	9.15E-03
9.93E-02	9.28E-01	5.75E-02	1.32E-02

Table D.14: pX data for 28.5 grams of sample Q350

τ(s)	Ypx	Ymx	Yox
3.01E-03	9.88E-01	1.16E-02	8.36E-04
4.09E-03	9.86E-01	1.26E-02	9.19E-04
6.14E-03	9.83E-01	1.63E-02	1.12E-03
9.27E-03	9.77E-01	2.15E-02	1.37E-03
1.34E-02	9.68E-01	2.98E-02	1.85E-03
2.11E-02	9.57E-01	4.09E-02	2.54E-03
3.07E-02	9.37E-01	5.89E-02	3.81E-03
5.63E-02	8.97E-01	9.57E-02	7.05E-03

Table D.15: pX data for 30.3 grams of sample Q800

τ(s)	Ypx	Ymx	Yox
8.52E-03	9.29E-01	6.06E-02	1.07E-02
1.13E-02	9.14E-01	7.32E-02	1.30E-02
1.72E-02	8.82E-01	9.98E-02	1.85E-02
2.58E-02	8.36E-01	1.37E-01	2.64E-02
3.88E-02	7.78E-01	1.86E-01	3.62E-02
5.88E-02	7.00E-01	2.48E-01	5.18E-02

Table D.16: pX data for 30.3 grams of sample Q2300

τ(s)	Ypx	Ymx	Yox
2.53E-02	8.64E-01	1.18E-01	1.79E-02
3.22E-02	8.33E-01	1.44E-01	2.23E-02
4.51E-02	7.90E-01	1.81E-01	2.95E-02
7.31E-02	6.98E-01	2.56E-01	4.60E-02
1.09E-01	6.08E-01	3.26E-01	6.61E-02

Table D.17: TIPB data for all catalysts

T_f (nm)	Sand τ_m (s/m)	X (%)	Alumina τ_m(s) (s/m)	X (%)	Quartz τ_m(s) (s/m)	X (%)
150	17069	14	106854	5		
	34577	26	338586	13		
	116249	58				
350	16712	34	135452	14	8454	23
	48716	58	400662	33	27136	31
	53056	66				
800	31591	14	109868	17	14511	6.5
	63583	25	331757	38	33533	14
	126098	35				
2300	16995	15	9200	5	9772	41.4
	56092	39	29073	12	31262	77.5
	92723	54	55305	49		

Table D.18: pX data during CVD of TEOS on sample S350

CVD #	Tau(s) ×100	Ypx ×100	Ymx ×100	Yox ×100	CVD #	Tau(s) ×100	Ypx ×100	Ymx ×100	Yox ×100
	2.7	89.3	9.2	1.5		6.5	92.0	6.7	1.3
	5.5	82.4	15.0	2.6		10.9	86.9	11.0	2.1
0	7.8	78.6	18.1	3.3	8	14.2	83.2	14.0	2.8
	8.2	78.4	18.3	3.3		20.0	77.8	18.4	3.8
	10.9	71.9	23.5	4.6					
	2.7	91.8	7.1	1.1		3.7	95.6	3.7	0.7
	5.5	86.1	12.0	1.9		7.2	91.9	6.8	1.3
1	8.0	81.1	16.1	2.8	9	11.1	87.7	10.3	2.0
	10.7	76.5	19.8	3.7		15.3	83.8	13.5	2.7
	14.3	71.1	24.2	4.7		22.5	77.0	19.0	4.0
	2.7	92.5	6.5	1.0		3.8	95.7	3.6	0.7
	5.3	87.2	10.9	1.8		8.4	90.1	8.2	1.6
2	7.9	83.4	14.2	2.5	10	11.5	87.7	10.3	2.0
	10.8	79.3	17.6	3.1		17.9	82.4	14.6	3.0
	14.2	74.7	21.3	4.1		23.2	78.5	17.6	3.9
	2.7	93.6	5.6	0.9		3.8	96.1	3.3	0.6
	5.3	88.7	9.7	1.6		9.4	91.3	7.3	1.4
3	7.8	84.8	13.0	2.2	11	16.1	85.8	11.8	2.4
	10.8	80.6	16.4	2.9		22.0	80.0	16.5	3.5
	13.9	76.0	20.2	3.8					
	2.7	94.3	4.9	0.8		3.9	95.8	3.5	0.7
	5.3	89.1	9.3	1.6		10.1	90.8	7.7	1.5
4	7.7	86.4	11.6	2.0	12	16.5	86.3	11.4	2.3
	11.0	82.3	15.1	2.7		22.0	82.8	14.2	3.0
	14.4	77.5	18.9	3.6					
	2.7	94.9	4.4	0.7		4.2	96.4	3.0	0.6
	5.4	90.2	8.4	1.4		11.2	91.1	7.4	1.5
5	7.7	87.8	10.4	1.8	13	16.9	85.9	11.6	2.4
	10.8	83.9	13.6	2.5		22.1	83.5	13.6	2.9
	14.5	79.7	17.1	3.2					
	3.7	93.1	5.9	1.0		4.5	96.6	2.8	0.6
	7.5	87.7	10.4	1.9		12.2	91.3	7.2	1.5
	8.7	86.4	11.5	2.1	14	17.7	87.0	10.8	2.2
6	12.8	81.7	15.4	2.9		23.2	84.4	12.8	2.8
	15.9	78.3	18.1	3.6					
	3.7	94.8	4.4	0.8		4.5	96.6	2.8	0.6
	6.2	91.7	7.1	1.3		13.1	91.4	7.1	1.5
	8.4	89.0	9.3	1.7	15	17.7	88.9	9.2	1.9
7	10.1	86.7	11.2	2.1		23.2	86.3	11.3	2.4
	14.2	81.6	15.4	3.0					
	20.2	74.9	20.8	4.3					

Table D.19: TIPB data for 5 grams of sample S350

CVD (#)	τ_m (s/m)	X (%)	CVD (#)	τ_m (s/m)	X (%)
0	741783	24.9	4	741783	7.01
	1111989	33.5		1111989	10.4
	2219875	56.7		2219875	20.0
1	741783	22.9	5	741783	3.96
	1111989	31.5		1111989	5.69
	2219875	54.8		2219875	11.1
2	741783	16.0	6	741783	3.30
	1111989	22.2		1111989	4.60
	2219875	41.0		2219875	9.18
3	741783	12.7			
	1111989	17.4			
	2219875	29.9			